UNIVERSITY OF CALIFORNIA
Los Angeles

Airborne Remote Sensing of Radical Precursors in Biomass Burning Smoke Plumes: Emissions, Chemistry, and Radiative Transfer

A dissertation submitted in partial satisfaction of the
requirements for the degree Doctor of Philosophy
in Atmospheric and Oceanic Sciences

by

Nathaniel White Brockway

2021

ABSTRACT OF THE DISSERTATION

Airborne Remote Sensing of Radical Precursors in Biomass Burning Smoke Plumes: Emissions, Chemistry, and Radiative Transfer

by

Nathaniel White Brockway
Doctor of Philosophy in Atmospheric and Oceanic Sciences
University of California, Los Angeles, 2021
Professor Jochen Peter Stutz, Chair

Biomass burning (BB) has worsened in the Western US over the past several decades, a trend that is expected to continue. BB emits particles and precursors of secondary organic aerosols (SOA) and ozone. Ozone and particles are known to have adverse effects on human health, and BB will have a larger impact on the air quality of the Western US. HONO and HCHO are two of the major sources of radicals in BB plumes that drive the chemistry that forms SOA and ozone.

HONO photlyzes quickly, thus providing an early source of OH radicals in smoke. This photolysis complicates the measurement of HONO emissions, as in-situ observations are made after some photolysis has occurred. Remote sensing (RS) provides one solution to this issue, as it can measure fresher smoke and continuously observe smoke as it travels downwind. Unfortunately, little work has been done to understand the radiative transfer (RT) of sunlight through smoke. In this thesis, a radiative transfer model (RTM) was initialized with observations of smoke from an airborne field campaign to understand the ability of RS to observe trace gases in smoke when data is available to constrain the model and how a lack of data impacts that ability.

Results from the RTM suggest a model uncertainty from observations of BB plumes of 16.5%, and greater than 50% if more averaged assumptions are used. The impact of HONO photolysis can also impact RS retrievals by 15% over the first 2 hours after emission. This motivates better modelling of BB plumes for future satellite observations, which are becoming more prevalent. A parameter called the color index may help to inform these assumptions. Early results of HONO to NO_2 emission ratios from satellites agree very well with the observations in this work, and RS observations suggest a high variability of HONO emissions, even by a single fire. Modelling studies of BB plumes must take care to accurately represent HONO emissions. The findings of this thesis motivate further improvements on RT modelling of BB plumes and photolysis rates to better account for RS observations and chemical modelling.

The dissertation of Nathaniel White Brockway is approved.

Paul Wennberg
Rong Fu
Pablo Saide Peralta
Jochen Peter Stutz, Committee Chair

University of California, Los Angeles
2021

To all of my sources of support: my wife, family, and friends

TABLE OF CONTENTS

LIST OF FIGURES

LIST OF TABLES

ACKNOWLEDGMENTS

I would like to thank my advisor, Professor Jochen Stutz, for continuously supporting my research and involving me in interesting projects. I would like to thank the rest of my committee: Professor Pablo Saide, Professor Rong Fu, and Professor Paul Wennberg for their constructive feedback, support, and time.

I would like to thank the wonderful educators in the department for constantly challenging me, especially Professor Suzanne Paulson, Professor Jasper Kok, and Professor Jacob Bortnik. A special thanks to Professor Robert Fovell for introducing me to atmospheric science. I would also like to acknowledge Dr. Robert Spurr for creating the radiative transfer model that made my research possible.

I would like to acknowledge the past and current members of my research group who have always helped me and pushed me: Dr. Ross Cheung, Dr. Catalina Tsai, Dr. Fedele Colosimo, James Festa, Dr. Katja Grossman, Dr. Steve Hurlock, Sarah Johnson, Zoe Pierrat, and especially Katie Tuite. Lastly, I would like to acknowledge the FIREX-AQ science team and the DC-8 flight crew for the tremendous work they did over the Summer of 2019.

VITA

2010-2014	B.S. Atmospheric, Oceanic, and Environmental Sciences, University of California, Los Angeles
2014-2016	M.S. Atmospheric, Oceanic, and Environmental Sciences, University of California, Los Angeles
2014	Academic Assistant, AOS Department, UCLA
2015-2017	Teaching Assistant, AOS Department, UCLA
2015-2021	Graduate Student Researcher, AOS Department, UCLA
2021	Teaching Associate, AOS Department, UCLA

PUBLICATIONS AND PRESENTATIONS

Tuite, K., **Brockway, N.**, Colosimo, S.F., Grossmann, K., Tsai, C., Flynn, J., Alvarez, S., Erickson, M., Yarwood, G., Nopmongcol, U., Stutz, J. (2018). Iodine catalyzed ozone destruction at the Texas coast and Gulf of Mexico. *Geophysical Research Letters*, 45, 7800– 7807. https://doi.org/10.1029/2018GL078267

Brockway, N., Van Roozendael, M., Theys, N., Stutz, J., Kurosu, T., Salawitch, R., Wales, P. (2018). Radiative Transfer Corrections for OMI BrO [Conference Presentation]. 42nd COSPAR Scientific Assembly, Pasadena, Ca, United States.

Brockway, N., Tuite, K., Stutz, J. (2019). Airborne Remote Sensing of HCHO and HONO in Biomass Burning Plumes [Conference Presentation]. AGU Fall Meeting, San Francisco, Ca, United States.

CHAPTER 1

Introduction

1.1 Motivation

Wildfires continue to increase in size and frequency in the Western United States and will have a larger impact on air quality (Westerling, 2016; McClure and Jaffe, 2018). BB emits primary aerosols and the precursors to secondary pollutants, chiefly secondary organic aerosols (SOA) and ozone (Crutzen et al., 1979; Jaffe and Wigder, 2012; Akherati et al., 2020). The secondary pollutants are formed through photochemistry that occurs in BB smoke plumes and can be transported hundreds of kilometers downwind. Both particles and, to a lesser extent, ozone have been known to correlate with human mortality rates due to cardiovascular and respiratory illnesses (Samet et al., 2000; Karanasiou et al., 2021). The actual causes of this relationship are not yet fully understood, but are in part due to oxidative stress in the body stemming from the oxidative potential of these pollutants. The oxidative potential of BB aerosols generally increases as smoke travels downwind due to photochemistry (Wong et al., 2019), thus resulting in more dangerous particles.

There are still many gaps in our understanding of BB smoke emissions and chemistry. As such, the continued study and monitoring of natural BB smoke plumes is essential. Recently, this has mainly been performed through airborne campaigns where smoke is sampled in-situ (*e.g.* WE-CAN and FIREX-AQ experiments). This results in a detailed description of smoke composition. However, our understanding of plume chemistry is confined to a limited range of altitudes and smoke ages, as only a finite number of plume transects can be made. Similarly, such campaigns are costly and only a number of plumes can be probed. Another issue is that very young smoke cannot be sampled as it is highly convective and unsafe to fly through. Therefore, the earliest in-situ measurements often occur in smoke that was emitted at least 15-30 minutes prior.

Passive remote sensing (RS) provides an alternative approach as it can be performed from smaller aircraft and satellites and allows for the safe observation of younger smoke. Measurements in the UV-Vis spectral region can be particularly useful for measuring trace gases important to plume chemistry (*i.e.* formaldehyde, nitrogen dioxide, and nitrous acid). Nitrogen dioxide (NO_2) is a precursor for ozone production, and formaldehyde (HCHO) and nitrous acid (HONO) are two important precursors for hydroxyl and hydroperoxyl radicals (HOx) and drive photochemistry in young smoke plumes (Peng et al., 2020). HCHO and NO_2 are routinely measured from spaceborne instruments to study urban air pollution (Zhu et al., 2017; Goldberg et al., 2021). RS observations have also been used recently to study plume chemistry, showing the potential of these methods to monitor BB plumes (Theys et al., 2020; Jin et al., 2021; Griffin et al., 2021).

Although these observations can be beneficial to quantify and study emissions and chemistry of BB plumes, the science is young and the interpretation of RS observations is challenging. The lack of literature and the complex radiative environment created by a large concentration of highly absorbing and scattering particles necessitates an in-depth analysis on the capabilities of RS observations of BB smoke.

Developments in this field are needed quickly, as climate change and other human impacts continue to affect wildfires in the Western US. Climate change leads to rising temperatures in much of the US and is expected to impact precipitation and snowmelt in the Western US which will greatly impact the frequency and size of wildfires (Ashfaq et al., 2013). This earlier snowmelt, coupled with hotter and drier summertime conditions, leads to a lengthening of the fire season that is predicted to continue over the coming decades (Flannigan et al., 2013).

Coupled with these impacts are the effects of fire suppression that has dominated fire treatment in the US for the past several decades (Parks et al., 2015). These fire suppression efforts have led to an increase in fire fuel in many forests in the Western US. Marlon et al. (2012) has observed a "fire deficit" between the number of fires expected and observed since the late 1800s due to the combined effects of fire suppression and climate forcing from warming temperatures that would naturally cause more wildfires. Williams et al. (2019) has seen a positive correlation between climate forcing and burn area in the Western US since the early 1970's, showing that drier conditions have an exponential relationship with burn area. These impacts may be somewhat counteracted by decreasing fuel growth associated with harsher conditions and the possibility that previously burned areas will not pose as much of a risk of wildfire (McKenzie et al., 2009; Hurteau et al., 2019). Regardless, with hotter and drier conditions, a longer fire season, and more fuel, wildfires are expected to continue to worsen for the next several decades.

Wildfires are beginning to dominate the air quality of much of the Western US during summertime, and this will be exacerbated with improvements in urban air quality and worsening wildfires (Kaulfus et al., 2017). It is therefore critical to study smoke chemistry and create more effective tools for observing smoke on a large scale. In this thesis, I will present remote sensing observations of trace gas amounts in smoke plumes. I will discuss what information can be gleaned from these observations and what tools are needed to interpret them. I will then use these results to determine the ability of satellite instruments to make similar observations. These satellite measurements, coupled with chemical modelling, could provide near real-time forecasts for the downwind air quality caused by wildfires in the future.

1.2 Biomass Burning Smoke Quantification

Smoke is constantly diluted as it disperses and travels downwind, thus impacting aerosol and trace gas concentrations. Therefore, trace gases are often quantified by normalizing against a non-reactive tracer. The normalized excess mixing ratio (NEMR, also known as an enhancement ratio) is defined as:

$$NEMR_{X/Y} = \frac{\Delta X}{\Delta Y} = \frac{[X_{smoke}] - [X_{bkgr}]}{[Y_{smoke}] - [Y_{bkgr}]} \tag{1.1}$$

where the background concentration is subtracted to isolate the amount attributed to BB. In many applications, CO is used as the non-reactive tracer (Y), as it is emitted in large quantities and is relatively non-reactive on the timescale of smoke plumes.

NEMRs are particularly useful for studying plume chemistry, as division by CO accounts for plume dispersion. As a result, any changes in the NEMR as smoke travels downwind are due to chemistry. The NEMR can also be used to quantify emissions. The emission ratio (ER) is the NEMR before significant chemistry has occurred. Although this can be somewhat arbitrary, in practice, the ER is generally the NEMR from observations of the youngest BB smoke.

Similar to an ER, an emission factor (EF) is also used to quantify emissions of trace gases from BB. The EF is defined as the mass of trace gas emitted per kilogram of dry fuel burned

$$EF_X = \frac{\Delta X}{\Delta(CO + CO_2)} \times \frac{MW_X}{MW_C} \times CF \tag{1.2}$$

which is easily calculated in laboratory studies but is more difficult to measure for natural fires where the fuel cannot be weighed. In these cases, the mass of dry fuel burned is often approximated using the sum of CO and CO_2 along with a carbon fraction (CF) of the fuel (~ 0.45). The molecular weights (MW) are used to convert from concentration to mass. This same calculation will also be used for downwind observations, in which case it is deemed an enhancement factor (EnF).

The ER and EF can be converted to one another if the modified combustion efficiency (MCE) is known. The MCE:

$$MCE = \frac{\Delta CO_2}{\Delta(CO + CO_2)} \tag{1.3}$$

explains how efficiently a fire is burning and is a useful parameter to understand burn conditions of a fire. A high MCE indicates an efficient, flaming fire at high temperatures that corresponds with emission of shorter chain volatile organic compounds (VOCs), NOx, and black carbon (BC). A low MCE ($<$0.9) indicates a smoldering fire that is associated with emission of longer chain VOCs with lower volatility (Sekimoto et al., 2018).

1.3 HONO and HCHO as Radical Sources

BB can produce large amounts of secondary pollutants that negatively impact human health. Radical chemistry drives the production of secondary pollutants, chiefly ozone and SOA, in smoke plumes. Therefore, understanding the sources of HOx radicals from BB improves our understanding of overall plume chemistry.

HONO is perhaps the most important HOx precursor emitted from BB, as it is one of few sources of radicals in smoke plumes during the first hour after emission (Peng et al., 2020). HONO rapidly photolyzes in clear-sky conditions, with a photolytic lifetime of 10-15 minutes, to produce OH radicals:

$$HONO + h\nu \rightarrow OH + NO \; (300\,nm < \lambda < 405\,nm). \tag{1.4}$$

Further downwind, HCHO plays a larger role in HOx production through similar photochemistry that produces HO_2 radicals:

$$HCHO + h\nu + 2O_2 \rightarrow 2HO_2 + CO \; (\lambda < 330\,nm). \tag{1.5}$$

However, HCHO photolysis requires higher energy sunlight and therefore occurs more slowly, with significantly longer lifetimes. Photolysis rates are often reduced inside BB smoke plumes due to the extinction of light by the high concentration of particles, and photolytic lifetimes of HONO in smoke plumes can be over an hour. Light intensity also changes vertically in a plume. How this impacts photolysis rates has not been well studied.

Peng et al. (2020) found that HOx production in smoke plumes was dominated by HONO and HCHO photolysis for the first several hours after emission. In particular, HONO photolysis accounted for the vast majority of HOx production in smoke less than one hour old. Although HCHO and HONO may not dominate HOx production to the extent observed by Peng et al. (2020) in all smoke plumes, this finding highlights the impact that HONO and HCHO have on overall plume chemistry.

Measuring HONO emissions from natural fires is difficult due to its fast photolysis. Although smoke obscures sunlight and reduces photolysis rates inside BB plumes, photolytic lifetimes of HONO are still generally less than 1 hour and are often on the order of 30 minutes (Peng et al., 2020). Therefore, some photolysis has occurred by them time the first in-situ measurements are taken. As a result, it is likely that many in-situ measurements of HONO emissions in natural smoke underestimate the true HONO emissions.

Burling et al. (2010) found HONO to be a product of flaming emission. Therefore, one would expect a clear relationship between HONO emissions and MCE. However, HONO emissions are also dependant upon the nitrogen content of the fuel. When normalized against the nitrogen content, HONO emissions appear to have a clearer relationship with MCE (Burling et al., 2010), although this is difficult to characterize for natural fires. For this reason, some studies (*e.g.* Yokelson et al. 2009) quantify HONO emissions as $ER_{HONO/NOx}$.

Due to the complex relationship between HONO emissions, MCE, and nitrogen content, as well as the fast photolysis of HONO, there is currently much uncertainty in our understanding of HONO emissions. For observations of temperate forest (*i.e.* much of the Western US), the HONO emissions from Akagi et al. (2011) and Andreae (2019) differ by 40%. This difference is relatively small compared to many of the other trace gases measured (Andreae, 2019), but the importance of HONO to the plume chemistry makes it important to investigate the difference.

HONO has also been proposed as an important radical source downwind through the heterogeneous conversion of NO_2. There is some experimental evidence of this reaction on several different relevant particle types (Jacob, 2000; Nienow and Roberts, 2006; Stemmler et al., 2006, 2007). Both Trentmann et al. (2005) and Alvarado and Prinn (2009) relied on secondary HONO production to model the observed downwind ozone production for an African Savanna fire. However, Alvarado et al. (2015) found no evidence of secondary HONO chemistry for a chaparral fire in California. More research is thus needed to clarify the role of HONO in BB plumes.

1.4 Secondary Pollutant Production and Aerosol Optical Properties

Tropospheric ozone is formed via the photolysis of NO_2 and the subsequent reaction of an oxygen atom with an oxygen molecule:

$$NO_2 + h\nu \rightarrow NO + O(^3P) \tag{1.6}$$

$$O_2 + O(^3P) \xrightarrow{M} O_3. \tag{1.7}$$

However, NO also reacts to destroy ozone, which often occurs shortly after emission in a BB plume. The oxidation of VOCs converts NO to NO_2, thus leading to net ozone formation. As BB emits both NOx and VOCs, smoke plumes have the potential to form large amounts of ozone (Jaffe and Wigder, 2012). This process can be limited by the availability of radicals to oxidize VOCs. This indicates the importance of HONO and HCHO to plume chemistry, as they drive the processes that lead to ozone formation.

The photochemistry that leads to the production of ozone in BB plumes is also dependent on sunlight to produce radicals (via HONO and HCHO photolysis), recycle radicals, and photolyze NO_2. The large concentrations and optical properties of BB aerosols leads to decreased photolysis rates further inside a plume. Alvarado et al. (2015) found NO_2 photolysis rates to be depleted in the middle of a plume and even less at the bottom of a plume. Baylon et al. (2018) found that the actinic flux of light was even more affected at lower wavelengths. Similarly, Mok et al. (2016) found that BB aerosols in plumes could decrease ozone production by 18%.

As such, the availability of light in smoke plumes is important for the overall chemistry of the plume. Photochemistry likely occurs more quickly in the upper portions of thick plumes where there is sunlight. Similarly, the edges of plumes are also areas of increased photochemistry due to the lower aerosol concentrations and increased sunlight relative to the center of the plume (Peng et al., 2020).

The chemistry that leads to the production of ozone in BB plumes is also responsible for the production of SOA. Particles are directly emitted from BB and, like ozone, can be initially depleted through particle evaporation (May et al., 2015), although the oxidation of VOCs in smoke plumes leads to lower volatility organic compounds and particle condensation (Yokelson et al., 2009; Akagi et al., 2012; Majdi et al., 2019). This generally result in increases in organic aerosol mass and particle size with plume age.

Fires burning with a lower MCE result in the emission of lower volatility organics. As such, the mass of organic aerosols is negatively correlated with MCE (Collier et al., 2016; Jen et al., 2019). These emissions also provide some information on the optical properties of the aerosols. For instance, fires with a higher MCE result in higher emissions of BC due to more complete combustion. One way to define aerosol absorption is with an absorption Ångström exponent (AAE). The AAE is a parameter that describes the wavelength dependence of aerosol absorption:

$$b_{abs}(\lambda) = b_0(\lambda) \cdot \lambda^{-AAE} \tag{1.8}$$

where b_{abs} is the aerosol absorption coefficient at wavelength λ and b_0 is the aerosol absorption coefficient at 1 μm. A similar equation can also be used for the imaginary refractive index of the aerosol (κ). BC therefore has a low AAE, as it absorbs strongly, and roughly equally, at all wavelengths, thus resulting in a black color. Pokhrel et al. (2016) observed higher AAE associated with lower MCE. These organic aerosols emitted at lower MCE with high AAEs are loosely defined as brown carbon (BrC). These aerosols have a strong wavelength dependence of absorption with increasing absorption at shorter wavelengths.

However, the composition and optical properties of BB aerosols vary between different fires (Moosmüller et al., 2011), and even within the same plume. The formation of SOA and oxidation of organic aerosols leads to decreasing absorptivity with photochemical aging (Forrister et al., 2015), although absorptivity can increase over short time scales in young smoke (Hems et al., 2021). Similarly, changes in particle size with aging also impacts aerosol optical properties. The concentration and variability of BB aerosols poses a challenge to RS observations of BB plumes that will be investigated in this thesis.

1.5 Differential Optical Absorption Spectroscopy and UV-Vis Remote Sensing

Remote sensing is a useful tool to study HONO emissions and chemistry, as it allows for observations of smoke directly emitted from burning areas before significant photolysis occurs. Flying over a plume also allows for the continuous observation of trace gases in smoke. This is more difficult to achieve in-situ as the altitude of smoke changes as it travels downwind. Satellites could also become a particularly useful tool to measure HONO emissions and study the downwind evolution of HONO in smoke plumes, as they could measure many more fires than possible in an airborne campaign.

The differential optical absorption spectroscopy (DOAS) technique is used in this thesis to quantify trace gases in BB smoke plumes. The same principles apply to satellite observations with a few minor differences. The DOAS technique utilizes the unique narrow-band absorption features of different trace gases to quantify their amount along a light path (Platt and Stutz, 2008). The theory is based on the Lambert-Beer Law:

$$I(\lambda) = I_0(\lambda) \cdot e^{-\sum \tau_i(\lambda)} \tag{1.9}$$

where I is the incoming light upon an observer, I_0 is the source light, and $\sum \tau_i(\lambda)$ is the sum of optical depths due to Rayleigh scattering, Mie scattering and absorption, and trace gas absorption. For trace gas absorption, the optical depth is equal to the product of the absorption cross-section of the trace gas (σ), the concentration of the trace gas, and the path length of the light:

$$\tau(\lambda) = \sigma(\lambda) \cdot C \cdot \ell. \tag{1.10}$$

For DOAS applications, I_0 is a solar reference recorded by the same instrument. This accounts for many extinction features in measurement spectra and isolates the narrow-band differential absorption features of trace gases. Separate trace gases can then be identified based on their unique, wavelength-dependent absorption.

A slant column density (SCD) is the sum of all molecules along the light path leading from the sun to the observer:

$$SCD = \int_0^L C(s)\, ds \tag{1.11}$$

and therefore accounts for the product of the concentration and path length in Equation 1.10. The differential slant column density (DSCD) accounts for the fact that the DOAS method utilizes a measured solar reference spectrum containing some trace gas absorption:

$$DSCD = SCD - SCD_0 \tag{1.12}$$

where SCD_0 is the SCD of the solar reference spectrum. This is the main difference between satellite and airborne/ground-based remote sensing, as satellites directly retrieve a SCD.

For each measured intensity spectrum, $I(\lambda)$, a non-linear fit is performed to minimize the sum of square differences between the logarithm of the observed spectrum and the function:

$$F(\lambda) = \ln I_0(\lambda) + \sum \sigma_i(\lambda) \cdot DSCD_i(\lambda) + p(\lambda) \tag{1.13}$$

where I_0 is a measured solar reference and p is low-order polynomial to account for Rayleigh scattering and Mie scattering/absorption to retrieve the DSCD of each i^{th} trace gas included in the fit.

Although SCDs and DSCDs can be helpful in quantifying trace gas amounts, they are dependent upon the light path that led to the observer (Equation 1.11). The light path is affected by several parameters, such as measurement geometry, surface albedo, aerosol extinction, and wavelength. It is therefore beneficial to quantify trace gases as a vertical column density (VCD)

$$VCD = \int_0^{TOA} C(z)\, dz. \tag{1.14}$$

which is the sum of all molecules in a vertical column from the surface to the top of the atmosphere (TOA), and is therefore only dependent on the vertical distribution of the trace gas.

The SCD and VCD are related through the air mass factor (AMF):

$$SCD(\lambda) = VCD \cdot AMF(\lambda) \tag{1.15}$$

which accounts for the enhancement of the light path length compared to the vertical.

In most applications, the AMF is calculated using a radiative transfer model (RTM) to account for how light reaches the observer (Section 2.3).

RS observations in the UV-Vis have become an invaluable tool to study the atmosphere (Wagner et al., 2008), and first examples of application of this technique to BB plumes have been reported (Theys et al., 2020; Jin et al., 2021; Griffin et al., 2021). The most common viewing geometry for trace gas monitoring from air and space is in the nadir (Figure 1.1). Other measurement geometries will also be used in this thesis, but the nadir is the primary focus.

Instruments viewing BB plumes in the nadir measure sunlight scattered by atmospheric particles, air molecules, and the ground. The light path can be summarized as follows (Figure 1.1): Sunlight passes through the atmosphere, where it undergoes extinction by gases and particles. This light then enters the highly scattering/absorbing BB plume. Inside the plume, light undergoes multiple scattering on different particles, as well as absorption by trace gases and particles. The light leaving the plume then travels again through the atmosphere to be detected by a suitable spectrometer.

In this application, the zenith reference largely accounts for trace gas absorption above the aircraft, although this is imperfect due to the path length differences stemming from the different viewing geometries. From Figure 1.1, we can also see that the light path length through a plume is only a fraction of the total path length from the sun to the observer. However, trace gas concentrations in a young smoke plume can be two orders of magnitude larger than background air, thus dominating the DSCD signal.

The quantitative impact on this DSCD signal depends on light path lengths, both inside and outside of the smoke plume. Solar and measurement geometry largely control background light path lengths and also impact light penetration in a plume. If the solar

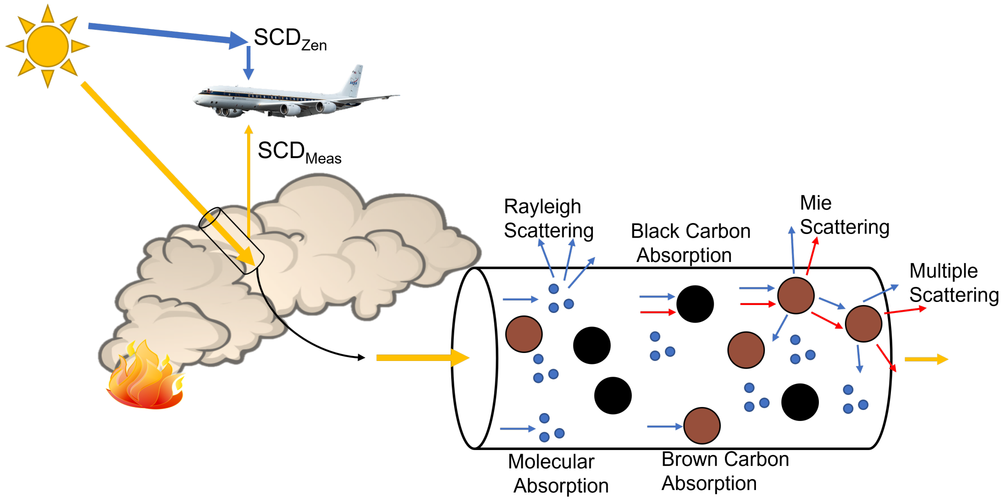

Figure 1.1: Sunlight travels through the atmosphere, into and through the plume, and up toward the instrument. Trace gas absorption inside the plume is the primary focus, but several other radiative transfer effects, listed in the figure, occur inside smoke plumes making this determination difficult.

zenith angle (SZA) is less than 70°, *i.e.* high sun, then light paths through a plume are much more dependent upon the amount and optical properties of the particles. Properly accounting for these effects is necessary to accurately quantify the amount of trace gases in the smoke. Accomplishing this requires accurately modeling the radiative transfer (RT) through a smoke plume.

1.6 Radiative Transfer

In most DOAS applications, RTMs are required to calculate AMFs, and thus VCDs (Hendrick et al., 2006; Wagner et al., 2007; Frieß et al., 2019). The RTM is used to determine the light path length through the atmosphere. This, coupled with information on the vertical distribution of a trace gas, helps determine the AMF. The AMF calculation is dependent upon the vertical profile shape of a trace gas, as light paths change with altitude through the atmosphere. Therefore, the location of the trace gas affects the SCD and the

AMF, meaning different trace gases have different AMFs for the same observation due to their different vertical profiles. As a result, it is more helpful to consider a box air mass factor (BAMF) in this thesis.

Similar to an AMF, a BAMF describes the light path length enhancement through discrete levels of the atmosphere. The BAMF is simply a function of the radiative transfer through the atmosphere, and is therefore unaffected by trace gas profile shapes. The SCD and BAMF are related through:

$$SCD = \sum_{i=0}^{n} BAMF_i \cdot C_i(h) \cdot \Delta h_i \tag{1.16}$$

where $C_i(h)$ is the trace gas concentration profile and Δh_i is the height of the i^{th} altitude level of the atmosphere from the surface (0) to the top of the atmosphere (n). This is simply a numerical approximation of Equation 1.11, where the product of the BAMF and Δh account for the light path length through each level of the atmosphere.

The BAMF is particularly useful, as it describes the instrument sensitivity to each layer of the atmosphere. A larger BAMF signifies a longer light path length through a certain layer of the atmosphere. Therefore, the trace gases in that layer will have a larger impact on the observed DSCD, resulting in larger instrument sensitivity to that layer. The BAMF is affected by all radiative transfer processes in the atmosphere such as viewing geometry, solar geometry, location of scatterers/absorbers, etc. BAMFs can even be 0 for the levels of the atmosphere below a thick plume. The BAMF can be coupled with observed DSCDs and information on the vertical profile of the trace gas to determine the VCD. This information on the trace gas profile can come from a climatology, chemical modelling, observations, or optimal estimation retrieval.

The quantitative interpretation of DSCDs and SCDs emerging from aircraft and satellite DOAS observations is one of the main challenges in UV-Vis remote sensing. Typically, RTMs are used to simulate AMFs, BAMFs, and/or SCDs and DSCDs based on environmental conditions, i.e. sun and viewing geometry, temperature and pressure profiles, aerosol extinction profiles, etc., as well as the vertical trace gas concentration profiles (Baidar et al., 2013; Meier et al., 2017; Zhang et al., 2020; Lorente et al., 2017). However, the RT, and therefore UV-Vis RS in general, in BB plumes presents unique challenges that have, thus far, not been discussed in detail in literature.

BAMFs decrease with decreasing altitude through a smoke plume as particles obscure sunlight. This results in decreased sensitivity of RS to trace gases lower in the plume. Compared to a clean-air observation with the same DSCD, an observation of smoke would require higher concentrations of a trace gas inside the plume to create the same DSCD, due to this decreased measurement sensitivity. A further complication stems from the fact that the areas of decreased instrument sensitivity are co-located with the highest trace gas concentrations. Therefore, accurately accounting for the RT through a plume is essential to accurately quantifying trace gases in the plume.

Several properties of BB smoke complicate the RT through the plume, chiefly that smoke particles are highly scattering/absorptive. It is therefore crucial to properly account for the amount and specific optical properties of the smoke aerosols to understand how light travels through a plume. However, many properties of BB aerosols are highly variable.

As smoke ages, particles generally grow due to accumulation and condensation which affects the optical properties of the aerosols (Alvarado and Prinn, 2009; Hennigan et al., 2011). Oxidative processes on the surface of aerosols can also affect the optical properties of aged particles. Fires emit, and plumes contain, varying amounts of BC and BrC aerosols, which are highly absorptive in the UV-Vis wavelength range and greatly impact how light travels through a plume (Pokhrel et al., 2016). Further complicating this issue is that BrC is a loose definition, and there is a wide range of wavelength dependent absorption of these aerosols (Saleh et al., 2018). Few studies of BrC consider wavelengths below 400 nm, again adding uncertainty to UV-Vis remote sensing (Chakrabarty et al., 2010; Saleh et al., 2013; Pokhrel et al., 2016). Besides the large variability of the aerosol optical properties, atmospheric dynamics are also a source of BB plume variability. As smoke travels downwind, it can change altitude and disperse vertically and/or horizontally

All of these effects introduce uncertainty and make RS observations dependent on the unique RT environment of the particular observation. These impacts must be understood in order to interpret RS data of BB plumes. One major focus of this thesis is determining how effectively these processes can be accounted for in RS observations. Once it is clear that smoke plumes can be effectively modelled, a RTM will be used to quantify trace gases in BB smoke plumes based on RS observations. This thesis will also consider the ability to model RS observations of a BB plume if not all information on aerosol properties and plume geometry is known. These findings can help improve future satellite observations of BB plumes.

1.7 FIREX-AQ

Data presented in this thesis comes from the FIREX-AQ field campaign performed in the the summer of 2019. The goal of this project was to measure trace gases and aerosols in biomass burning smoke via aircraft to better understand BB emissions and chemistry. Many research groups operated roughly 30 instruments on board the NASA DC-8 aircraft, including in-situ and remote sensing instruments. There were other ground-based and aircraft instruments associated with this project, but this thesis will only use data from the DC-8.

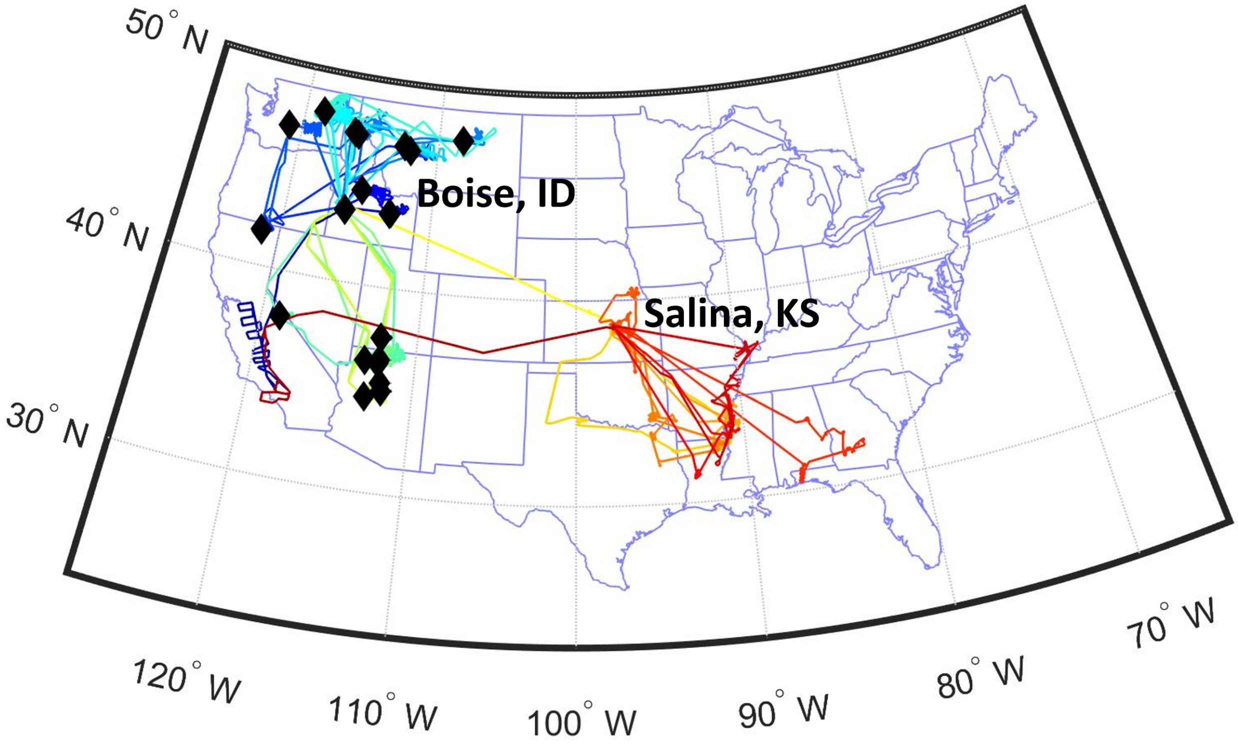

Figure 1.2: Flight tracks and location of Western wildfires from the FIREX-AQ campaign.

FIREX-AQ was split in two halves. The first half focused on wildfires in the Western US and operations were based out of Boise, Idaho. The second half was based out of Salina, Kansas and focused on small agricultural fires in the Southeastern US and one prescribed burn in the Florida panhandle. In all, 23 separate flights were flown, including 3 transit flights. Figure 1.2 shows the flight paths with each flight plotted in a different color. The black diamonds indicate the location of each wildfire observed during the first half of the campaign.

The flight path for all Western wildfires and the Blackwater River State Park prescribed

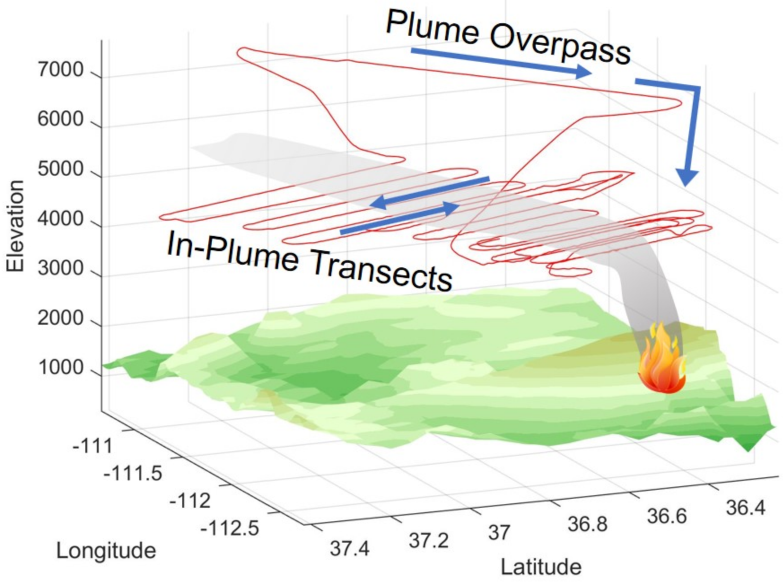

Figure 1.3: A typical flight plan for observing a Western wildfire.

burn were generally the same. Figure 1.3 shows the usual aircraft flight path for a wildfire measurement strategy during the campaign. The aircraft first overflew the plume, flying from downwind past the fire. During this plume overpass, the LIDAR remotely observed the location and altitude of the smoke. The aircraft then descended and flew perpendicular to the direction of the smoke plume. The aircraft first flew upwind of the fire, to measure background aerosol and trace gas concentrations, and then through the smoke, working its way downwind. This pattern was often repeated several times, if possible. The RS data presented here will primarily focus on plume overpasses. In-situ observations during in-plume transects will be used to constrain the RTM and to compare with RS observations.

1.8 Science Questions

- *Will UV-Vis remote sensing of biomass burning plumes offer new information?*

  RS of BB plumes offers an exciting opportunity to study the emission and chemistry of radical precursors that can drive the downwind photochemistry in plumes Theys et al. (2020). However, little work has been done to understand the uncertainties associated with these observations. The first goal of this thesis is to determine the ability of RS to observe trace gases in BB plumes.

- *What are the emissions of HONO in biomass burning plumes?*

  The emission of HONO by biomass burning is of prime importance for downwind chemistry, as emitted HONO provides a source of OH radicals early in smoke plumes. HONO is difficult to measure in-situ, leading to differences in HONO emission calculations (Akagi et al., 2011; Andreae, 2019; Peng et al., 2020). This thesis will quantify HONO emissions to study these differences. Further, RS observations will be used to study downwind HONO chemistry and possible secondary formation.

- *What is the ability of satellites to measure biomass burning plumes?*

  The first goal of this study is to determine how well RS can retrieve trace gases with the aid of several other instruments on board the same aircraft. However, satellite RS must make assumptions to account for the lack of in-situ observations. The third goal of this thesis is to determine how accurately satelltie observations can represent BB plumes without reliable support data.

1.9 Thesis Outline

In Chapter 2, the RS instrument used for this work will be introduced. The other instruments on board the DC-8 during FIREX-AQ will also be discussed. Perhaps most importantly, the RTM used will be introduced, followed by an in-depth description of how the model was initialized to represent BB plumes. Chapter 3 will discuss the analysis techniques used to interpret RS data. This chapter will explain how VCDs were calculated from RS data and how the RS data was used to calculate HONO emissions from BB burning.

Results from the analysis of raw RS observations, *e.g.* HONO emissions, will be shown in Chapter 4. Emission observations will be compared to other sources. This will be followed by a discussion of HONO chemistry in the plumes based on RS observations. Results from RTM calculations are examined in Chapter 5. Future observations of BB plumes from satellites will rely on similar RTM calculations, so much of this chapter is focused on understanding the RTM results and the implications they have for RS observations. The results from the previous two chapters are summarized and investigated in Chapter 6, and future studies will be motivated.

CHAPTER 2

Instrumentation and Tools

2.1 Mini-DOAS

2.1.1 Instrument Details

The data used in this thesis was gathered by the UCLA mini-DOAS (Stutz et al., 2017), a passive airborne remote sensing instrument. The instrument consists of three independent telescope/spectrometer combinations that measure in the UV-Vis, visible, and near-IR wavelength ranges, seen in Figure 2.1. The telescopes had a 0.25°x1° field of view and viewed in the forward direction at any angle between the nadir and zenith, depending on the geometry of the aircraft and smoke plume. Although the visible spectrometer can measure glyoxal and NO_2 in smoke plumes and the near-IR spectrometer can measure CO_2 which may provide information on the chemistry of smoke plumes, this thesis will focus on data from the UV-Vis spectrometer.

The DC-8 is the third aircraft that the mini-DOAS has flown on and had the longest distance between the instrument and the telescopes. As such, new, roughly 20 ft long fiber optic cable bundles were installed. The UV-Vis fiber bundle consisted of 6 200 μm quartz fibers arranged linearly to maximize light throughput while maintaining spectral resolution.

Light from the fibers was fed to an Ocean Optics QE65000 spectrometer that measured

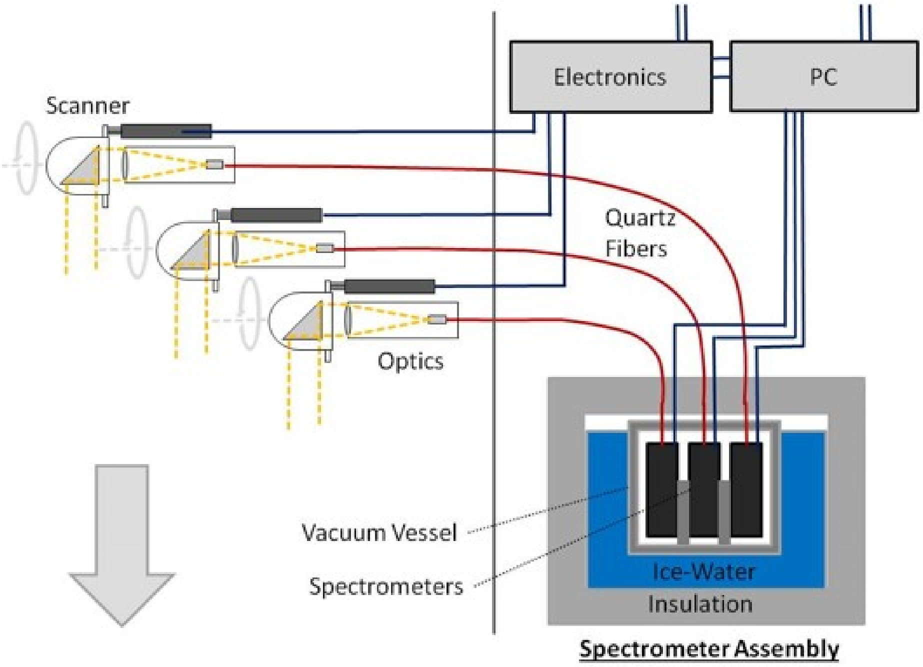

Figure 2.1: Schematic of the mini-DOAS instrument. Three independent telescopes (left) viewed in the forward direction and fed light to spectrometers measuring in the UV-Vis, visible, and Near-IR wavelength ranges.

scattered sunlight from roughly 300-380 nm with a resolution of 0.5 nm FWHM. The spectrometer box, and fiber cable connectors, were vacuum sealed, as seen in Figure 2.1. The spectrometer box was temperature regulated in an ice water bath that was filled with roughly 50% ice and 50% ice water an hour before takeoff of each flight. Temperatures generally rose less than 2 °C over the duration of a flight, so temperature and pressure had little influence on the spectral structure of the spectrometer.

Lastly, the UV-Vis telescope included a HOYA 340 UV bandpass filter to reduce spectrometer straylight. This filter added specific spectral characteristics to the measured spectra that will be discussed later.

2.1.2 Measurement Technique

Observations of smoke plumes were generally recorded with 5 second time resolution using an auto-exposure algorithm which maintained the detector signal at 50% of its maximum. Over dense smoke plumes, the exposure time was capped at 5 seconds.

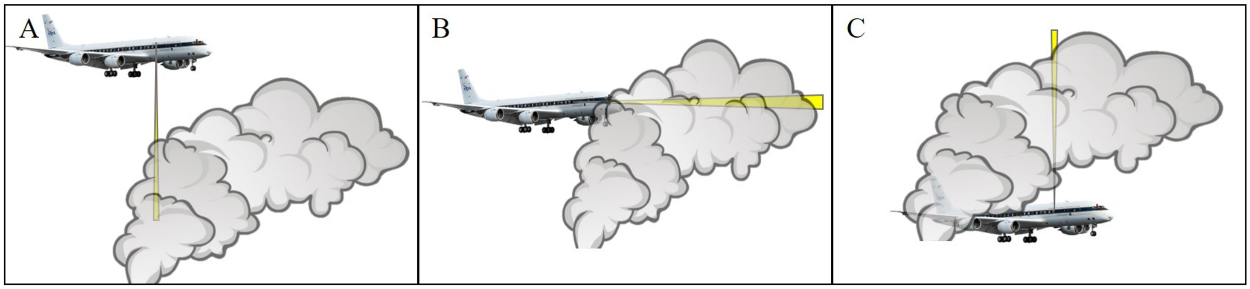

Figure 2.2: Common mini-DOAS observation geometries to observe BB smoke plumes.

The typical viewing geometry for a Western wildfire depended on where the aircraft was located in relation to the plume as well as the plume geometry. For the plume overpasses, shown in Figure 1.3, the mini-DOAS observed the smoke in the nadir (Figure 2.2A). During these times, the LIDAR instrument concurrently measured aerosol extinction profiles in the nadir, albeit with different temporal resolution.

After the plume overpasses, the aircraft performed in-plume transects (Figure 1.3). During these transects, the mini-DOAS often measured smoke in a limb or near-limb geometry (Figure 2.2B) in order to maximize light path lengths through the smoke. However, in several instances, the smoke was very optically thick and light throughput became an issue. To guarantee that the mini-DOAS received enough light, the instrument observed smoke with a zenith-viewing geometry (Figure 2.2C). This was rather common for transects through young smoke before significant dispersion occurred, starting after Flight 7.

The viewing strategy for agricultural fires in the Southeastern US similarly depended on plume geometry. Some fires measured during this half of the campaign were large enough to observe in the same pattern as the Western wildfires (Figures 1.3 & 2.2). One particular example was a prescribed burn in the Blackwater River State Park on August 30th, 2019 in the Florida panhandle. This fire was extensively studied by the DC-8.

Figure 2.3: DC-8 forward view camera snapshot of a small agricultural fire from August 21, 2019. The DC-8 would fly once crosswind through the plume (shown here), and once in the direction of the wind (from left to right on this figure).

However, many fires, *e.g.* Figure 2.3, were too small to measure with this strategy. Many of these fires were the purposeful burning of specific agricultural plots. As such, they produced little smoke that dispersed quickly, as can be seen in Figure 2.3. To observe these small plumes, the DC-8 flew at a low altitude ($\sim$ 1000 ft), flying in the direction of the wind through the smoke and turning to fly through the smoke perpendicular to the wind (shown in Figure 2.3). Ideally, the mini-DOAS would measure these plumes in a near-nadir geometry to quantify emissions. However, this generally allowed for only one observation causing a small margin of error. As a result, these plumes were often measured in the limb/near-limb.

2.1.3 Solar Reference Spectra

The choice of reference spectra during this campaign was very important to reduce the impact of background trace gas absorption and minimize the impacts of changing solar geometry. Reference spectra ideally had a similar solar geometry, similar flight altitude, no influence from biomass burning, and a zenith viewing geometry. These specifications made the spectral analysis and RT interpretations considerably easier. This is particularly important for NO_2 retrievals in order to avoid stratospheric influence on the retrieved absorption. To further reduce observational uncertainties, reference spectra were co-added, ideally for over a minute of observation.

To meet these stated requirements, zenith spectra were often gathered for several minutes preceding a plume overpass (Figure 1.3). Similarly, the first transect upwind of the fire was often used to record zenith spectra for the in-plume transects. In some cases, there was not enough time to record zenith spectra before a plume overpass so clear-sky nadir observations were used as references which makes properly accounting for background trace gas profiles more important. Similarly, some in-plume transects ladders lasted several hours to observe dispersed smoke well downwind of a fire. To account for this, some in-plume transect flight segments were split in half, utilizing a zenith reference upwind of the fire and a zenith reference downwind of a plume.

2.1.4 Spectral Pre-processing

All observed scattered-sunlight spectra were corrected for offset and dark current and had a 20-order low-pass binomial applied to them, after co-adding in the case of the solar references. Lastly, all reference spectra recorded while the aircraft had a roll (horizontal tilt) of greater than 5° are disregarded from co-adding. Similarly, any measured spectra with a roll greater than 5° are removed from the analysis.

2.1.5 DOAS Theory and Fit

The DOAS theory was used to retrieve DSCDs from measured spectra (briefly described in Section 1.5). The primary focus of this study is the measurement and quantification of HCHO, HONO, and NO_2 in biomass burning plumes. O_4 measurements can also be helpful to determine the distance between the aircraft and the smoke plume. The LIDAR instrument on board the aircraft makes O_4 measurements unnecessary, but these 4 species can all be retrieved in the same fit range. The fit routine and trace gas absorption cross-sections used to retrieve these species are listed in Table 2.1. All trace gas reference spectra were pre-convoluted based on Hg lamp observations and high altitude zenith measurements in order to apply a wavelength dependent instrument function. Due to the smoothing of the observed spectra, all mini-DOAS uncertainties listed are 3 times the fit retrieval uncertainty. One hope of this study was the retrieval of SO_2 and HCHO further into the UV, but this was not feasible for reasons described below.

This fit routine results in very good sensitivity to HCHO, HONO, and NO_2 in BB smoke plumes. For observations of young, thick smoke, the median fit uncertainty for these three species was roughly 15% for HCHO, 12% for HONO, and 17% for NO_2. This high sensitivity can be seen in Figure 2.4, which shows an example retrieval of HCHO, HONO, and NO_2. This figure shows the fit result for each absorption-cross section along with the residual added to the fit. It is clear that the spectral structures of these three gases are easily observed in this observation of a young smoke plume. For this case, the relative fit uncertainty for HCHO, HONO, and NO_2 was 9%, 7%, and 12%. Also shown

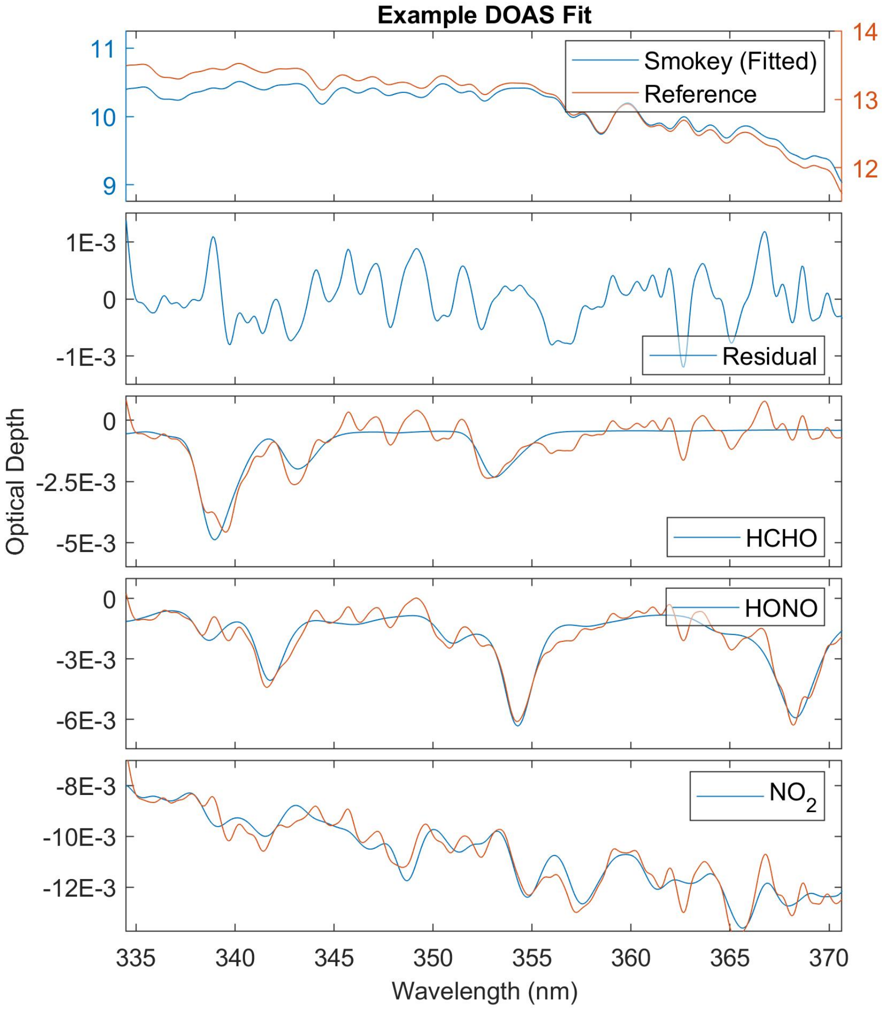

Figure 2.4: An example DOAS fit retrieval of a smokey spectrum. This spectral analysis shows good sensitivity to HCHO, HONO, and NO_2 with a low fit residual. Also shown (top) is the log of the measurement spectrum and reference spectrum. This shows that the observed spectrum received considerably less light at low wavelengths compared to the reference due to absorption by the smoke plume.

FIT PARAMETER	DETAILS
Fit Range	334.6-370.8 nm
Polynomial	4th order
Ring Spectra	3
Zenith Spectrum	
O_4	293 K Thalman and Volkamer (2013)
NO_2	280 K Voigt et al. (2002)
O_3	283 K & 243 K Gorshelev et al. (2014)
H_2O	Rothman et al. (2010)
HONO	Stutz et al. (2000)
HCHO	Calvert et al. (2000)

Table 2.1: DOAS fit parameters to retrieve DSCDs of HONO, HCHO, and NO_2. This routine is also used to retrive O_4 DSCDs, but those are not used in this work.

in this figure is the solar reference spectrum, which was recorded just 15 minutes before the measurement spectrum, thus reducing the fit uncertainty of the trace gases.

2.1.6 Color Index

The strong wavelength dependent extinction observed in smoke plumes (Figure 2.4, top) motivated the use of a parameter called the color index (CI). In this nadir observation of BB smoke, measured intensities were considerably lower at smaller wavelengths compared to the reference spectrum, which was also observed in the nadir in this case. The CI is defined as the ratio of incident light at two different wavelengths:

$$CI = \frac{I(360nm)/I_0(360nm)}{I(340nm)/I_0(340nm)}. \tag{2.1}$$

Intensities at 340 and 360 nm were used to cover the area of highest HONO and HCHO absorption. The ratio is also normalized against a clean-air spectrum (I_0) to account for the spectral structure of the HOYA 340 UV bandpass filter.

The CI is sensitive to wavelength-dependent extinction along the light path leading to the telescope. The CI was independently calculated for each plume overpass which covers a sampling time of roughly 15 minutes. Therefore, for SZA less than 80°, Rayleigh scattering has little impact on the color index. Similarly, the impact of surface albedo wavelength dependence appeared to be small in this wavelength range. The dependency of BB smoke on the CI will be investigate and used to constrain RTM calculations.

2.1.7 Sulfur Dioxide Retrievals

As stated earlier, one hope of the study was to use mini-DOAS observations to measure SO_2 in BB smoke plumes. SO_2 is less reactive than the other species in question and could therefore act as a tracer species. Unfortunately, the main absorption features of SO_2 are below 315 nm. After considerable effort, it was deemed that the mini-DOAS could not utilize these wavelengths to measure SO_2 in smoke for reasons affecting the intensity of light received by the instrument. Up to five measurement spectra were co-added in an attempt to increase signal-to-noise, but without success.

The main issue is the wavelength-dependent absorption of BrC in smoke plumes, which has a large impact at 315 nm. As a result, there was not enough light for the mini-DOAS to consistently and accurately observe SO_2 in the measured spectra (Figure 2.5). However, there were clear-sky and optically thin smoke observations that provide hope that a more sensitive instrument may be capable of measuring SO_2 in select BB plumes.

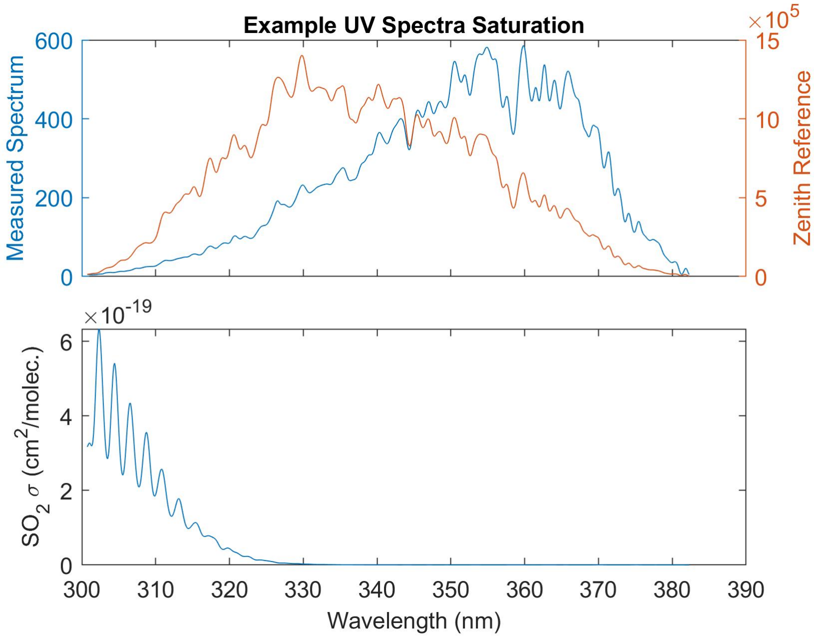

Figure 2.5: Example mini-DOAS zenith measurement spectrum (blue) inside an optically thick plume and the zenith reference (orange) recorded in clear-sky. Also shown is the absorption cross section for SO_2 (bottom). SO_2 must be observed at wavelengths below 315 nm, where this specific spectrum recorded hardly any incoming light. The wavelength dependent extinction seen in the top plot make this wavelength range difficult to use.

2.2 FIREX-AQ Instruments and Analyses

There were several instruments on board the NASA DC-8 aircraft, seen in the external view of the aircraft (Figure 2.6) and the internal view which shows the numerous instrument racks inside the DC-8. Many of these instruments are relevant to the research in this thesis, and the instruments used are listed in Table 2.2. These were used to constrain RTM calculations and interpret mini-DOAS observations. Instrument/analysis descriptions, usage, and available references are outlined below. All data described here, and from other instruments not used in this work, are publicly available at: 10.5067/SUBORBITAL/FIREXAQ2019/DATA001.

INSTRUMENT NAME / ANALYSIS	MEASUREMENT(S)
DIAL High Spectral Resolution LIDAR	Aerosol Extinction Profiles BB Plume Shape
Langley Aerosol Research Group Experiment (LARGE)	Particle Size Distributions In-situ Aerosol Extinction & Scattering
Aerosol Optical Properties (AOP)	In-situ Aerosol Extinction & Scattering
Compact Atmospheric Multispecies Spectrometer (CAMS)	HCHO Mixing Ratios
Airborne Cavity Enhanced Spectrometer (ACES)	HONO Mixing Ratios NO_2 Mixing Ratios
Differential Absorption Carbon monOxide Measurement (DACOM)	CO Mixing Ratios CO_2 Mixing Ratios
Charged-coupled device Actinic Flux Spectroradiometers (CAFS)	Trace Gas Photolysis Rates
Meteorological Measurement System (MMS)	Atmospheric and Location Variables *e.g.* Temperature, Pressure, etc.
Fire Location & Wind Speed	Smoke Age
Meteorology backtracing	Smoke Age
Fuel2Fire	Fuel Type Classification
MODIS/ASTER Airborne Simulator (MASTER)	Fire Radiative Power
Visible and IR Cameras	

Table 2.2: A list of instruments on board the NASA DC-8 and analyses from the FIREX-AQ field campaign.

Figure 2.6: External and internal view of the NASA DC-8 aircraft show the numerous other instruments on board (left image courtesy of NASA).

2.2.1 DIAL/HSRL

Aerosol extinction profiles were taken from the differential absorption LIDAR/high spectral resolution LIDAR (DIAL/HSRL) instrument(Hair et al., 2008) at 532 nm using the measured LIDAR backscatter coefficient and LIDAR ratio, both of which have a vertical resolution of 30 meters. This study utilized the 10 second measurements of these parameters as opposed to the reported 60 second extinction profiles. This may add some uncertainty, but the largest uncertainty is due to the actual parameter variability of the LIDAR ratio, and 60 seconds is too coarse of a resolution for our observations.

In several overflight measurements of thick plumes, the LIDAR backscatter coefficient was saturated (Figure 2.7 Left). This means that there was no data for the bottom portion of the plume because the extinction was so high that light could not penetrate the plume. This has little impact on RT modelling, because for instances in which the LIDAR instrument saturated at 532 nm, our measurements near 350 nm are also not sensitive to that portion of the plume. This data was filled in to produce input data for the RTM, ac-

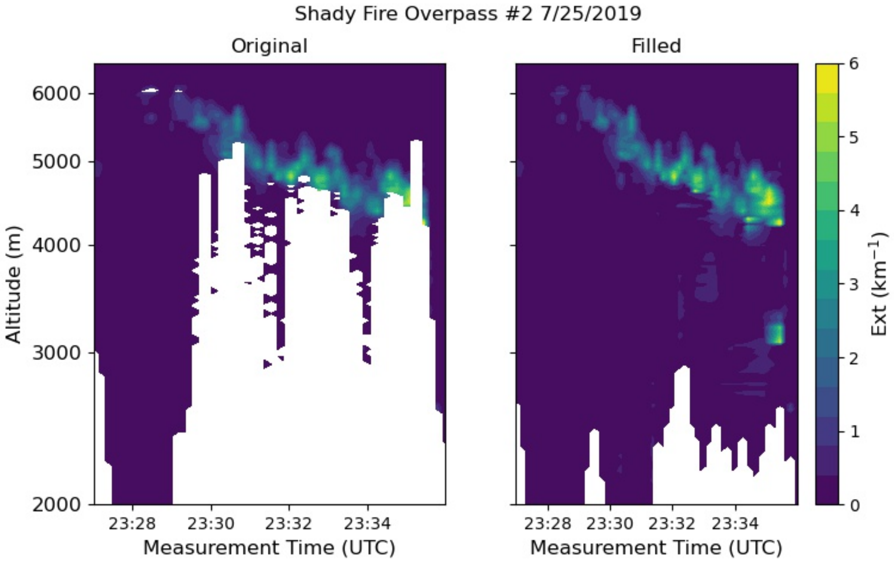

Figure 2.7: An example of the effect of filling in missing LIDAR data for the second overpass of the Shady fire on July 25th. Many observations are missing below the plume due to instrument saturation (left). The right plot shows the LIDAR profile after missing data were filled in.

count for the total aerosol optical depth (AOD), and determine trace gas vertical column density.

To fill in this missing data, extinction profiles from the geographically nearest in-plume transect (within 1 hour of the overflight measurement) were used to fill in extinction data at any missing altitudes. This data was then interpolated horizontally. If there were still missing data points in the profile, the existing profile was fit with a Gaussian shape and missing data was filled with these values. The impact of this method can be seen in Figure 2.7 where the original, saturated LIDAR data is shown on the left and the filled extinction data is shown on the right. This process seems to reasonably fill in lofted data, although the column of rising smoke is still not resolved.

2.2.2 LARGE

Particle size distributions (PSDs) are particularly important for the definition of aerosol optical properties for RT modelling. PSDs were determined from laser aerosol spectrometer (TSI model 3340) 1 hz measurements at ambient temperature and humidity with diameters from 100 nm to roughly 5 microns, measured by the Langley aerosol research group experiment (LARGE). These observations were used to calculate log-normal particle size distribution parameters for smoke aerosols, boundary layer aerosols, and free tropospheric aerosols. The particle sizes covered by this instrument are the most optically relevant for UV-Vis remote sensing observations. Extinction data from the LARGE team was also used along with other sources depending on data availability.

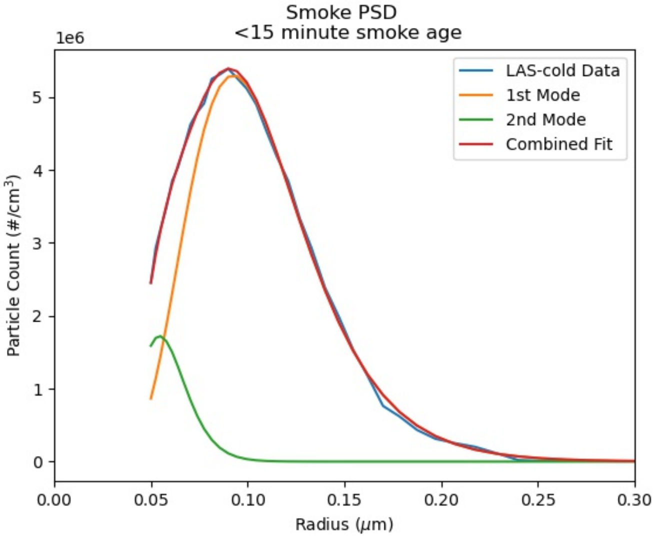

Figure 2.8: An example particle size distribution fit of young smoke. Smoke PSDs were fit with a log-normal bimodal distribution. The first mode (orange) is meant to capture the distribution for radii larger than the peak, so greater than $\sim 0.1\mu$m in this case. The second mode (green) accounts for the difference between the observation and this first mode. The R^2 of this method was regularly above 0.99.

An example PSD is shown for all young (<15 minute smoke age) smoke measurements of the Shady Fire in Idaho on July 25th, 2019 (Figure 2.8, Blue). The PSDs were consistently well explained with a bimodal, log-normal fit with a major mode near 100 nm (Orange), and a second mode near 60 nm (Green) radius. The combination of these modes (Red) is a nearly perfect fit of the PSD in this case.

2.2.3 AOP

1 hz data from the AOP team (Langridge et al., 2011; Lack et al., 2012) was used to create background profiles of ambient aerosol extinction (Section 2.3.3). Extinction and absorption data at 405 nm were also used to calculate smoke single scattering albedo (SSA) and determine the BC content to include in RTM runs.

2.2.4 CAMS

The compact atmospheric multi-species spectrometer (CAMS, Richter et al. 2015) used mid-IR laser spectroscopy to measure HCHO mixing ratios at 1 hz resolution. This data was used to constrain a background HCHO profile for the RTM as well to compare with mini-DOAS observations.

2.2.5 ACES

We used the airborne cavity enhanced spectrometer (ACES, Min et al. 2016) 1 hz data for observations of HONO and NO_2. As with HCHO, ACES was used to create background atmosphere profiles of HONO and NO_2 and to compare with mini-DOAS observations.

2.2.6 DACOM

The differential absorption carbon monoxide measurement (DACOM, Warner et al. 2010) instrument was very important to calculate emissions from in-situ instruments and mini-DOAS data. DACOM measurements of CO and CO_2 were necessary to calculate NEMRs (Equation 1.1) and EFs (Equation 1.2) for various trace gases using in-situ data.

2.2.7 CAFS

The charged-coupled device actinic flux spectroradiometers (CAFS, Shetter and Müller 1999) instrument was valuable for understanding the photochemistry of smoke plumes, as it measured actinic fluxes at a 1 hz resolution. Actinic fluxes were combined with absorption cross-sections to produce photolysis rates for several trace gases, including HONO, NO_2, and HCHO. Although not directly used to interpret mini-DOAS data or constrain RTM calculations, CAFS data was still very helpful for modelling photolysis rates and filtering in-situ observations for photochemically young smoke.

2.2.8 MMS

Data from the meteorological measurement system (MMS, Chan et al. 1998) was important to constrain atmospheric parameters, like temperature and pressure, and were especially important for flight altitude data.

2.2.9 Smoke Age

In order to interpret mini-DOAS data (*e.g.* the rate of chemical changes), it is important to quantify the age of the observed smoke. This is also important in order to compare mini-

DOAS and in-situ data, as the overpass and in-plume data are not gathered concurrently.

One method to determine the smoke age is by simply using the distance from the fire and the mean wind speed at the smoke altitude. This is a simple calculation, is easily implemented, and can be used for both in-plume and overpass observations. As such, all use of smoke age with remote sensing observations will utilize this method of determining smoke age. Similarly, any comparison of remote sensing and in-situ data will utilize this smoke age calculation for in-situ observations as well so as not to introduce bias.

However, there is a more advanced smoke age calculation available for in-plume observations that utilizes the HYSPLIT back trajectory modelling. This method is helpful as it can account for changing wind speeds throughout the plume as well as the plume rise. Perhaps the most important feature of this calculation is that it allows for changing plume age through a transect of the smoke. This is useful to determine if each observation of a transect was subject to the same photochemistry. This smoke age calculation was used to determine emissions from in-situ data and to filter in-situ data to account for changing chemistry.

2.2.10 Fuel Burned

The fuel burned by each fire was useful for interpreting HONO emissions and comparing them to other works. The fuel burned was determined by the Fuel2Fire group using several sources of data (Soja et al., 2021), starting with the fuel characteristic classification system (FCCS, Prichard et al. 2019). FCCS is a tool to catalog the different flora species with a 30 m resolution. This dataset is combined with fire detections from VIIRS observations coupled with diurnal variability determined from GOES observations. This results in a daily estimate of the area burned and carbon emitted by different fuel types.

2.2.11 MASTER

The MODIS/ASTER Airborne Simulator (MASTER) is an instrument that uses thermal radiation bands to spatially resolve the fire radiative power throughout the burning area (Hook et al., 2001). This is helpful to determine the state of the burning for the areas of the fire measured during mini-DOAS overpasses.

2.2.12 Cameras

As with most remote sensing campaigns, camera data from the aircraft was invaluable. Videos (*e.g.* Figure 2.3) were used to study oddities in mini-DOAS data. For instance, the convection from many fires created pyrocumulus clouds above a fire, which often lowered trace gas DSCDs in mini-DOAS data due to lower sensitivity to the plume itself. The nadir camera on the DC-8 was very helpful to locate these pyrocumulus observations. Similarly, the nadir IR camera was used to determine the location of the fires at the time of the overpass in order to determine the smoke age of mini-DOAS observations.

2.3 Radiative Transfer Model: VLIDORT-QS

As discussed in Section 1.6, a RTM is needed to account for the numerous optical properties of a BB plume in order to interpret mini-DOAS data. Considering the large variability of BB smoke plumes and the effect on mini-DOAS observations, the RTM needed to be run for each individual measurement. As such, the RTM used in this study needed to be computationally fast. Monte Carlo RTMs (*e.g.* McArtim, Deutschmann et al. 2011), are very accurate but also very computationally expensive. For this reason, this study utilized VLIDORT, which my research group has found agrees with McArtim to within

1%.

An accurate simulation of the mini-DOAS measurements during the FIREX-AQ campaign required a RTM with fully spherical ray-tracing capability for both single-scattering (SS) and multiple-scattering (MS) radiative processes to explain the measurement sensitivity to different layers of the atmosphere. The VLIDORT-QuasiSpherical (VLIDORT-QS) vector RTM (Spurr, In Progress) is based on the 2015 2.7 version of the VLIDORT code (Spurr, 2006; Spurr and Christi, 2019) and was specifically designed and developed for the interpretation of airborne limb scanning measurements. In order to include the contribution of the sphericity of the atmosphere to the signal, the code implements a multi-shell model, with multiple optically uniform layers, extending from the surface to the top of the atmosphere, allowing RT simulation for different solar geometries, elevation angles, and altitudes.

The versatility of VLIDORT-QS allowed for the model to be used for any realistic measurement geometry used throughout the campaign. Similarly, The state of the atmosphere, the location and amount of aerosols, and the optical properties can be easily updated for each model run, which is particularly beneficial for this application. A python wrapper was used to set the solar and viewing geometry, surface albedo, background atmosphere profiles, aerosol profiles, and aerosol optical properties for each observation externally to avoid recompiling VLIDORT-QS for each model run and save computational time.

In order to properly simulate the signal traveling in a curved atmosphere, the radiative transfer equation (RTE) is separately solved for the SS and MS component for each ray path segment, *i.e.* for each layer defined by the model. For each segment, the SS source term is evaluated by integrating the RTE using a Gauss-Legendre quadrature scheme defined by a finite number of points of abscissa and weights which allow the code to define a set of optical thickness values for that segment. The radiation field is then calculated in a recursive manner, propagating these source terms from the ray path origin, depending on the viewing geometry, to the observer in a fully spherical atmosphere.

For the MS term, the code first implements the standard VLIDORT code for each segment to generate a set of discrete-ordinate solutions for the RTE for each quadrature point in that segment in a plane-parallel scenario. The MS source term is subsequently derived utilizing the quadrature scheme used in the SS case for a fully spherical atmosphere, thus integrating the source function in a full spherical geometry.

2.3.1 Size-Resolved Mie Code

To properly represent the radiative impacts of BB plumes, RTM calculations must include the impacts of background aerosols and BB aerosols. Further, calculations must be able to capture the variability of BB aerosols, *i.e.* changes in size, composition, etc. In order to accomplish this, a size-resolved Mie code was coupled with VLIDORT-QS to account for the optical properties of the aerosols.

The size-resolved Mie code allowed for a trimodal PSD, although in this case only bimodal and monomodal distributions were used. The Mie code utilizes a log-normal PSD

$$P(r) = e^{-(\ln \frac{r}{r_0})^2/2(\ln \sigma)^2}/r \tag{2.2}$$

and takes the mean radius (r_0) and standard deviation (σ) as inputs for each PSD mode. The modes are then weighted based on their particle number concentrations (an example is shown in Figure 2.8). The Mie code was run for measurement wavelengths between 300 and 380 nm, with 10 nm resolution, as well as for 400 nm and 1 μm. Refractive indices for several aerosol types were also used (Section 2.3.3).

For each aerosol PSD with a given refractive index at a certain measurement wavelength, the mie code calculates aerosol scattering and extinction cross-sections and aerosol scattering moments, which can be used to determine the scattering phase function of the aerosols. These results are calculated for a normalized PSD with the amount of aerosols controlled separately in the RTM. This code was specifically created for compatibility with VLIDORT-QS and runs separately. It was therefore used each time aerosol optical properties were updated for individual RTM calculations.

2.3.2 VLIDORT-QS Output

2.3.2.1 Radiances & Slant Column Densities

VLIDORT-QS was run for a model grid of 78 discrete layers from the surface to 43 km altitude, with 100 m resolution for the lowest 5 km and broader spacing approaching the TOA.

One output of VLIDORT-QS is an incident radiance upon the observer. Therefore, the Lambert-Beer law (Equation 1.9) can be used to calculate trace gas SCDs by running the RTM with and without a respective absorber. We can adjust the Lambert-Beer equation:

$$I(\lambda) = I_0(\lambda)^{\sum SCD_i(\lambda)\cdot\sigma_i(\lambda)+\tau_r(\lambda)+\tau_m(\lambda)} \tag{2.3}$$

where τ_r and τ_m are the impacts of Rayleigh and Mie scattering. Equation 2.3 is the basis for the DOAS fit (Section 2.1.5).

This new representation of the Lambert-Beer law shows how VLIDORT-QS can be used to model SCDs, by running the model with (I) and without (I') an absorber:

$$SCD(\lambda) = \frac{-1}{\sigma(\lambda)} \log \frac{I(\lambda)}{I'(\lambda)}. \tag{2.4}$$

This same process can be done for the solar reference observation to calculate SCD$_0$ (Equation 1.12) and determine modelled DSCDs.

2.3.2.2 Jacobians & BAMFs

Along with radiances, VLIDORT-QS calculates trace gas or particle Jacobians, etc. Jacobians quantify the change in radiance due to a change in another parameter in each layer of the atmosphere. For trace gases, the Jacobians are defined as the change in radiance (I) due to the change in the partial vertical column of a trace gas (D):

$$J_i(\lambda) = \frac{\partial I(\lambda)}{\partial D_i} \tag{2.5}$$

where the partial column (D) is the concentration times the height of layer i.

However, this parameter is not particularly useful, as the DOAS technique does not directly rely on either of these parameters. It is much more important to define how the DSCD or SCD changes as a function of the partial column:

$$\frac{\partial DSCD(\lambda)}{\partial D_i} = \frac{\partial SCD(\lambda)}{\partial D_i} \tag{2.6}$$

which are equal since the DSCD is simply offset from the SCD by a parameter (SCD$_0$) that does not depend on the trace gas profile of the measurement.

Using Equation 2.4, where σ and I' are not affected by changes in the partial column of the trace gas:

$$\frac{\partial SCD(\lambda)}{\partial D_i} = \frac{\partial(\frac{-1}{\sigma(\lambda)} \log \frac{I(\lambda)}{I'(\lambda)})}{\partial D_i} \tag{2.7}$$

$$= \frac{-1}{\sigma(\lambda)} \frac{I'(\lambda)}{I(\lambda)} \frac{\partial(\frac{I(\lambda)}{I'(\lambda)})}{\partial D_i} \tag{2.8}$$

$$= \frac{-1}{I(\lambda) \cdot \sigma(\lambda)} \frac{\partial I(\lambda)}{\partial D_i} \tag{2.9}$$

we find that change in the SCD due to change in the partial column of a trace gas is simply the modelled Jacobian normalized by the modelled radiance (I) and the trace gas absorption cross-section (σ).

Equation 2.9 is the formal definition of the BAMF (from Equation 1.16). It should now be obvious that Equation 1.16 is simply a numerical approximation of the integral of ∂SCD with respect to the partial trace gas column. In this way, VLIDORT-QS is used to calculate BAMFs for each mini-DOAS observation.

The resulting BAMF explains the path-length enhancement, and thus measurement sensitivity through each layer of the model. The BAMF does not depend on the specific trace gas but rather on the radiative transfer that defines the light path length through a layer in the atmosphere which affects all trace gas SCDs equally at the same wavelength.

2.3.3 Model Initialization

The model is constrained with data from other instruments on board the aircraft in order to accurately portray the atmosphere and measurement conditions. As smoke plumes are quite variable, many model parameters are updated for each individual observation, resulting in unique BAMFs for each mini-DOAS observation.

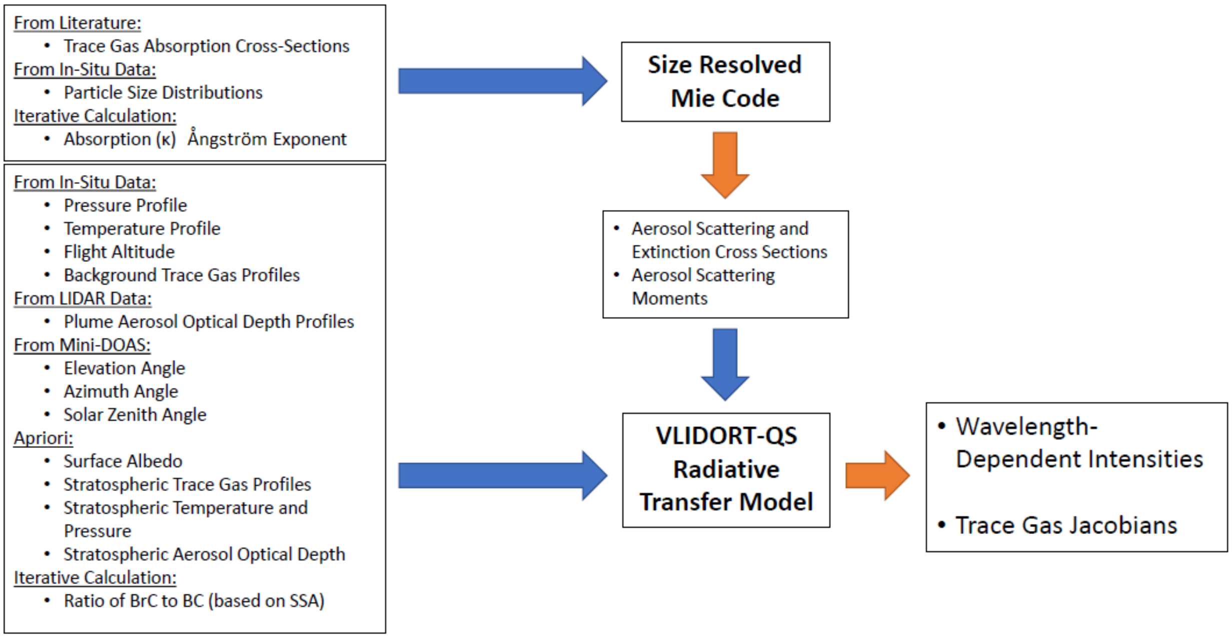

Figure 2.9: VLIDORT-QS requires an accurate representation of the atmosphere. This figure summarizes the data used to initialize VLIDORT-QS and the coupled size-resolved Mie code in order to calculate intensities and Jacobians (BAMFs) for each mini-DOAS observation.

To accurately model mini-DOAS observations, an accurate representation of the atmosphere was needed. Section 2.2 describes the sources of the data used to constrain the model, but there are a few details worth noting. The data used for all VLIDORT-QS model runs is shown in Figure 2.9. An apriori atmosphere was created based on a summertime climatology of the Western US with profiles of pressure, temperature, O_3, NO_2, BrO, HCHO, HONO, and SO_2 as a function of altitude. Each of these parameters was then updated with available in-situ (non-smoke) data from throughout the flight, binned and averaged in 50 m height intervals. These profiles were then interpolated to a 78-layer altitude grid, normalizing against the surface altitude, with a 100 m resolution for the lowest 5 km. The surface albedo was determined from climatology (Kleipool et al., 2008) based on latitude, longitude, and month (generally on the order of 0.07).

Perhaps most important is how the RTM handled aerosols. This was done by defining the aerosol profile and the optical properties of the aerosols. VLIDORT-QS aggregated four distinct aerosol types for each model run. The optical properties of these aerosols were needed to calculate the aerosol radiative properties at the model wavelength as opposed to the measurement wavelength (*e.g.* 532 nm for LIDAR data).

The background aerosol profile was calculated using 532 nm aerosol extinction data from AOP (Section 2.2.3) in the same way the trace gases were used to create a background profile. This data was used as there was less missing data compared to other observations and it is easier to guarantee there is no influence from BB on the in-situ data. Profiles from SAGEII climatology (NASA/LARC/SD/ASDC, 2012) were used for stratospheric aerosols. The BB aerosol profile was calculated by subtracting the background aerosol profile from the 532 nm extinction data from the LIDAR instrument (described in Section 2.2.1). Again, missing/saturated LIDAR data was filled in with in-plume LIDAR observations and a Gaussian plume shape.

The optical properties: scattering, extinction, and phase function, were determined for each aerosol type using refractive indices and PSDs (Section 2.2.2) with a size-resolved Mie code (Section 2.3.1). The aerosols were split into four different types based on these optical properties.

For background aerosols, the lower atmosphere generally consisted of larger particles. As such, boundary layer background aerosols were separated from free troposphere and stratosphere background aerosols as being below or above 4 km GPS altitude. Optical properties were calculated for these two aerosol types based on their individual PSDs and a refractive index for clean, continental aerosols (Levoni et al., 1997). The background aerosol extinction and optical properties were held constant for RTM calculations of all plume overpasses from a given day.

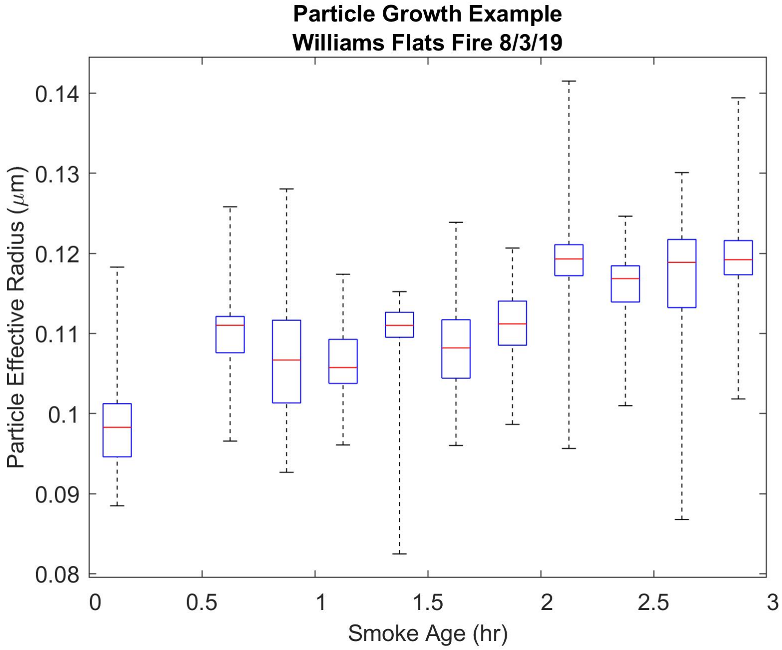

Figure 2.10: Example particle growth for the Williams Flats fire on August 3rd, with the number-weighted particle effective radius shown against the smoke age.

The optical properties of BB aerosols were more variable, and thus required more consideration. First, BB particles generally grew as a function of plume age, as shown for the Williams Flats fire in Figure 2.10, which affects their optical properties. As such, BB particles were binned in 15 minute intervals as a function of smoke age. The Mie code was then run for each of these PSD bins, and the optical properties were updated for each model run depending on the age of the smoke observed.

Next is the issue of refractive indices, as smoke plumes consist of many types of aerosols. BC was included as one type of aerosol in the smoke plumes, utilizing refractive indices of soot (Chang and Charalampopoulos, 1990; Levoni et al., 1997). It was assumed that the majority of the remaining aerosol is organic. As such, a refractive index of BrC (Alexander et al., 2008) was used, with the imaginary refractive index scaled to a value of

0.015 at 405 nm, based on observations of peat fire smoke (Sumlin et al., 2018). However, this model setup resulted in significantly less wavelength-dependent extinction than seen by the mini-DOAS (via the CI, Section 2.1). Wavelength-dependent absorption was thus added to this latter aerosol type by applying a κ absorption Angström exponent (κAE) to the imaginary refractive index below 405 nm. The κAE was determined by iteratively updating the value until the RTM recreated the CI for the entire overflight. The κAE was thus held constant for RTM calculations for an overpass.

Parameter	RTM Representation
BC Refractive Index	Mean of Chang and Charalampopoulos (1990) and Levoni et al. (1997)
BB Aerosol Refractive Index	Alexander et al. (2008) scaled to Sumlin et al. (2018) with κAE below 400 nm
Background Aerosol Refractive Index	Levoni et al. (1997)
Background Pressure Background Temperature Trace Gas Profiles Background Aerosol Profile Background Aerosol Optical Properties	Calculated for each flight and held constant
BC Ratio κAE	Iteratively calculated and held constant for each overpass
Surface Albedo	Updated for each observation using location and Kleipool et al. (2008)
Plume Aerosol Profile	Updated with LIDAR observations
BC and BB Aerosol Optical Properties	PSD updated for each observation based on plume age
Measurement Geometry Solar Geometry	Updated for each observation

Table 2.3: Summary of how each parameter is updated for RTM calculations.

The last consideration was what portion of the BB aerosol was BC. This was determined by iteratively running VLIDORT-QS at 405 nm, updating the proportion of BC until the modelled and measured 405 nm SSA (Section 2.2.3) agreed. The resulting ratio (on average 13%) was then used to split the BB extinction profile from the LIDAR into BC and remaining BB aerosols. This ratio was held constant for an entire plume overpass. It should be noted that a 13% BC content is a relatively high value, though not unrealistic, for biomass burning (Saleh et al., 2014). However, the RTM results are not particularly sensitive to the BC content, where a ± 15% BC content has less than a 2% impact on model results. Further, this method ensures that the model recreates the aerosol optical properties at 405 nm before running the model at lower wavelengths.

To summarize (Table 2.3), the background profiles of pressure, temperature, trace gas concentration, free troposphere/stratosphere aerosol extinction and optical properties, and boundary layer aerosol extinction and optical properties were held constant for all RTM calculations of a plume overpass. The proportion of BC in the smoke plume and the κAE were iteratively derived for each plume overpass and held constant. The surface albedo, plume aerosol profile, measurement geometry, solar geometry, and BC and BB aerosol optical properties were updated for each mini-DOAS observation using a python wrapper to avoid recompiling the model. The model was run at 353.5 nm which is in the middle of our DOAS fit window (Section 2.1) and where there is strong HCHO, HONO, and NO_2 absorption resulting in unique BAMFs for each mini-DOAS observation.

2.3.4 Radiative Transfer and the Color Index

As discussed in Section 2.3.3, the CI was used to constrain the RTM calculations and specifically, the κAE. Every other parameter besides the imaginary refractive index of BB aerosol was well defined in the RTM, either through good apriori assumptions, data from the flight, or literature. When the model was used to recreate the observed CI from mini-DOAS data, it was discovered that the CI was particularly sensitive to the κAE of the BB aerosols.

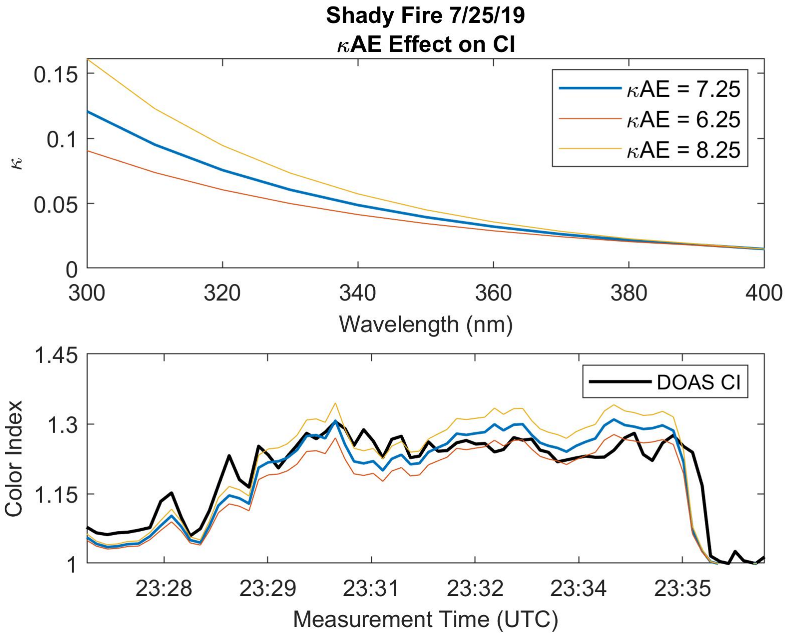

Figure 2.11: This figure shows the imaginary refractive index for three different κAEs (top), with the retrieved κAE for this overpass being 7.25. The bottom shows the observed CI from the mini-DOAS for this overpass with the modelled CI using each of these κAEs, and displaying the sensitivity of the CI to the input κAE.

An example is shown in Figure 2.11 for the second overflight of the Shady Fire on July 25th, 2019. The imaginary refractive index (κ) is shown for three different κAE scenarios (Top). The lower plot shows the impact of these κAEs on the modelled CI and how they compare to the mini-DOAS measured CI. For this overflight, a κAE of 7.25 gave the best agreement. However, a κAE of 7.25 leads to a slight overestimation of the CI early in the plume and slight underestimation later in the plume. This could indicate an increasing κAE as a function of smoke age in this fire, either from changing emissions or chemical changes, such as particle growth, aerosol oxidation, and aerosol coating. However, the associated uncertainties are too high to confirm these explanations. As such, a single κAE was used for each overpass, but this should be an area of future study.

CHAPTER 3

Analysis Methods

3.1 Trace Gas Profiles

Knowing the profile shape of retrieved trace gases is crucial to accurately quantifying their amounts in the smoke plume. The reason for this, as will be discussed in depth below, is the changing sensitivity of the mini-DOAS through a smoke plume. For nadir observations, the mini-DOAS was most sensitive to the top of a BB plume, with sensitivity decreasing with altitude as more light is occluded by smoke the further into a plume. As this area of rapidly changing instrument sensitivity is also where we expect rapidly changing concentrations, it is necessary to accurately account for both factors.

HCHO and aerosols are co-emitted by BB, and both undergo relatively slow chemistry early in smoke plumes. Generally, both HCHO and aerosols are slowly formed in BB plumes. At the same time, HCHO is photolyzed, with lifetimes on the order of hours inside smoke plumes. Consequently, aerosol extinction is a good tracer for HCHO concentrations. Therefore, the 532 nm aerosol extinction data from the LIDAR can be used to represent the profile shape of HCHO in young BB plumes.

One example to confirm this assumption is seen in Figure 3.1. The top plot shows the comparison of HCHO (from CAMS) and 532 nm aerosol extinction (from AOP) for an in-plume transect of 3 hour old smoke. In this case, there is near perfect agreement between

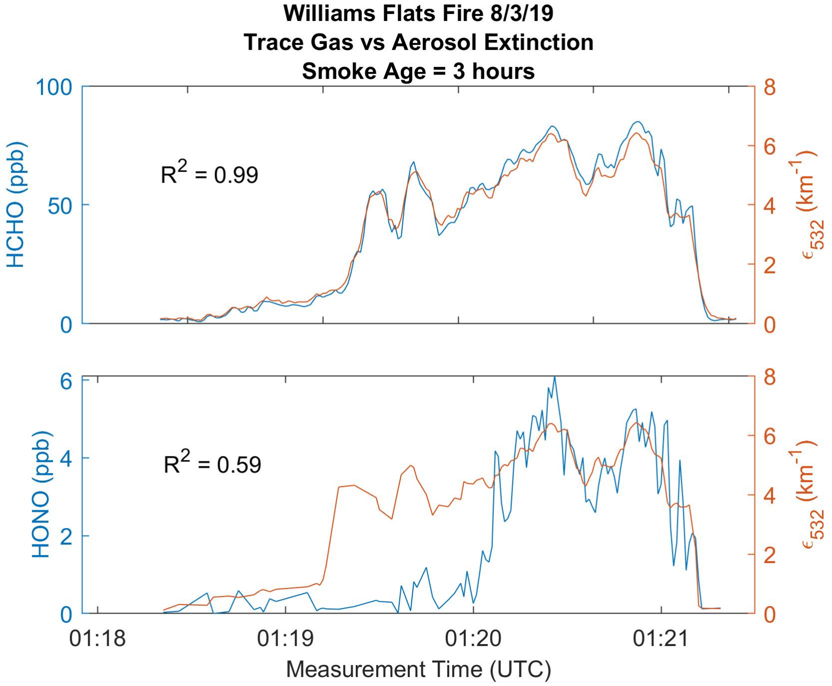

Figure 3.1: This figure shows the relationship between trace gases (blue) and aerosol extinction (orange) for a transect of 3 hour old smoke. The shape of HCHO and aerosol extinction (top) are nearly identical. However, the relationship with HONO (bottom) is much poorer due to photolysis in the first part of the transect.

HCHO and aerosol extinction hours after emission and after some photochemistry has occurred. For over 265 in-plume transects of Western wildfires, like the one showed in this figure, the mean R^2 between HCHO and 532 nm extinction was 0.944 with no dependence on plume age. This signifies that the LIDAR aerosol extinction profile is an accurate representation of the HCHO vertical plume profile for all smoke ages.

The bottom plot shows an example where the aerosol extinction is not a good tracer for a trace gas, in this case HONO. The first half of the plume was the "sunny side" with higher photolysis rates, and the HONO horizontal profile changes with respect to aerosol extinction. Clearly, some other representation of the vertical plume profile is needed for HONO.

3.2 Chemical Model

HONO and NO_2 undergo quicker chemistry than HCHO due to their with particularly fast photolysis. If the photolysis was constant through the plume, then the aerosol extinction profile could still be used to represent the profile shape of HONO and NO_2, as only the profile shape is needed for the interpretation of DOAS data. However, one would expect the photolysis rate of a trace gas to change drastically as a function of altitude through an optically thick BB plume due to less light penetrating deeper into the smoke.

Therefore, a more advanced representation of HONO and NO_2 is needed for the interpretation of mini-DOAS data. For this research, the platform for atmospheric chemistry and vertical transport in one-dimension (PACT-1D) chemical model was used to study the photochemistry of HONO in biomass burning plumes. The model is described in Tuite et al. (2021) where the HONO chemistry mechanisms were confirmed with observations from a 2010 study. It has since been applied to model the chemistry of BB plumes, which will be discussed in an upcoming manuscript and thesis.

The chemical model is not the focus of this study, so it will not be described extensively. Further, only two mini-DOAS plume overpasses have been modelled with PACT-1D thus far. However, these results can still inform future remote sensing studies.

3.3 Photolysis Rates

Perhaps most important for HONO chemistry in a BB plume is the altitude dependence of the photolysis rate. To accurately represent the photolysis rate in PACT-1D, VLIDORT-QS was used to model the vertical distribution of HONO photolysis rates (j_{HONO}).

Unfortunately, actinic fluxes are not an output of VLIDORT 2.7, although this has since been implemented in VLIDORT 2.8 and is currently being studied. As a result, VLIDORT-QS was run for an array of viewing zenith and azimuth angles and integrated to calculate a normalized actinic flux at 341.7 nm, in the middle of a HONO absorption peak. VLIDORT-QS was initialized as discussed in Section 2.3.3, and this pseudo actinic flux was calculated for each LIDAR observation from the first half of the campaign and compared to 10 second average j_{HONO} values (from CAFS, Section 2.2.7). This comparison is done to ensure that the VLIDORT-QS pseudo actinic flux is an accurate parameterization of observed j_{HONO} values.

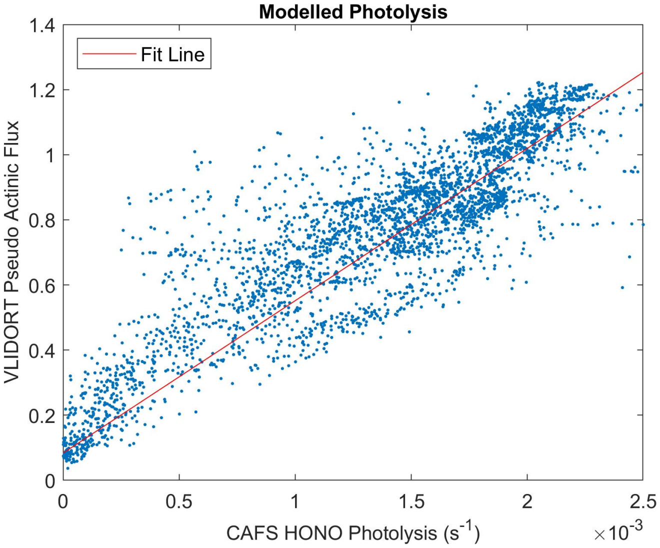

Figure 3.2: Model results comparing the observed HONO photolysis rates to VLIDORT-QS model results show good agreement between the two.

The resulting actinic flux calculations can be seen on the y-axis of Figure 3.2 compared to 10 second average in-situ j_{HONO} values. For these 3649 observations, VLIDORT-QS predicts the HONO photolysis rate with a R^2 of 0.784, a fit slope uncertainty of 0.24%, and a standard deviation between the fit and measurements of 2.87×10^{-4} s^{-1}. For simplicity, this modelling utilized more averaged values than the BAMF calculations. Similarly, in-plume actinic flux calculations are highly dependent upon the overhead AOD, making filling in missing LIDAR data even more important. These sources of uncertainty could be reconsidered to find better model agreement with observed j_{HONO} values. However, this first attempt confirms that VLIDORT-QS can account for changes in photolysis rates and be used to study those changes.

After confirming that VLIDORT-QS can represent j_{HONO} rates, it was used to determine the vertical variability of j_{HONO} rates through a BB plume. The RTM was initialized (Section 2.3.3) for a thick (532 nm AOD = 2.28) and thin (AOD = 0.92) Gaussian plume and run at a 50 m vertical resolution from 100 m altitude to 4.5 km. The resulting pseudo actinic flux profile shape was then used to create a j_{HONO} profile parameterization.

As the j_{HONO} profile is dependent upon the shape and optical thickness of the plume, it was important to create a parameterization that was easily adapted to any situation. Further, PACT-1D relied on in-situ data from in-plume transects that took place just after the fire overpass, so it was important that the parameterization recreated the observed j_{HONO} values from these transects. The resulting photolysis parameterization was based on a bidirectional sigmoid function to account for upwelling and downwelling radiation:

$$J(z) = J_{dwn}(z) + J_{up}(z) \tag{3.1}$$

$$J_{dwn}(z) = \frac{J_t - J_{min}}{1 + e^{(z'-z)/F}} + J_{min} \tag{3.2}$$

$$J_{up}(z) = \frac{J_b}{1 + e^{(z-z")/F}} \tag{3.3}$$

where the variables are explained in Table 3.1. However, these equations have three unknown parameters (z', $z"$, and F) and can therefore not be solved with just one in-situ data point.

To account for this, the equation was linearized between the top of the plume and the

Parameter	Description
$J(z)$	j_{HONO} at altitude z
J_{dwn}(z)	Downwelling component of $J(z)$
J_{up}(z)	Upwelling component of $J(z)$
J_t	$J(z)$ at the top of the plume
J_{min}	Minimum j_{HONO} rate
z'	Offset altitude where $J(z) = (J_t + J_{min})/2$
F	Factor to control slope of the photolysis profile
J_b(z)	$J(z)$ at the surface
z"	Offset altitude for upwelling radiation

Table 3.1: Variable descriptions for Equations 3.1, 3.2, and 3.3.

measurement location to solve for z' and F. It was then assumed that the plume aerosol extinction is symmetric around its peak, which is a approximately the case for a modelled plume, and solve for z" based on the downwelling parameters.

$$z' = \frac{z_t - z}{J_t - J(z)}(J_m - J(z)) + z \tag{3.4}$$

$$\text{where } J_m = (J_t - J_{min})/2 \tag{3.5}$$

$$z" = z_b + z_t - z' \tag{3.6}$$

$$F = \frac{z' - z}{\log(\frac{J_t - J_{min}}{J(z) - J_{min}} - 1)} \tag{3.7}$$

For these equations, z' is the midpoint of the downwelling sigmoid function, z" is the midpoint of the upwelling sigmoid function, and F controls the rate of change of these sigmoid functions.

Throughout the campaign, we found that upwelling radiation consistently accounted for 20% of clear-sky j_{HONO} values. Therefore J_b is 20% of the clear-sky j_{HONO} value and J_t is 80%. Similarly, J_{min} also must be specified, ideally based on observations.

For validation of this approach, the photolysis profile was modelled with VLIDORT-

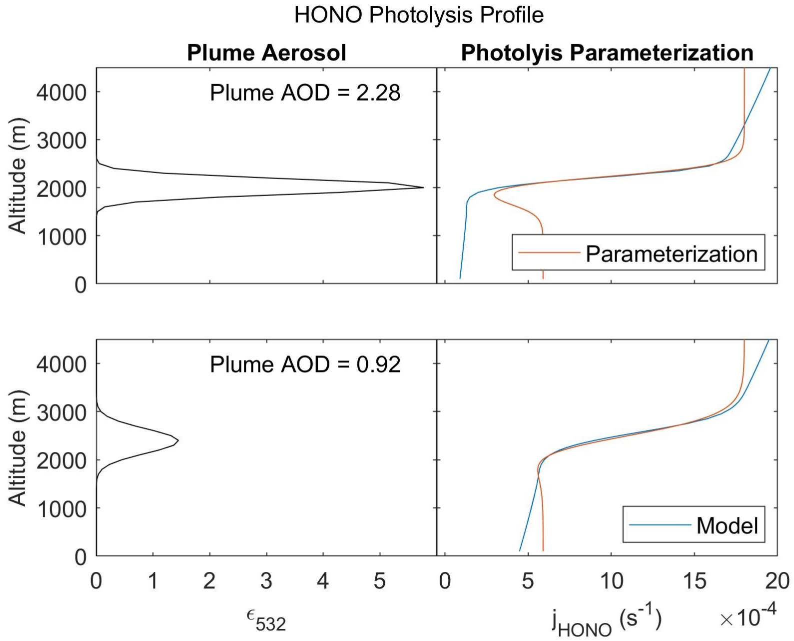

Figure 3.3: Modelled photolysis rates and parameterization results for an optically thick (top) and thin (bottom) plume.

QS for observations of the Shady Fire on July 25th, 2019 and a Gaussian plume shape. For this example, J_t was set to 1.8×10^{-3} s^{-1}, indicating clear-sky HONO photolytic lifetimes of roughly 7.5 minutes, based on overpass j_{HONO} observations. J_{min} was set to 1.4×10^{-4} s^{-1} based on the lowest in-plume observations of this plume. $J(z)$ and z were chosen based on normal in-plume observation altitudes near the center of the plume. The resulting parameterization can be seen for two different scenarios in Figure 3.3.

This parameterization represents the vertical photolysis profile from VLIDORT-QS and accounts for the changing dynamics of the plume, as it represents both thick and thin smoke. For the thick plume case (top), the model and parameterization do not agree at the surface. This is because VLIDORT-QS is a 1D model, and cannot resolve upwelling radiation that did not first have to pass through the smoke plume. Similarly, the model and parameterization do not agree above the plume where j_{HONO} slowly increases from

J_t to $J_t + J_b$. However, capturing the rates inside the smoke is more important, and both cases show good agreement inside the plume, confirming that this is an accurate and easily adaptable parameterization and was therefore implemented in PACT-1D.

3.4 Vertical Column Density Retrieval

While SCDs and DSCDs provide useful information on the amount of trace gases in smoke plumes, they are also dependent on light path lengths both inside and outside of a plume. It is thus preferable to convert them to concentration profiles or plume vertical column density (VCD), i.e. the vertical integral of a trace gas concentration profile inside a plume. Conversion of a SCD/DSCD to a VCD depends on the shape of the vertical trace gas concentration profile. This is especially true for BB plumes, where the trace gas profile exhibits very large change from the top to the center of the plume. Consequently, an accurate description of the plume shape is necessary for the VCD retrieval.

As discussed in Section 3.1, the LIDAR aerosol extinction profile is a good representation of the HCHO profile, as both are co-emitted and undergo relatively slow chemistry. The LIDAR profile thus accounts for plume dispersion and can be used to describe the shape of the HCHO profile in mini-DOAS observations. The LIDAR profile does not work well for photolytic trace gases (*i.e.* HONO and NO_2), where it is expected that the shape of the vertical profile changes due to increased photolysis at the top of the plume (Section 3.2) and chemical model calculated profiles must be used.

Once the plume shape (S) has been determined, mini-DOAS observations can be used to derive a concentration profile, a VCD by integrating this retrieved profile, or a maximum trace gas mixing ratio in the plume. All three representations will be shown, although they are all variations of the same retrieval.

The concentration profile can be described as the sum of the background concentration profile (MR_0) and the plume concentration profile:

$$MR(z) = MR_0(z) + \overline{MR} \cdot S(z) \tag{3.8}$$

where the plume shape is normalized to a mean of 1 over the plume altitudes. This approximation is used to solve for the mean plume mixing ratio ($\overline{MR}$), the plume concentration profile (the product of $\overline{MR}$ and S), and the VCD (the integral of the concentration profile).

The approach to calculate these parameters from DSCDs is based on a combination of Equations 1.12 and 1.16:

$$DSCD = \sum_{i=1}^{TOA} BAMF_i \cdot MR_i \cdot N_i \cdot \Delta h_i - \sum_{i=1}^{TOA} BAMF_{0i} \cdot MR_{0i} \cdot N_i \cdot \Delta h_i \tag{3.9}$$

where i represents the vertical grid with grid cell heights of Δh_i, and air molecule concentrations N_i. $BAMF_{0_i}$ and $BAMF_i$ are the box airmass factors of the solar reference and the nadir observations at grid altitude i.

Utilizing Equation 3.8 and rearranging Equation 3.9 results in a solution for the average mixing ratio:

$$\overline{MR} = \frac{DSCD - \sum\limits_{i=1}^{TOA} dBAMF_i \cdot MR_{0i} \cdot N_i \cdot h_i}{\sum\limits_{i=1}^{TOA} BAMF_i \cdot S_i \cdot N_i \cdot h_i} \tag{3.10}$$

where $dBAMF_i = BAMF_i - BAMF_{0i}$ is the differential box air mass factor.

Some plumes were so optically thick that the mini-DOAS was not sensitive to the lowest portions of the smoke. Therefore, areas of the plume where the calculated BAMF was less than 0.25 were omitted from this retrieval to ensure that these areas did not influence the mixing ratio calculation. However, these portions were still considered for the VCD calculation.

HCHO VCDs were calculated for all mini-DOAS DSCD observations from 21 different overpasses. These retrievals rely on the independently calculated BAMFs of each observation and the profile shape from the LIDAR instrument. Photolytic profiles from PACT-1D were used to represent the plume shape of HONO for VCD calculations of the two plumes modelled thus far (Section 5.6).

3.5 Normalized Excess Mixing Ratios and Emissions

One purpose of this study is to calculate HONO emissions and determine what information can be gathered from RS observations without accounting for RT effects (*e.g.* Theys et al. 2020). This was done by calculating and comparing HONO NEMRs and EFs from mini-DOAS and in-situ data. The first step in this comparison is determining how to obtain comparable data from RS and in-situ observations. Theys et al. (2020) utilized DSCD ratios to account for plume concentration ratios. This assumption is tested here.

3.5.1 DSCD Ratios

As the DSCDs retrieved from observations of young smoke are dominated by the high trace gas concentrations inside the plume, we assume that a DSCD ratio is roughly equal to a concentration ratio (Theys et al., 2020), assuming that the trace gases are co-located inside the plume. Therefore, the DSCD ratio can approximate Equation 1.1:

$$\frac{DSCD_X}{DSCD_Y} \sim NEMR_{X/Y}. \tag{3.11}$$

This assumption was tested by comparing in-plume DOAS retrievals with in-situ data. There are three trace gas ratios considered for this comparison; HONO to HCHO, NO_2 to HCHO, and HONO to NO_2. Although, HCHO is not conserved, as would be ideal for an NEMR calculation, the comparison is restricted by the gases the Mini-DOAS can accurately measure in the same wavelength range. HCHO undergoes slower chemistry than HONO and NO_2, and this chemistry will be accounted for in Section 3.5.2, allowing for the use of HCHO as a tracer.

Observations of small agricultural fires in the Southeastern United States can be used to validate this assumption. These fires were small, and the Mini-DOAS generally viewed in a near-limb geometry. The size and consistent measurement angle make these fires ideal for comparison, as the Mini-DOAS observations were mostly sensitive to the same areas of the smoke as sampled in-situ.

However, as opposed to in-situ NEMRs, the DSCD ratio does not account for background trace gases. Although this had little impact for Western wildfires, this affected the ratios for small, low altitude fires in the Southeast where there is likely more HCHO in the background atmosphere. Therefore, mini-DOAS observations of HONO/HCHO and NO_2/HCHO were generally lower than those calculated in-situ. It might be possible to correct for this with RT modelling, but it is very difficult to model this geometry, *i.e.* a small plume dispersing vertically (Figure 2.3). Also, the purpose of the DSCD ratios is their ease of use. Therefore, these fires were only used to validate the HONO:NO_2 ratio.

To validate the HCHO-based DSCD ratios, in-plume transects from Western wildfires were utilized. The mini-DOAS recorded in-plume measurements in the nadir, limb/near-limb, and the zenith. Again, the purpose of this comparison is not to account for the radiative transfer, but to see how accurate the simple approximation of DSCD ratios is, so the impact of viewing angles is not considered in this comparison.

NEMRs were calculated for each in-plume transect with in-situ data from CAMS (Section 2.2.4) for HCHO and ACES (Section 2.2.5) for HONO and NO_2. All available data from each transect was fit with a mean bivariate error weighted regression (BEWR). The comparable Mini-DOAS data was chosen as the maximum HONO to HCHO and NO_2 to HCHO ratios from each transect, generally from the center of the plume. Considering the averaged nature of the 5 second integrations from the mini-DOAS, these single RS observations should be an accurate representation of the plume.

This temporal resolution also makes it difficult to perform a regression on mini-DOAS data, as there is too little data. Lastly, that the mini-DOAS data are measured in the same spectrum removes any impact of temporal bias between two systems. Taking the maximum data point from each transect thus gives the truest view of the center of the plume. As both HONO and NO_2 undergo fast photolysis, the Mini-DOAS HONO to NO_2 ratio was taken as the mean of all smokey data from a given transect, determined from high HONO, NO_2, and HCHO DSCDs and the color index.

Each of the comparisons can be seen in Figures 3.4, 3.5, and 3.6. For each of the three ratios, the bias between the DSCD ratios and in-situ NEMRs is small (Table 3.2), and the standard deviation is slightly higher than the sum of squares of the respective uncertainties, likely due to the ignored effects of radiative transfer and chemistry.

The slope and intercept for these three ratios were derived from a BEWR of in-situ

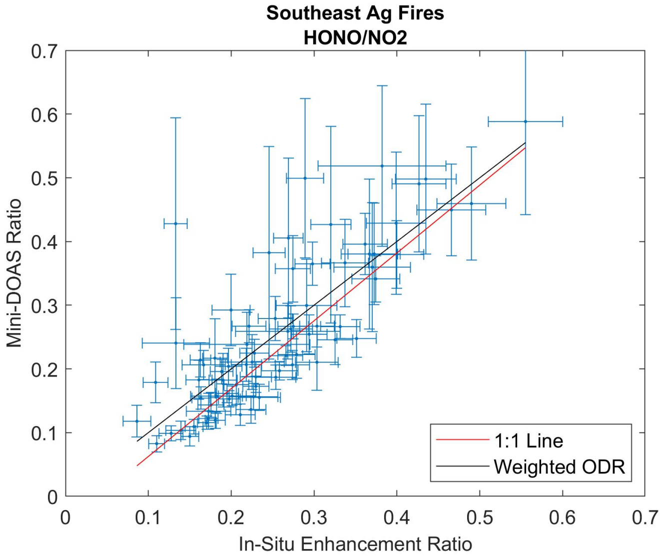

Figure 3.4: Comparison of in-plume HONO to NO_2 DSCD ratios with in-situ NEMRs from ACES measurements of HONO and NO_2 for observations of Southeastern agricultural fires.

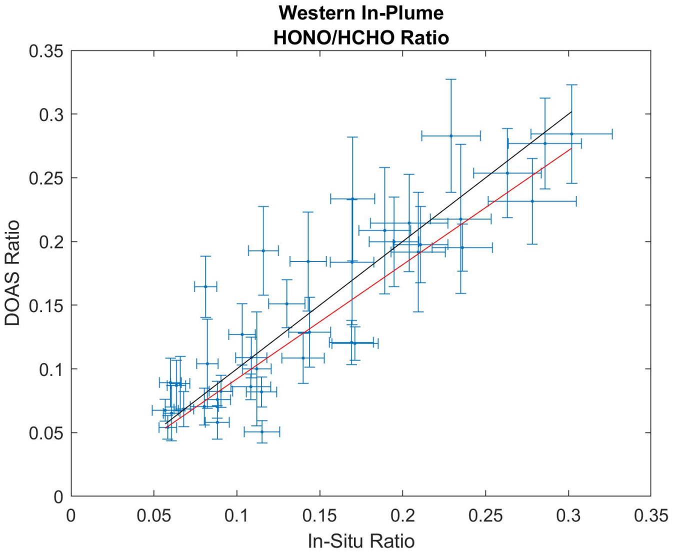

Figure 3.5: Comparison of in-plume HONO to HCHO DSCD ratios with in-situ NEMRs for observations of Western wildfires.

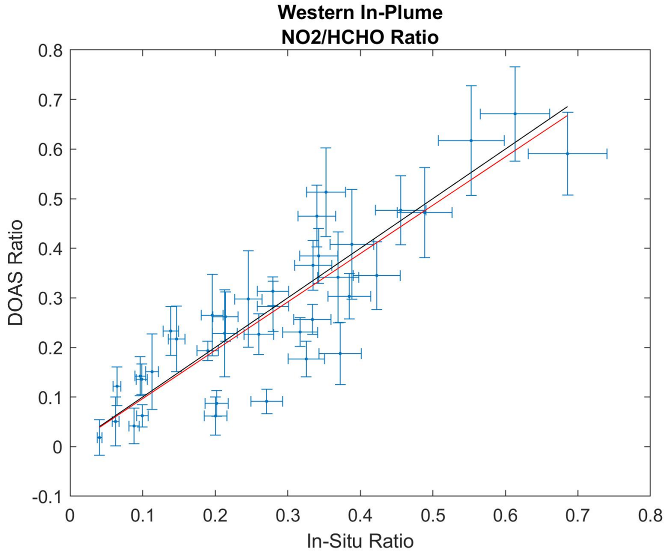

Figure 3.6: Comparison of in-plume NO_2 to HCHO DSCD ratios with in-situ NEMRs for observations of Western wildfires.

NEMR	N	Bias	Standard Deviation	Slope	Intercept	R^2
HONO/HCHO	40	+0.2%	23%	0.92 ± 0.07	1.2×10^{-2}	0.79
NO_2/HCHO	38	−2.8%	29%	0.98 ± 0.06	-8×10^{-4}	0.77
HONO/NO_2	61	−7.9%	20%	1.005 ± 0.06	-2×10^{-2}	0.72

Table 3.2: Comparison of in-situ NEMR calculations to in-plume mini-DOAS DSCD ratios to validate the use of DSCD ratios. The statistics shown are the DSCDs ratios compared to the in-situ NEMRs, *e.g.* the standard deviation is between the two calculations.

NEMRs to DSCD ratios. In this case, it was not a mean BEWR, as data with large errors should have less significance on these fit results. For these three ratios, the fits suggest agreement within 10% and suggest that the DSCD ratios under approximate the NEMR at high values for the HCHO-based ratios. This could be a RT impact, or due to the 5-second averaging of the mini-DOAS data. Regardless, this uncertainty is within the uncertainty of the DSCD ratios. These comparisons show that the DSCD ratio is a good approximation of the corresponding NEMR. As such, the DSCD ratio will be used to calculate HONO emissions and study downwind chemistry in this thesis, and the DSCD ratios will be referred to as NEMRs in the next section.

3.5.2 DSCD Ratios to Emission and Enhancement Factors

One option to quantify HONO emissions is by calculating a ER_{HONO/NO_2}. This parameter has been used in other studies (Yokelson et al., 2009), and can be calculated entirely from RS data. This could be a large benefit of future satellite observations of BB plumes. As seen in Figure 3.4, the DSCD ratio approximates $NEMR_{HONO/NO_2}$ well, and can easily be calculated. These emissions will be quantified and shown in Section 4.2. However, NO_2 emissions are also variable, so it is important to quantify the HONO emission factor.

Although the $NEMR_{HONO/HCHO}$ is helpful to understand plume emissions and chemistry, this is not a parameter used in other studies, as HCHO is not non-reactive. Accounting for HCHO chemistry makes it possible to quantify HONO emissions and better study downwind HONO chemistry. HCHO reacts slowly in young plumes (*e.g.* less than 3 hours old), and this chemistry can be accounted for.

By calculating an enhancement factor (EnF) of HCHO in smoke plumes, a HCHO-based NEMR can be converted by combining equations 1.1 and 1.2 to get:

$$EnF_X = NEMR_{X/Y} \cdot EnF_Y \cdot \frac{MW_X}{MW_Y}. \tag{3.12}$$

This results in a HONO EnF, thus allowing for the calculation of HONO emissions with a more common parameter. Calculating a smoke age dependent EnF_{HCHO} also removes the impacts of HCHO chemistry from the resulting EnF_{HONO}, creating a parameter that is only dependent upon HONO chemistry.

HCHO is a byproduct of organic oxidation inside smoke plumes. The EnF_{HCHO} therefore generally increases as a function of plume age, particularly in the first few hours after emission. To account for this chemistry, in-plume EnF_{HCHO} observations for smoke younger than 3 hours were fit as an exponential function of smoke age using a mean BEWR (Figure 3.7). This was done for each overpass with in-situ observations from within an hour of the overpass. The uncertainty of this fit was taken as the standard deviation between the fit line and EnF_{HCHO} observations. In cases where there were fewer than 5 in-situ observations, the mean EnF_{HCHO} was used and the uncertainty was increased by 50%.

The corresponding EnF_{HCHO} for each mini-DOAS $NEMR_{HONO/HCHO}$ observation was calculated with the fit and the smoke age of the mini-DOAS observation. As can be seen in Figure 3.7, there is little change in HCHO over the first 2 hours in this plume. As a result, a EF_{HCHO} could also have been calculated from the youngest smoke observations in order to calculate HONO emissions from mini-DOAS data. However, accounting for the smoke age dependence of HCHO also results in a parameter that can be used to study downwind HONO chemistry.

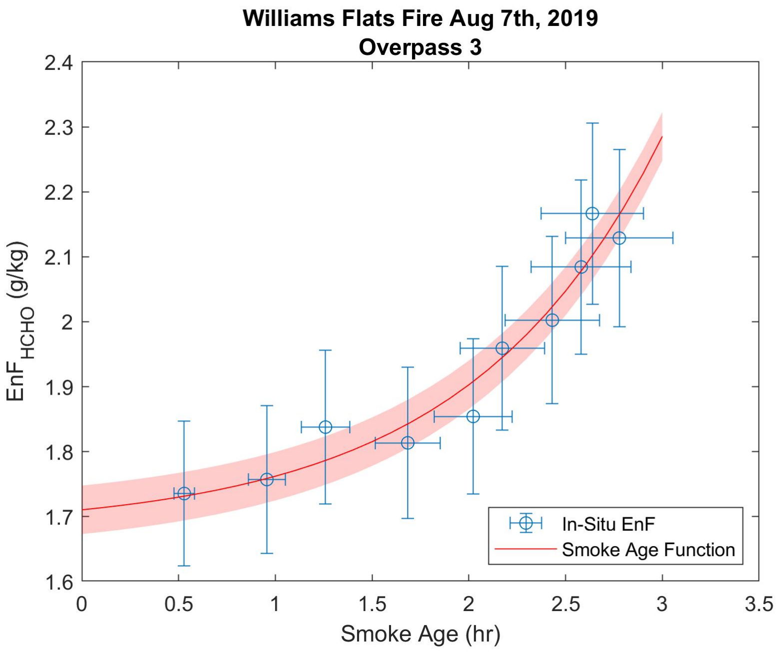

Figure 3.7: Example of the smoke age dependence of the HCHO enhancement factor. This case shows the clear exponential dependence used to calculate the function (red line) and uncertainty (red shading).

As the resulting EnF_{HONO} was derived from overpass observations, it is dependent upon the RT and chemistry of the plume. The best opportunity to validate the EnF_{HONO} is with data from a prescribed burn in the Blackwater River State Park in the Florida panhandle from August 30th, 2019. This plume had large emissions of HCHO and HONO with less optically thick smoke than many of the Western wildfires observed. This resulted in Mini-DOAS sensitivity to the entire height of the plume. Further, this plume was extensively studied via the DC-8, resulting in many in-plume observations.

This fire behaves just as expected. The first panel shows the calculated EnF_{HCHO} from in-plume transects as well as the time-dependence determined for this overpass. The second panel shows the DSCD ratio of HONO to HCHO from the mini-DOAS with the earliest observation showing the highest HONO value, which quickly decreases downwind due to HONO photolysis. The third panel shows the product of the first two panels

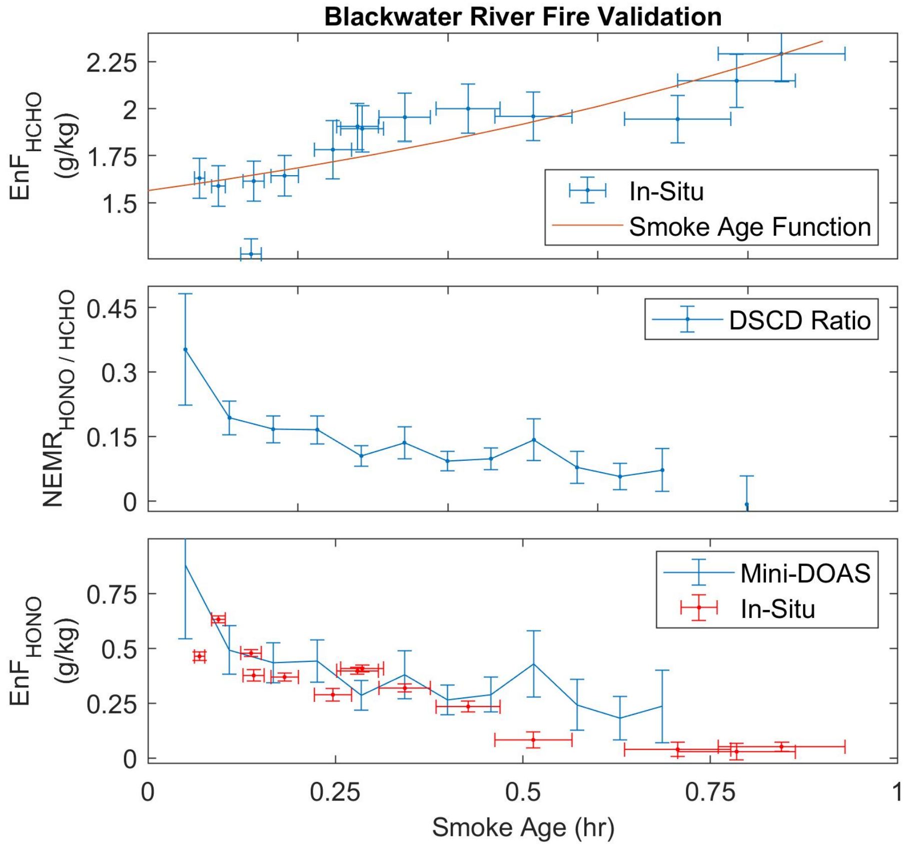

Figure 3.8: Validation of the calculation of EnF_{HONO} with mini-DOAS data. These results agree very well with the EnF_{HONO} calculated from in-plume data from ACES. Most observations are within the margin of error and a similar downwind rate of change is observed with the two systems.

after correcting for molecular weights, *i.e.* the EnF_{HONO}. Also shown is the EnF_{HONO} calculated entirely from in-situ plume transect data from ACES (in red).

This fire reveals that this method can be utilized to accurately determine HONO emissions from BB and study downwind HONO chemistry. For this illuminated plume, mini-DOAS results agree very well with in-situ observations. Therefore, differences between mini-DOAS and in-situ HONO data likely stem from changing emissions/chemistry and the fact that the two measurement techniques probe different areas of a plume. This example also illustrates that the mini-DOAS can observe younger smoke than in-situ observations and, in this case, that leads to a slightly higher observed HONO emission.

This method was used to quantify HONO emissions from 18 different plume overpasses from throughout the first half of the FIREX-AQ field campaign, along with observations of the Blackwater River State Park fire. Some overpasses were excluded due to a lack of in-situ data within an hour of the overpass or due to complications in the mini-DOAS observation (*e.g.* pyro-cumulus clouds).

CHAPTER 4

DSCD Results

4.1 Differential Slant Column Densities

Figure 4.1 shows concurrent LIDAR and mini-DOAS observations from two different plume overpasses, which were chosen for their different dynamics and consequent vertical extent. The 532 nm aerosol extinction profile from the overflight of the Shady fire plume (Figure 4.1, panel a1) was lofted above the boundary layer and remained elevated. Smoke from the Castle fire (Figure 4.1, panel a2), on the other hand, remained in the boundary layer, leading to a 2000m deep plume. The profile of the Shady fire also shows that the LIDAR instrument saturated for the densest part of the plume near the fire. The LIDAR's inability to penetrate dense and deep plumes poses a challenge, but should have minimal impact on the trace gas retrieval as long as only the upper part, i.e. the portion probed by the LIDAR, is interpreted.

The total aerosol optical depth (AOD) from the Shady fire derived from the LIDAR (Figure 4.1, panel b1) was around 3 at it's densest point near the fire and overall larger than that of the Castle fire (Figure 4.1, panel b1). The AOD in both plumes decreases with distance from the fire due to plume dilution. As a result, the CI measured by the mini-DOAS (Figure 4.1, panel c1 and c2) was also higher for the Shady fire. For both plumes, the CI follows the general pattern of the AOD, but with less variability in young smoke and slower decrease downwind. This indicates that the mini-DOAS is not sensitive to the

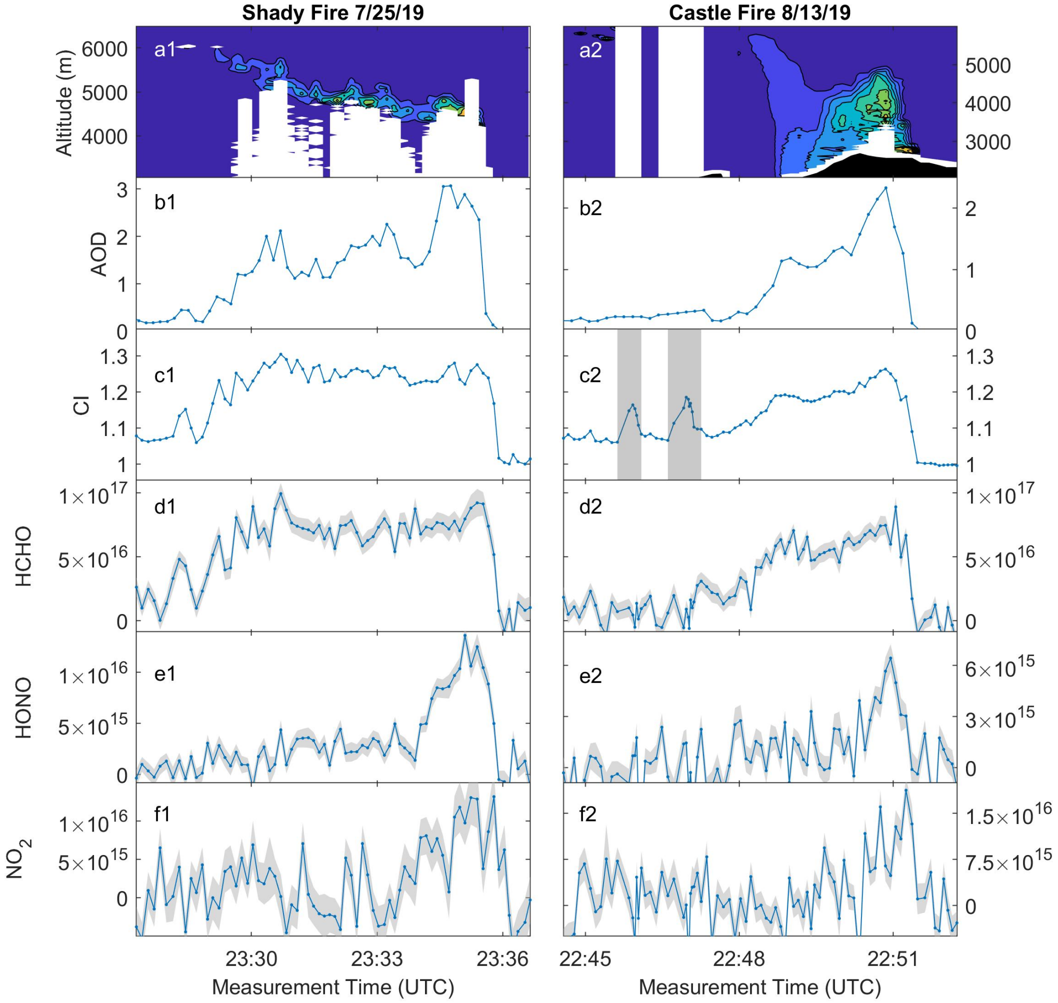

Figure 4.1: Remote sensing results from overpasses of the Shady (1) and Castle (2) fires which had different plume dynamics and emissions. DSCDs for HCHO (d), HONO (e), and NO_2 (f) are in units of molecules/cm^2 and shading denotes the measurement uncertainty. The two CI peaks for the Castle fire (c2) between 22:44 and 22:47 UTC and the missing LIDAR data are due to flying over small cumulus clouds that may have contained smoke.

entire plume, so changes in the AOD have little impact on the CI.

DSCDs for HONO (Fig. 4.1 e1 and e2) and NO_2 (f1 and f2) show highest values near the fire and decrease as the plume ages. HCHO DSCDs (d1 and d2) remain elevated for the length of the plume with a very similar pattern as the CI. The behavior of HCHO can be explained by counteracting effects of photochemical formation, dilution/chemical loss, and increased measurement sensitivity with decreasing AOD. For the Shady fire, this leads to near constant HCHO DSCDs, while there is a slow decrease for the Castle fire. Alternatively, HONO and NO_2 DSCDs decrease quickly downwind due to a combination of their fast photochemical loss and plume dilution. Photolysis and chemical loss (such as nitric acid formation) likely dominate this behavior considering the elevated AOD, CI, and HCHO DSCDs downwind.

The magnitudes of the DSCDs are also impacted by their respective emissions. For instance, the Shady fire appears to have emitted more HONO than NO_2 considering the higher DSCDs in the youngest smoke. The Castle fire appears to emit 40% less HONO than NO_2, thus suggesting much different HONO to NO_2 emission ratios. The comparison of the DSCD ratios can thus be useful for quantifying emissions and studying the downwind evolution of HONO in BB plumes.

As the plume travels downwind, photochemistry has a larger and larger effect on the vertical distribution of HONO and NO_2. Therefore, DSCD ratios become a worse approximation for NEMRs with increasing smoke age. RT modelling and chemical modelling are needed to resolve this uncertainty and properly quantify trace gases. The DSCDs however can be used to quantify emissions (Sections 3.5.2 and 4.4), and differences between the DSCD ratios and in-situ NEMRs can be used to understand plume chemistry (Section 4.4).

4.2 HONO Emissions

As discussed in Section 3.5.2, mini-DOAS measurements of HONO and HCHO can be coupled with in-situ observations of HCHO to calculate HONO emissions and study downwind evolution. The methods described in Section 3.5.2 were used on 18 different plume overpasses of 8 different fires from 10 different days. The only Southeastern fire considered was the Blackwater River State Park prescribed burn on August 30th, 2019, the rest were Western wildfires.

These 18 overpasses were selected based on low mini-DOAS uncertainties, available in-situ data, and clear observations of young smoke determined with the help of DC-8 videos (Section 2.2.12). Some fires were omitted due to pyro-cumulus clouds obscuring the view of the fire from above or low light leading to high retrieval uncertainty. Similarly, two overpasses from a wildfire in Arizona were omitted due to a dispersed burning area which led to uncertainties in the interpretation of observations, particularly as it applies to plume age. Lastly, some overpasses did not have in-situ plume transect observations within an hour of the overpass observations.

These 18 segments were analyzed to determine the EnF_{HONO} as a function of plume age from mini-DOAS data. First, the mini-DOAS observations were filtered based on the retrieved CI (Section 2.1.6) to ensure that smoke was observed. Next, data with a high absolute uncertainty of the $NEMR_{HONO/HCHO}$ DSCD ratio were removed. Lastly, the $NEMR$ was converted to a EnF with in-situ observations of HCHO, and the resulting EnF_{HONO} was again filtered based on absolute uncertainties.

Emissions were calculated as the highest EnF_{HONO} from observations of smoke with ages less than 30 minutes. Similarly, an ER_{HONO/NO_2} was calculated by averaging the

$NEMR_{HONO/NO_2}$ DSCD ratios from smoke younger than 30 minutes. The motivation for this decision can be summarized with Figure 4.2.

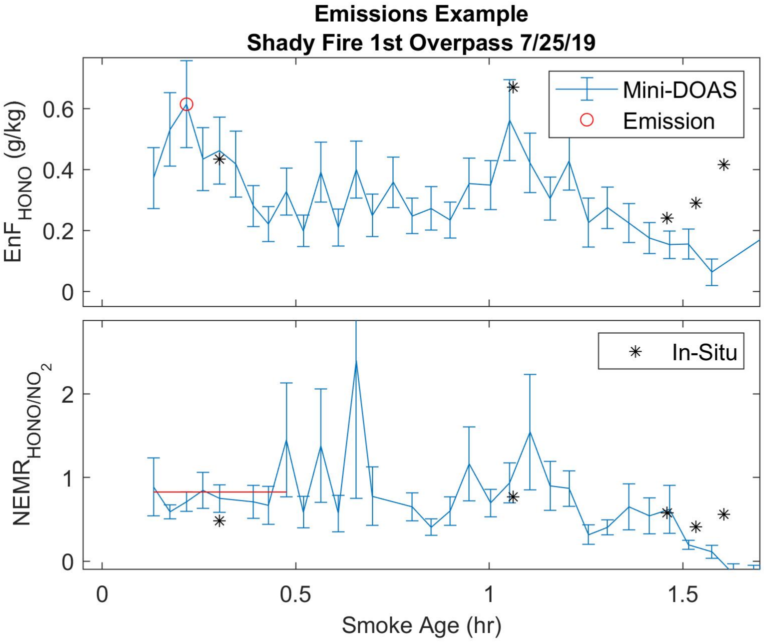

Figure 4.2: Example EF_{HONO} and ER_{HONO/NO_2} calculated from mini-DOAS data. In blue is the respective time series from mini-DOAS data, in black is the comparable in-situ observations, and red shows the emissions calculated from mini-DOAS data.

EnF_{HONO}, as observed by the mini-DOAS, is impacted by both changing emissions and fast photolysis. For instance, the high EnF_{HONO} at 1 hr smoke age is likely due to higher emissions that occurred previously and the quick decrease after roughly 15 minute smoke age is due to HONO photolysis. The increase in EnF_{HONO} for the youngest smoke in this example may also be due to changing emissions. These variabilities make it necessary to use a single data point to represent EF_{HONO}.

The bottom plot shows the ratio of HONO to NO_2 as observed by the mini-DOAS. This parameter should have much less influence from changing emissions, as that affects both NO_2 and HONO similarly. Further, in the first 30 minutes, photolysis should not have a large impact on the vertical profiles of HONO and NO_2. As seen in the figure, this ratio remains relatively constant over the first 30 minutes, hence this data was averaged to calculate ER_{HONO/NO_2}.

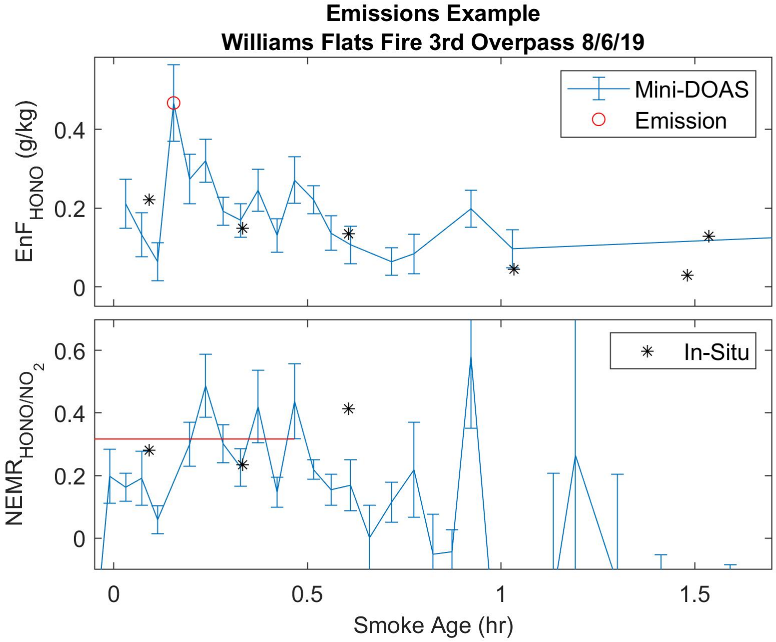

Figure 4.3: Williams Flats fire emission calculation from 8/6/2019.

This same behavior was observed in the Williams Flats fire on August 8th, 2019 (Figure 4.3). These examples display the impact that changing emissions and photolysis have on EF_{HONO} calculations, as both cases show a fast decrease downwind of the maximum EnF_{HONO}. The ER_{HONO/NO_2} appears not to be impacted by photolysis in the first 30 minutes after emission, as no consistent decrease is observed. This parameter can also be calculated with just RS data and could be very important for satellite observations of HONO emissions (*e.g.* Theys et al. 2020).

After calculating a single EF_{HONO} from each of the 18 fire overpasses, the emissions were classified based on their fuel type (Section 2.2.10) to compare the emissions with those from literature (*i.e.* Akagi et al. 2011 and Andreae 2019). The fuel type assumed for each overpass was based off of the the dominant fuel type(s) from the FCCS data, based on the emitted carbon from each fuel type. Generally, one or two specific fuels accounted for over 50% of the emissions, and Western wildfires were dominated by observations of burning timber, although the dominant timber species changed with the different fires. All of these fire overpasses were compared to emissions from temperate forests from literature.

Only one of the 17 Western wildfire overpasses was defined as burning grassland and shrubland. Also categorized with this overpass was the overpass of the Blackwater River State Park prescribed burn, which was most closely related to a savanna ecosystem. These overpasses were compared to literature for "Savanna and Grassland" (Andreae, 2019) as well as Akagi et al. (2011) emissions from "Savanna" and "Chaparral."

There is very good agreement between mini-DOAS data and Akagi et al. (2011) for temperate forests. The mini-DOAS retrieved a mean EF_{HONO} of 0.54 g/kg with a standard deviation of 0.22 g/kg which is similar to 0.52 ± 0.15 g/kg from Akagi et al. (2011). The emissions from Akagi et al. (2011) also fall within the margin of error of the mini-DOAS with a value of 0.33 ± 0.17 g/kg. These results can be seen in Figure 4.4.

For grassland/shrubland mini-DOAS retrieved HONO emissions of 0.79 g/kg which is higher than "Savanna" value of 0.2 g/kg from Akagi et al. (2011), shown as the single, blue point on this figure as it was from a single observation, as well as the Akagi et al. (2011) value for "Chaparral" of 0.41 ± 0.15 g/kg and the Andreae (2019) value for "Savanna and Grassland" of 0.47 ± 0.21 g/kg. However, with only 2 mini-DOAS observations, it is difficult to gather much information from this comparison.

HONO emissions were also calculated with in-situ observations from the ACES instrument. As with the in-situ data used to calculate EnF_{HCHO}, in-situ observations of EnF_{HONO} must be made within an hour of the plume overpass in question. To account

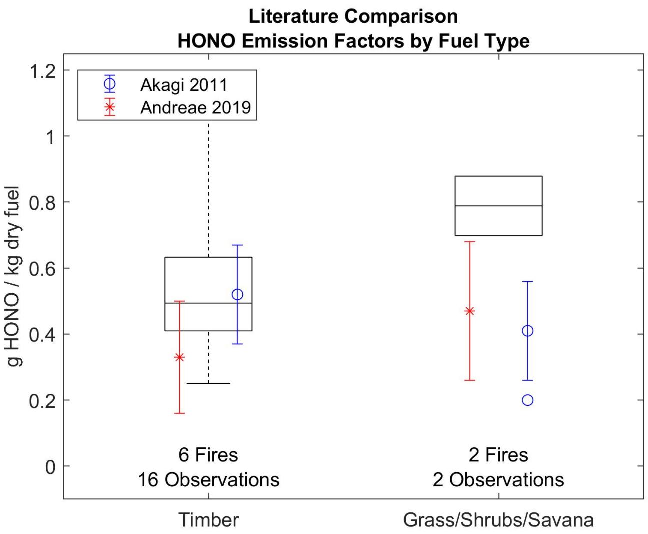

Figure 4.4: HONO EFs by fuel type measured by the mini-DOAS and comparison with values from literature. On average, mini-DOAS emissions are higher than those from literature but within the margin of error.

for HONO photolysis, observations were filtered for photochemically young smoke. Using the meteorology corrected smoke age, the in-situ data was filtered for all smokey observations where the in-situ HONO photolytic lifetime, measured via CAFS (Section 2.2.7), was larger than the age of the smoke in order to minimize the impact of photolysis.

HONO photolysis was also accounted for by creating a second dataset from ACES observations using a simple photolysis approximation. A mean photolysis rate was created for each ACES observation by assuming that the photolysis at the time of emission was 1×10^{-4} s^{-1}, which is a very slow HONO photolysis rate that was observed in a few very thick plumes. It was then assumed that the photolysis rate changed linearly from the time of emission to the time of observation, *i.e.* the photolysis rate was averaged between the in-situ j_{HONO} observations (from CAFS) and 1×10^{-4}. Each ACES observation was corrected using this mean photolysis rate and the smoke age. This photolysis correction is rather simple, but it is a good approximation for the impact of photolysis. Photolysis is much more difficult to correct for in mini-DOAS data, as DSCDs depend on the photolysis profile through the smoke for separate locations than the j_{HONO} values were observed. It therefore will not be corrected for in this comparison.

The in-situ EF_{HONO} was calculated using the described subset of ACES data, both observed and photolysis-corrected, utilizing a mean BEWR. Four plumes did not have enough observations of photochemically young smoke to calculate EF_{HONO}. Of the remaining 14 overpasses, the mean mini-DOAS emissions are nearly halfway between the in-situ EF_{HONO} and the photolysis-corrected EF_{HONO}.

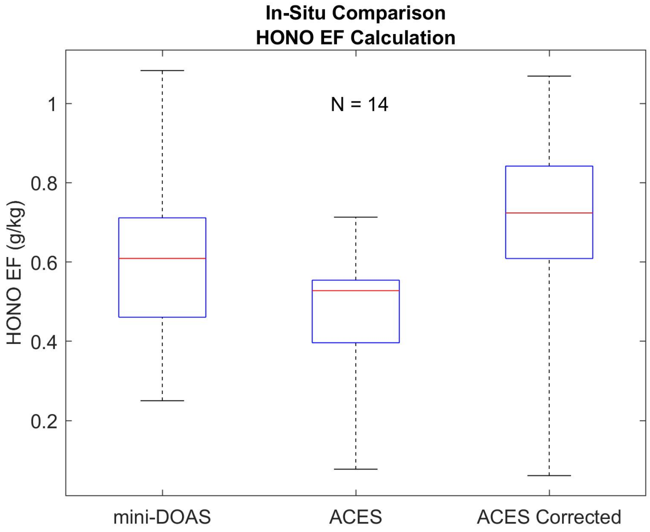

Figure 4.5: Comparison of HONO emissions measured by the mini-DOAS with in-situ observations of young smoke and photolysis corrected emissions. Campaign average Mini-DOAS emissions fell between the in-situ and photolysis corrected values.

The campaign averages from these two in-situ emissions calculations can be seen in Figure 4.5 compared to the mini-DOAS retrieved emissions. For these 14 overpasses, the mini-DOAS observed HONO emissions of 0.6 ± 0.24 g/kg, compared to an in-situ value of 0.46 ± 0.17 g/kg and a photolysis corrected value of 0.68 ± 0.27 g/kg.

Similarly, the ACES instrument can also be used to calculate ER_{HONO/NO_2}, which is a useful parameter to normalize HONO emissions against fuel nitrogen content. This calculation was made with the same subset of ACES data as used for the EF_{HONO} calculations. However, this calculation did not include any photolysis correction, as $NEMR_{HONO/NO_2}$ is a more stable parameter (seen in Figure 4.2) due to the photochemistry of both species and the short time scales considered. There are some issues in this assumption, but accounting for NO_2 plume chemistry is well beyond the scope of this work. Additionally, the mini-DOAS ER_{HONO/NO_2} was averaged over the first 30 minutes after emission, and should have observed similar photochemistry as the in-situ observations. For this example, 6 overpasses were omitted due to a lack of photochemically young observations and NO_2 data.

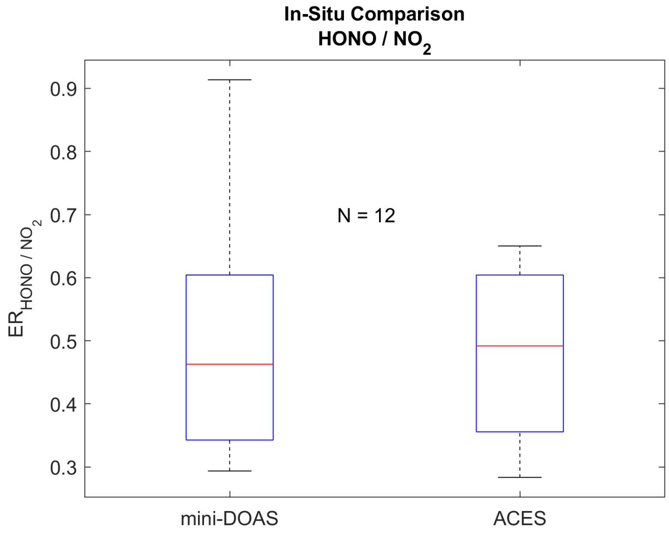

Figure 4.6: Comparison of the HONO to NO_2 emission ratios measured with the mini–DOAS and in-situ show good agreement between the campaign averages. The higher variability of mini-DOAS data is largely due to higher measurement uncertainty.

The resulting comparison between mini-DOAS and ACES ER_{HONO/NO_2} can be seen in Figure 4.6. On a campaign average, the two agree very well. The mini-DOAS observed a mean ratio of 0.49 ± 0.19 compared to the ACES average of 0.47 ± 0.13.

4.3 Emission Discussion

These comparisons indicate the utility of RS to measure HONO emissions. On average, mini-DOAS measured HONO emissions were slightly higher than values from literature. This is likely due to the fact that photolysis had a smaller impact on mini-DOAS observations than in-situ observations of HONO emissions. This finding should motivate future RS observations of BB emissions.

The ER_{HONO/NO_2} provides a useful parameter for RS observations of HONO emissions, as it does not require any in-situ data and there appears to be little change in the ratio over the first 30 minutes after emission. Therefore, satellite observations should be capable of measuring ER_{HONO/NO_2}, although the impact of pixel size should be considered. This offers exciting potential to monitor HONO emissions from BB on a larger scale than has previously been possible. However, NO_2 emissions and early chemistry in plumes are variable, and these factors must be considered when using the ER_{HONO/NO_2}. Therefore, it is preferable to use an emission factor which provides a better representation of HONO emissions.

The benefit of accounting for HCHO chemistry by calculating a plume age dependent EnF_{HCHO} (Section 3.5.2), as opposed to just HCHO emissions, is that it allows for the study of downwind HONO chemistry. The resulting EnF_{HONO} is only dependent on HONO emissions and chemistry, albeit for the areas of the plume that the mini-DOAS is sensitive to.

Figure 4.7 shows an example EnF_{HONO} time series from mini-DOAS data for the Williams Flats fire. This figure shows the impact that changing emissions has on HONO in BB plumes, particularly if coupled with the MASTER fire radiative power shown in

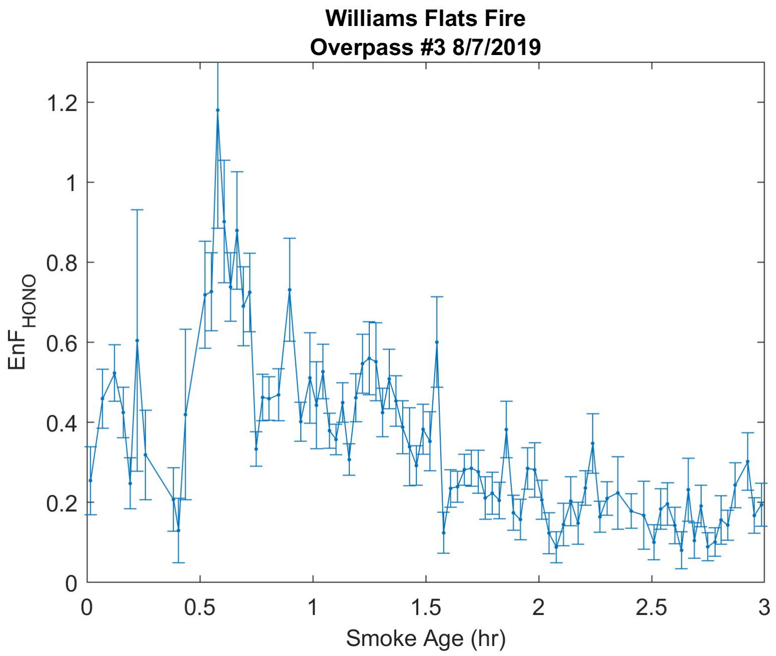

Figure 4.7: The evolution of EnF_{HONO} for three hours after emission in the Williams Flats fire on 8/7/2019.

Figure 4.8. This image is from the same plume overpass, where red colors indicate intense burning and dark/cool colors indicate smoldering fires. The lower HONO values in the youngest smoke seen in this overpass are related to emissions from the cooler burning areas toward the left of the MASTER image. The highest HONO values (at roughly 35 minutes downwind) are likely more indicative of the large flaming area seen in the top center of the MASTER image. This shows the difficulty of calculating the smoke age from large fires, as the highest HONO values at 35 minutes downwind are likely not observations of 35 minute old smoke but are due to representing the fire as a point source. Another issue illuminated by this example is the variability of burning conditions in fires which impacts the emission of HONO.

This example also shows that HONO emissions change as a function of time. After the peak HONO value, there is an exponential decrease downwind due to photolysis.

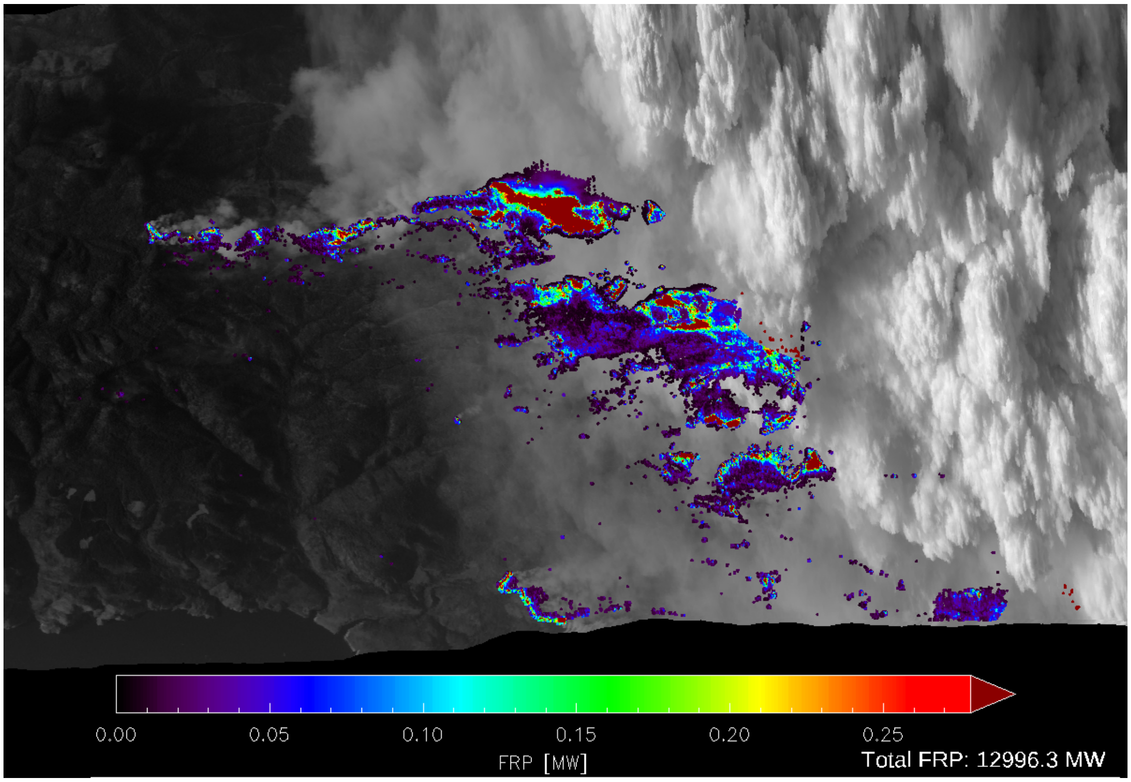

Figure 4.8: MASTER (Section 2.2.11) fire radiative power image from the overpass shown in Figure 4.7.

However, there are several areas of decreased or increase HONO relative to this change. For example, there is a local minimum HONO value around 45 minutes and a local maximum at 75 minutes downwind. These fast changes in HONO amounts are likely driven by changes in HONO emissions. This example, coupled with the variability of the individual EF_{HONO} calculations, underscores the variability of HONO emissions, the effect that has on the amount of HONO in young smoke, and the ability of RS to observe these changes as smoke travels downwind.

4.4 Downwind Ratios

The EnF_{HONO} from Figure 4.7 was of a thick plume, where the mini-DOAS was only sensitive to the uppermost portions of the smoke and the results are not indicative of HONO further into the plume. Utilizing mini-DOAS observations with in-situ observations can provide information on the vertical structure of HONO inside a plume. For instance, overpass mini-DOAS observations of a thick plume inform the $NEMR_{HONO/NO_2}$ for the illuminated, upper portions of the plume while in-situ observations depict the ratio further into the smoke. Theys et al. (2020) utilized TROPOMI to study HONO to NO_2 ratios in smoke as it travelled downwind, but did not consider the impacts of photochemistry on this ratio. As smoke travels downwind, the vertical profiles of these two trace gases will likely differ due to differing photochemistry. FIREX-AQ provided an opportunity to study the impact of this chemistry on satellite observations and the accuracy of the assumption from Theys et al. (2020).

4.4.1 Overpass Observations

This was done by comparing the $NEMR_{HONO/NO_2}$ from overpass DSCD ratios to in plume data calculated with observations from the ACES instrument. The two datasets were compared as a function of smoke age, calculated based on the distance from the fire and mean wind speed for both data sets.

The first case considered here is from the first overpass of the prescribed burn in the Blackwater River State Park in Florida. This fire was measured earlier in the day than any Western wildfire and was also the fire with the lowest latitude measured throughout the FIREX-AQ campaign. Additionally, the peak 532 nm AOD in this plume was less than 2, which is lower than most of the Western wildfires. The combined impact of these effects was that this BB smoke plume received more solar irradiance than many of the Western wildfires measured.

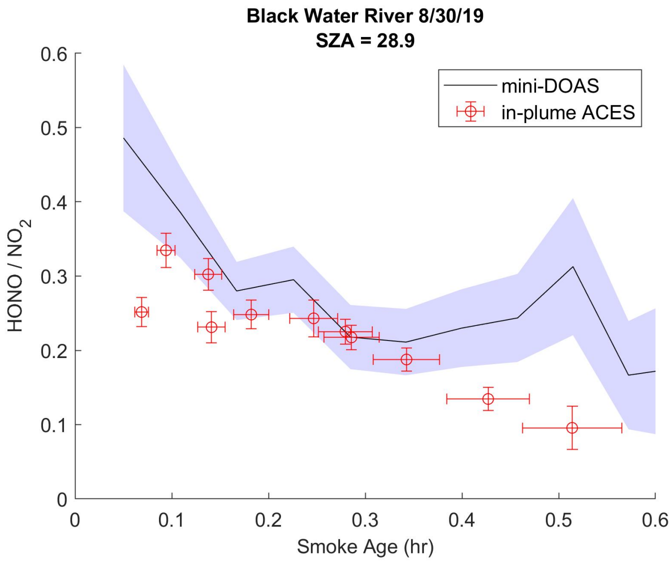

Figure 4.9: Observations of the $NEMR_{HONO/NO_2}$ in an optically thin and well illuminated plume show a similar trend and good agreement between overpass mini-DOAS data and in-plume ACES observations.

Figure 4.9 shows the impact that these conditions had on HONO to NO_2 ratios. For much of the plume, the overpass and in-situ ratios agree closely and see a similar rate of change early in the plume. This indicates that photochemistry is occurring throughout the plume, as the ratios at a specific altitude are similar to the averaged ratios from the mini-DOAS. This also indicates that photolysis has a larger impact on HONO early in this plume due to the photochemical sources of NO_2 in the plume, such as radical chemistry converting NO to NO_2.

Similarly, the single overpass of the Tucker fire also shows good agreement with the in-plume HONO to NO_2 ratios, although it is for a different reason. In this case, the fire was observed late in the day, with a SZA of roughly 80° during the overpass and the in-plume

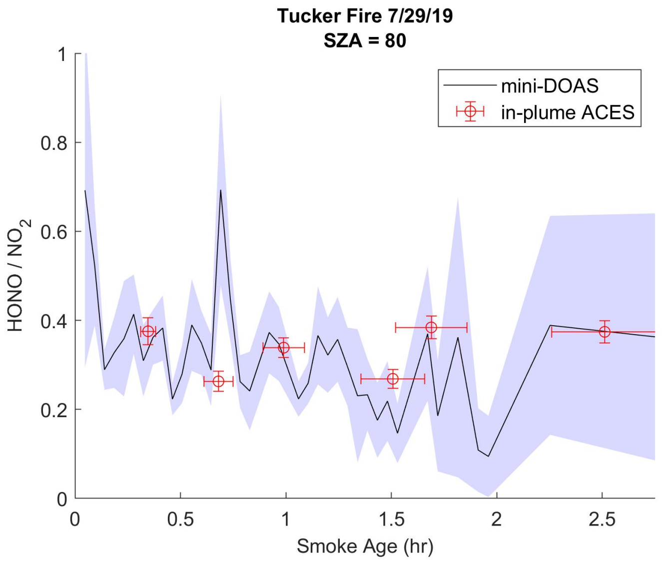

Figure 4.10: HONO to NO_2 ratios agree well between mini-DOAS and in-situ observations and remain relatively constant downwind for a high SZA scenario.

measurements proceeding the overpass. Therefore, photolysis likely had little impact, even at the top of the plume. One piece of evidence to support this is the much slower decrease in the HONO to NO_2 ratio as a function of plume age. With slow photolysis, the HONO to NO_2 ratio of the upper part of the plume agreed with the HONO to NO_2 ratio further into the plume, measured in-situ.

This indicates that for observations at high SZA, and thus low photolysis rates, remote sensing observations of HONO to NO_2 ratios are a good representation of the ratio deeper in the plume due to consistent photochemistry. However, TROPOMI does not measure the continental US during high SZAs due to its early afternoon overpass time, so this finding is less consequential for some satellite observations. Although, similar observations were found in optically thin plumes, due to the increased sensitivity to the entire plume by the mini-DOAS and increased photolysis lower in the plume.

Figure 4.11 shows an overpass of the Williams Flats fire where the overpass and in-situ

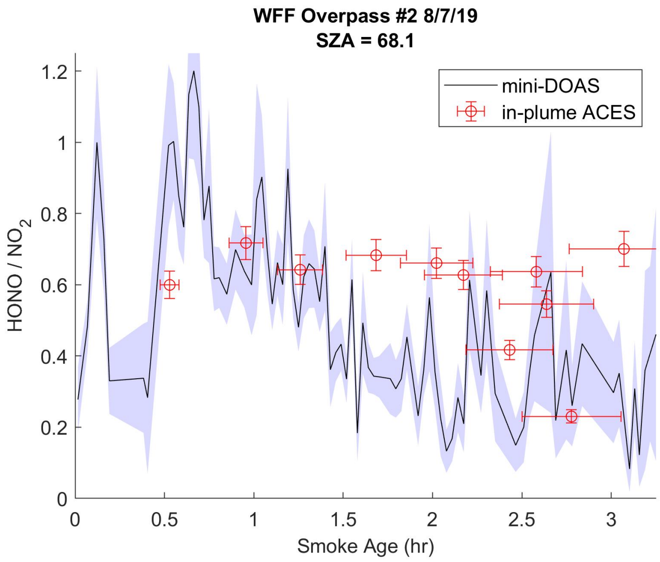

Figure 4.11: The HONO to NO_2 ratio shows poorer agreement between mini-DOAS and in-situ data due to HONO photolysis in the upper portion of the plume.

data do not agree. This was a very optically thick plume, with a maximum 532 nm AOD over 8, and the mini-DOAS was only sensitive to the upper portion of the plume with no sensitivity to the lower portion.

As such, the mini-DOAS measured the area of the plume impacted by photolysis. This is seen in this figure as the mini-DOAS HONO to NO_2 ratio observed during the overpass decreases with smoke age. However, this trend was not observed in the in-situ data, where the HONO to NO_2 ratio is almost constant for a majority of in-plume transect observations. Similar relationships were also seen in other fire overpasses of thick plumes.

In this case, the HONO profile shape changed as a function of plume age, with HONO in the middle of the plume remaining relatively unchanged and HONO at the top of the plume decreasing due to photolysis. This photolytic loss also occurs more quickly than losses of NO_2 in the illuminated portion of the plume. Therefore, overpass RS observations of HONO to NO_2 ratios in illuminated, optically thick plumes are not a good representation of the total plume chemistry.

Satellite observations, particularly from TROPOMI (Theys et al., 2020) which has an early afternoon overpass time, need to consider the optical depth of smoke plumes with HONO to NO_2 observations. For thin plumes, this ratio appears to represent the entire plume. For thicker plumes, this ratio clearly only represents the upper portion of the smoke.

4.4.2 In-Plume Observations

Just as differences between the overpass DSCD ratios and in-plume NEMRs can be used to study plume photochemistry, so too can in-plume mini-DOAS observations. Based on the viewing angle, mini-DOAS observations have different sensitivity to different regions of the plume. If viewing in the zenith or limb/near-limb, the mini-DOAS will still have more influence from the top of the plume. Alternatively, in-plume observations in the nadir will have some sensitivity to the lower portion of the plume, but unfortunately, there were few in-plume nadir observations with concurrent ACES observations to study here. Thus, in this section, differences between mini-DOAS and in-situ observations also inform on the photochemistry occurring in the upper portions of plumes.

Again, the first case to consider is from the Blackwater River State Park prescribed burn (Figure 4.12). During these transects, the mini-DOAS viewed in the limb. Just as in Figure 4.9, the RS and in-situ ratios agree well. This is further evidence that photochemistry occurred throughout this plume and there seems to be little altitude dependence on HONO to NO_2 ratios.

A very different relationship was observed for the Williams Flats fire on August 7th.

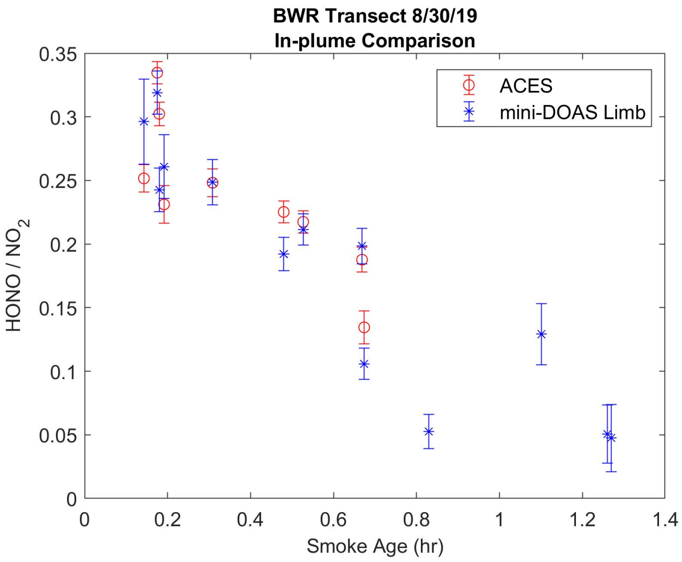

Figure 4.12: In-plume HONO to NO_2 ratios show excellent agreement between mini–DOAS and in-situ observations for an optically thin plume.

This fire was very optically thick, requiring that mini-DOAS measurements were observed in the zenith to ensure enough light reached the telescopes. Therefore, these observations were much more sensitive to the upper portion of the plume. For the second transect of this fire (Figure 4.13, right), the plume behaved as it did in the preceding overpass (Figure 4.11). The mini-DOAS observations were lower than in-situ ratios for the first 2 hours after emission, indicating lower HONO to NO_2 ratios in the upper part of the plume and a greater impact from HONO photolysis in the upper portion of the plume. After 2.5 hours, the plume appears to have thinned enough that photolysis has impacted the in-plume HONO to NO_2 ratio and we find better agreement with the mini-DOAS observations. However, the earlier in-plume transects showed the opposite behavior (Figure 4.12, left). During these transects, there were several observations of higher ratios from the mini-DOAS than measured in-situ, indicating higher HONO to NO_2 ratios above the aircraft.

However, the earlier in-plume transects showed the opposite behavior (Figure 4.12,

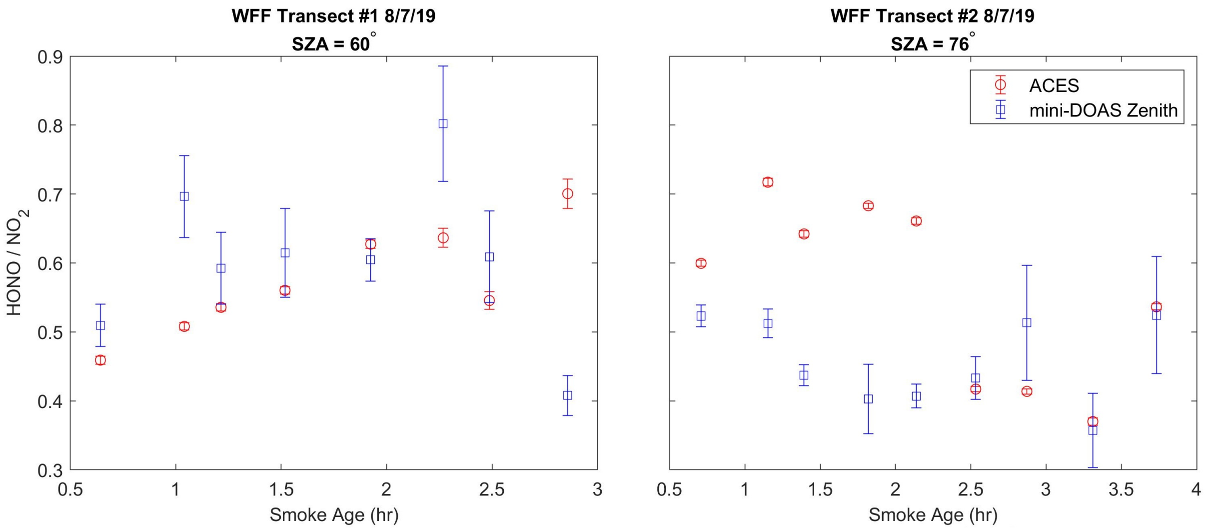

Figure 4.13: HONO to NO_2 ratios reveal two different chemical regimes for two different in-plume transects of the Williams Flats fire on August, 7th. The second transect (right) shows the relationship seen previously, with lower HONO to NO_2 ratios at the top of the plume. However, the first transect (left) indicates higher HONO to NO_2 ratios at the top of the plume.

left). During these transects, there were several observations of higher ratios from the mini-DOAS than measured in-situ, indicating higher HONO to NO_2 ratios above the aircraft. This finding may stem from emissions, as suggested with Figure 4.14. For observations from the first 2.5 hours of the earlier in-plume transects, the enhancement of mini-DOAS compared to in-situ $NEMR_{HONO/NO_2}$ was negatively correlated with the observed MCE (R^2 of 0.71). In other words, the lower MCE resulted in a lower in-situ NEMR compared to the mini-DOAS. Therefore, the colder emissions with a lower MCE lofted lower into the atmosphere than the higher MCE smoke that contained a higher HONO to NO_2 ratio. Since this plume was so thick and there was little photochemistry, this plume retained this trace gas emission signature. There are other possibilities, such as photo-enhanced heterogeneous HONO production, although this seems unlikely given the magnitude of the difference.

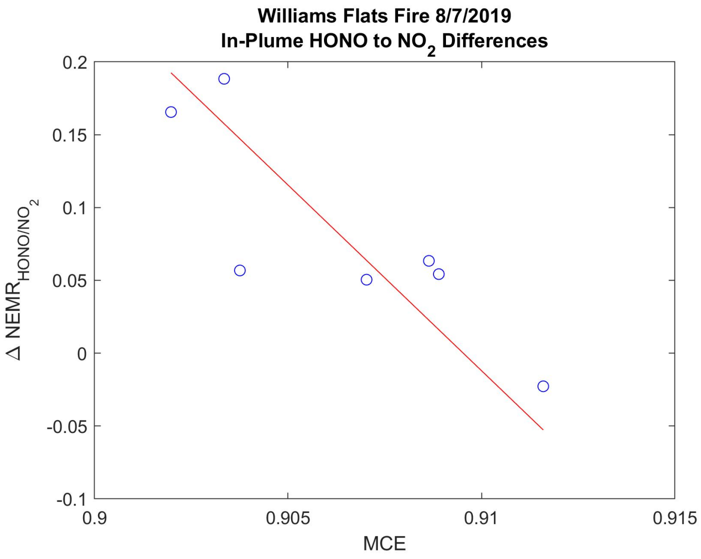

Figure 4.14: The difference between the $NEMR_{HONO/NO_2}$ measured by the mini-DOAS and in-situ is negatively correlated with the in-situ MCE ($R^2 = 0.71$).

This was a particularly thick plume with several emission sources and is further evidence of the extreme variability of BB plumes. In the same plume, over the span of several hours, the plume exhibited very different vertical structure. The causes of this variability are beyond the scope of this work, but are interesting to note. Clearly, HONO to NO_2 ratios do not remain constant through a plume for a variety of reasons. Past and future observations of these ratios therefore need to consider the portion of the plume that measurements are sensitive to.

CHAPTER 5

Radiative Transfer Results

RT calculations were performed for 21 different plume overpasses from FIREX-AQ by constraining VLIDORT-QS as explained in Section 2.3.3. Other overpasses were not considered due to extenuating circumstances, such as clouds obscuring young smoke. For each mini-DOAS observation from these overpasses, a BAMF was calculated using the RTM. The resulting BAMFs were then used to determine plume VCDs and the measurement sensitivity of the mini-DOAS. These model results were essential to understanding remote sensing observations of smoke and are needed to provide guidance for future remote sensing capabilities. Before analyzing the RT results needed for the trace gas retrievals, the initialization of the RTM and the description of the plume aerosols in the model was tested by comparing observed and modelled CIs.

5.1 Color Index Validation

As the CI (Equation 2.1) depends on the number, size, and optical properties of the particles in BB plumes, it provides a unique tool to optimize and validate the RTM. It should be noted that one κAE was determined and updated for each plume overpass to best represent the CI for the entire overpass. However, the retrieved campaign average κAE of 7 agrees well with the existing literature on BB smoke (Sumlin et al., 2018; Pokhrel et al., 2016; Chakrabarty et al., 2010; Chen and Bond, 2010). Also, as can be seen in Figure 2.11, the CI witnesses considerable variability unrelated to the κAE. Therefore, the CI can be used to validate the RTM methods.

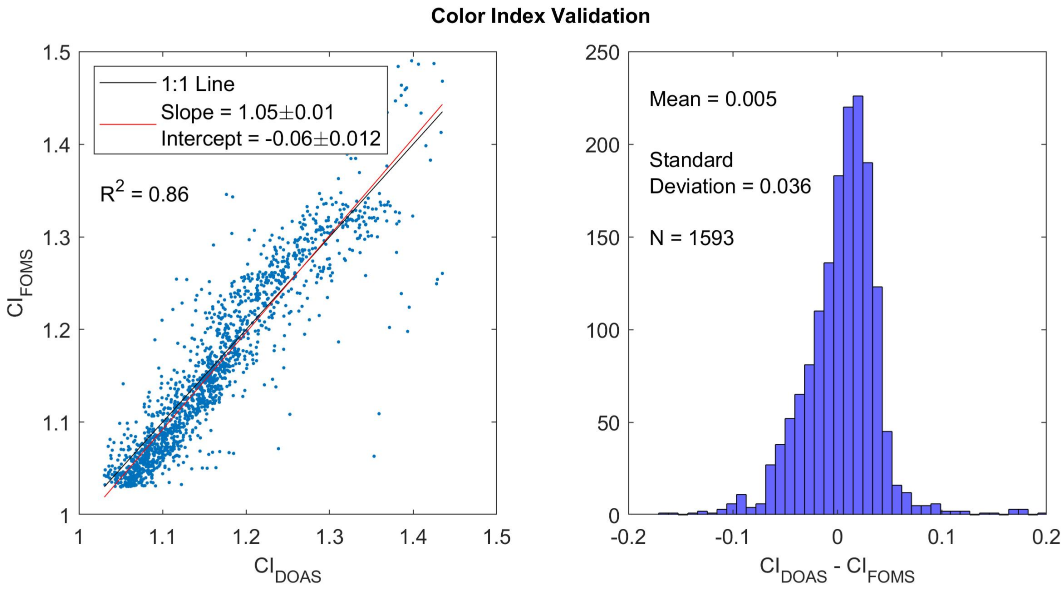

Figure 5.1: Validation of the RTM initialization using the measured and modelled CI. There was a high correlation between measured (left x-axis) and modelled (left y-axis) CIs with a small bias and standard deviation (right).

To validate the RTM initialization and usage, the CI was modelled for each mini-DOAS observations from 20 different plume overpasses of Western wildfires and the Blackwater River fire (with the methods described in Section 2.3.3). These modelled CIs were then compared to those observed by the mini-DOAS. For this comparison, one overpass was excluded due to the abnormally high solar zenith angles (>80°) of the observations. The CIs were further filtered for observations greater than 1.03 (75% of the data) to ensure that there was some smoke in the observations. The resulting comparison of the almost 1600 data points is shown in Figure 5.1.

The modelled (left y-axis) and observed (left x-axis) CIs show high correlation ($R^2 = 0.86$). A OLS regression revealed a fit with a small intercept and a slope of 1.05 ± 0.01. On the right is a histogram of the difference of the CIs, showing a near-zero mean and low standard deviation. Overall, VLIDORT-QS clearly reproduces the CI when constrained by LIDAR and aerosol observations. Much of the variability of the CI is independent from the input κAE, and the RTM calculations capture that well. This provides confidence that VLIDORT-QS can be used to study RS observations of BB smoke plumes.

5.2 Error Analysis

After validating our use of the RTM, it is important to understand how the uncertainty of the input data impacts the RTM calculations. To determine this, an error analysis was performed on the RTM initialization. Each input parameter was considered, and relevant parameters were independently adjusted plus and minus their respective uncertainty.

The uncertainty of the input LIDAR extinction profile was determined based on the variability of the LIDAR ratio from plume overpass observations. The BB aerosol size uncertainties were determined from the variability of these parameters inside various plumes. The uncertainty of the particle size distribution (PSD) was determined by fitting a log-normal shape through each smoke observation. The uncertainty listed in Table 5.1 is the mean standard deviation from each 15-minute smoke age bin of the log-normal radius and standard deviation (from Equation 2.2). It should be noted that the PSD parameters are input for the Mie code, which considers a normalized PSD. Therefore, changes in the PSD parameters are only considered for how they impact the optical properties of the aerosols and not how they change the total surface area or volume of the aerosols. The "amount" of aerosols used in a model run is controlled by the input aerosol extinction profile which is independent of the Mie code calculation.

The uncertainty used for the the real refractive index (RI) comes from observations of BB smoke (Magi et al., 2007), although the uncertainty is doubled due to the unknown composition of the BB aerosols in this work and the fact that this uncertainty is from a different study than the RIs used here. The uncertainty of the background aerosol stems from the measurement uncertainty, and is doubled to allow for changes as a function of measurement time. Lastly, the albedo uncertainty is the high-end of the uncertainty cited in Kleipool et al. (2008).

Parameter	Parameter Uncertainty	Model Uncertainty Constant κAE	Model Uncertainty Constant CI
LIDAR Profile	5%	8.8%	7.5%
PSD (r and σ)	4.2% and 1.6%	14.6%	11.9%
Real RI	2.5%	9.5%	8.0%
Background Aerosol	20%	1.8%	2.6%
Surface Albedo	15%	1.5%	1.5%
Total		19.7%	16.5%

Table 5.1: Error analysis of RTM input data.

The model uncertainty was calculated based on the mean BAMF change over the altitudes of the BB smoke plume used for the model. The results from each parameter can be seen in Table 5.1, Column 3. This analysis was then rerun by adjusting the κAE after each parameter was adjusted so that the CI remained constant (Column 4).

This latter method more closely resembles the method described in Section 2.3.3, thus Column 4 is a better representation of the total model uncertainty. By ensuring that the model reproduces the observed CI, the model uncertainty is decreased. For instance, if the LIDAR extinction profile is lower than true state of the smoke plume, the modelled CI would be low. This results in an increased input κAE, that would ultimately increase the aerosol extinction at 353.5 nm, where the model is run, and balance some of the initial uncertainty. This indicates that the CI is very useful for constraining and minimizing the uncertainty of RTM calculations.

Knowing the uncertainty of the RTM is essential to determining the uncertainty of VCD calculations, and an uncertainty of 16.5% for the RTM is used in this work based on this analysis. Further, Table 5.1 shows the largest sources of uncertainty for RT modelling. The modelled BAMFs are particularly sensitive to the influence that the natural variability of smoke has on the LIDAR data and the PSD, as the combination of these two account for a majority of the uncertainty. However, these uncertainties are somewhat mitigated when the CI is held constant. This reduced the total uncertainty by roughly 3% and could be used in future studies to reduce model uncertainty. Regardless, future modelling of BB plumes must accurately account for aerosol extinction and optical properties.

5.3 Vertical Column Densities and Mixing Ratios

VCDs were calculated for each mini-DOAS observation from the 21 overpasses analyzed with VLIDORT-QS. The results of the VCD retrieval method are shown for HCHO for the second Shady fire overpass from July 25th, 2019 in Figure 5.2.

The top plot shows the 532 nm BB AOD from the LIDAR instrument as a marker for plume thickness. The bottom plot shows the observed DSCD along with the retrieved VCD, where the VCD uncertainty stems from the 16.5% RTM uncertainty and measurement uncertainty. Early in the plume, the VCD is larger than the DSCD. The DSCD is not sensitive to the entire plume and therefore does not capture the peak HCHO amount shortly after emission, observed with the VCD. This difference decreases with plume age until the VCD is smaller than the DSCD several hours downwind. This faster VCD

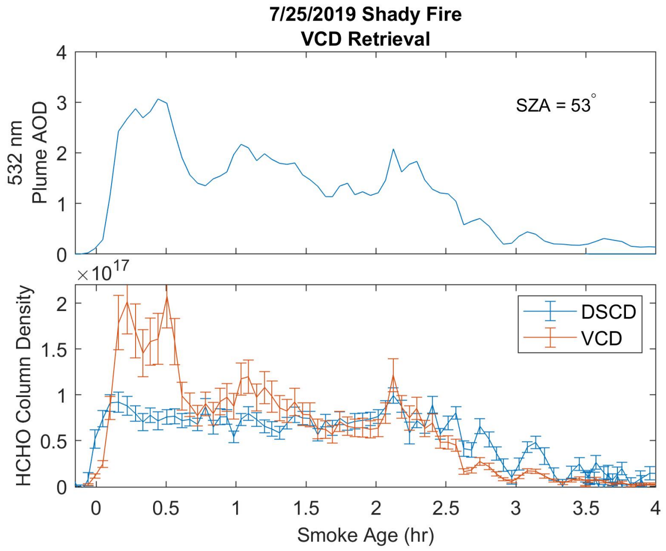

Figure 5.2: Results of a VCD retrieval for an overflight of the Shady fire on July 25th, 2019. The top plot shows the plume AOD, which decreases downwind due to plume dispersion. The retrieved HCHO VCD (in molecules per cm^2) closely follows this pattern.

decrease compared to DSCD is a common feature of plume overpass observations and shows the strong impact of dilution on the radiative transfer.

This pattern was also observed in the VCD calculation of the Williams Flats fire (Figure 5.3 left) and the Castle fire (right, from the overpass shown in Figure 4.1). For both fires, the retrieved VCDs were higher than the DSCDs in young smoke and the VCDs decreased more quickly downwind. In both of these cases, the VCD enhancement in young smoke was less than observed in the Shady fire. This is due, in part, to higher measurement sensitivity to these two plumes due to a lower SZA for the Williams Flats fire (39° compared to 53° for Shady) and a lower plume AOD for the Castle fire.

The difference between the HCHO DSCD and VCD stems from measurement sensitivity. As the plume dilutes and the AOD decreases, the mini-DOAS has higher measurement sensitivity to the plume, indicated by higher BAMFs. At the same time, the concentration of HCHO decreased in the plume due to this dilution. This can be inferred

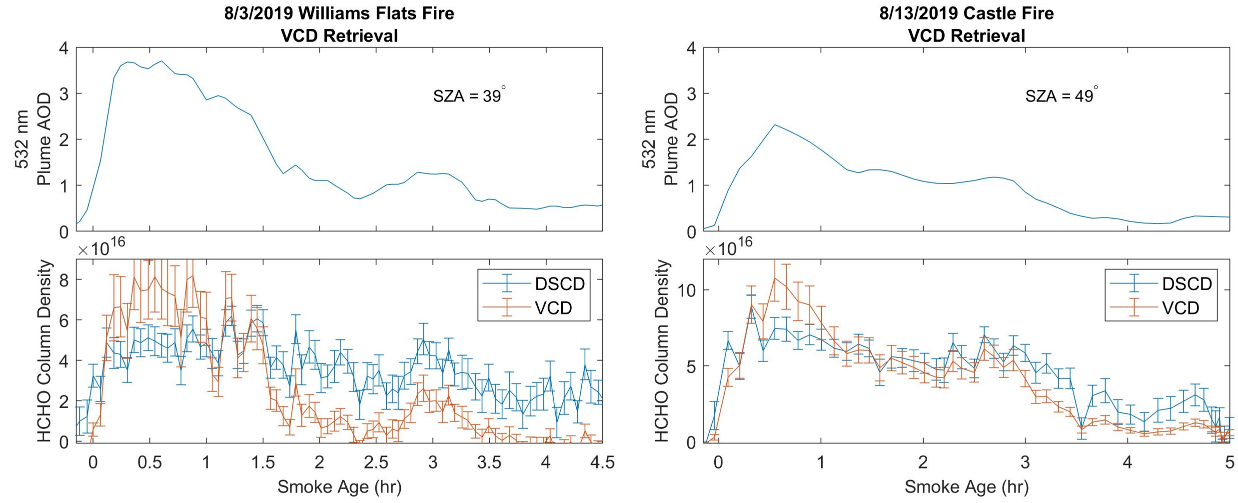

Figure 5.3: VCD retrievals for the Williams Flats fire on 8/3/2019 and the Castle fire on 8/13/2019 show a common relationship between VCD and DSCD, as seen in the Shady fire.

from the AOD, and is confirmed with the VCD. The combination of increasing sensitivity and decreasing concentration leads to a slowly decreasing DSCD. Figure 5.4 describes this process for three overpasses of the Shady fire with different SZAs.

The aerosol extinction profile provides information on the strength of the plume, and the BAMF explains the measurement sensitivity at different levels of the atmosphere, the product of these two is a proxy for the mini-DOAS sensitivity to different altitudes of the plume. Further, summing this product describes the total measurement sensitivity to the plume (middle panel of Figure 5.4). This parameter provides information on the impact that the plume VCD has on the measured DSCD. For these three overpasses, there is decreasing plume sensitivity with increasing SZA due to less light penetrating the plume at low sun angles. This example shows that the RT modelling accounts for this changing sensitivity very well, as the retrieved VCDs are very similar between 30 minutes and 1.5 hours downwind, with variability likely explained by changing emissions, changing chemistry, and transport time.

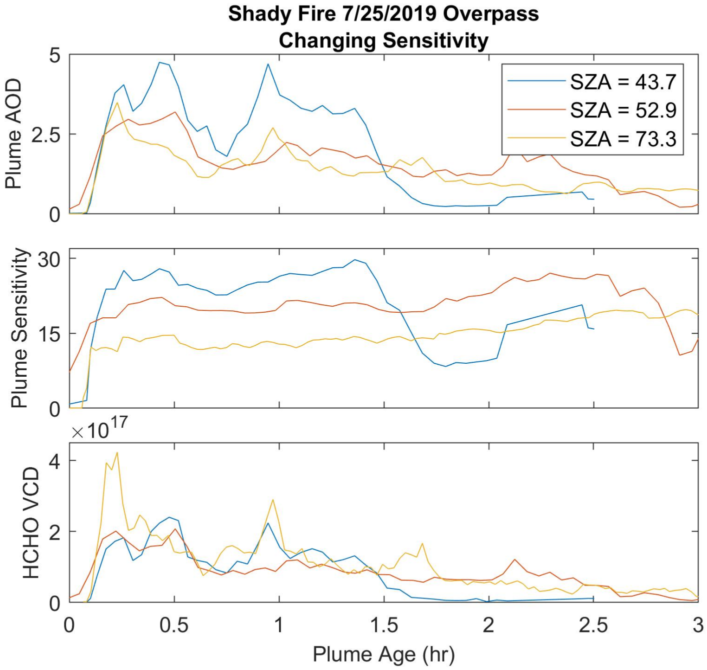

Figure 5.4: Three overpasses of the Shady fire from 7/25/2019 had different sensitivity to the plume (middle) due to the solar geometry.

For each individual overpass, the RT and plume sensitivity is dominated by the BB aerosol extinction profile. For thick smoke, the measurement sensitivity to the plume is low so a higher VCD is needed to account for the observed DSCD, and vice versa as the smoke disperses downwind. As a result, the retrieved VCDs are highly correlated with the plume AOD (Figure 5.5), although the magnitude of the VCDs is determined by the DSCDs, illustrated by the different slopes from these three overpasses.

These findings have significant impacts for satellite observations of BB plumes. Recent studies have utilized TROPOMI observations to quantify BB emissions (Jin et al., 2021; Griffin et al., 2021). These studies have taken some RT impacts into account, but this case shows that the aerosol amount greatly impacts RT and the resulting VCD analysis. Therefore, specific conditions need to be considered for each observation. Without this, the rate of retrieved VCD change will closely resemble the rate of change of the DSCD,

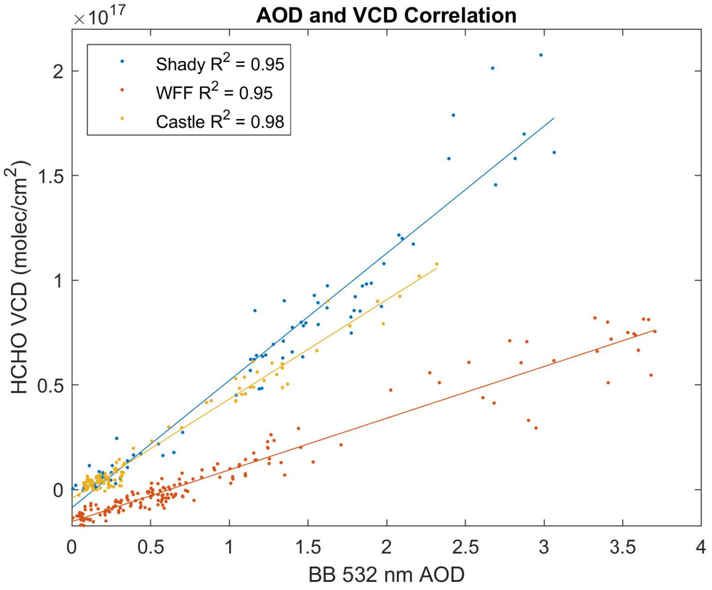

Figure 5.5: The VCD correlates very highly with the plume AOD from the examples shown in Figures 5.2 and 5.3.

which leads to an underestimate of the VCD of young smoke and overestimate of the VCD of older smoke.

The same retrieval used to calculate the VCD can also be used to calculate the mixing ratio profile from mini-DOAS data (Equation 3.10). Contour plots of the retrieved mixing ratio profiles are shown in Figure 5.6 for the same overpass as shown in Figure 5.2. They show the expected higher mixing ratios in the center of the plume and a decrease to the top and bottom of the plume, especially in the earliest part of the plume. The retrievals reflect the faster decrease of HONO and NO2 mixing ratios as the plume ages. In addition, Figure 5.6 illustrates the high variability and inhomogeneity of trace gases inside BB plumes.

Figure 5.7 shows these contour plots for the Williams Flats fire (from Figure 5.3, left). This figure similarly shows the inhomogeneity of BB plumes with significant vertical variability in the smoke location. The Williams Flats fire also has lower concentrations of all

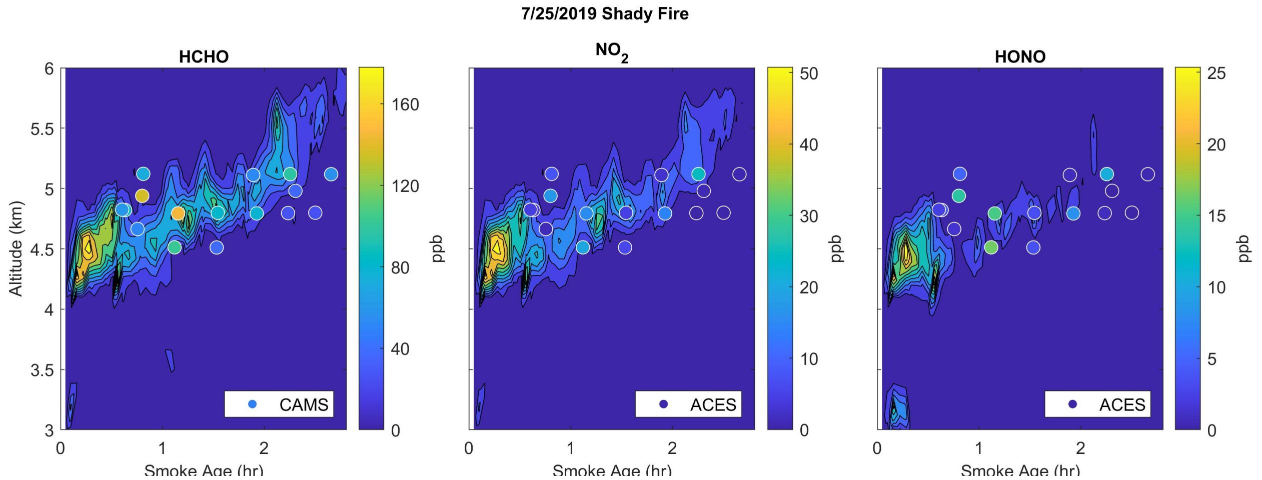

Figure 5.6: 2-D mixing ratio profiles of HCHO, NO_2, and HONO mixing ratio as determined from mini-DOAS data during a plume overpass. Overlaid is the peak mixing ratio from in-situ instruments from each in-plume transect measured within 1.5 hours of the plume overpass. We see that the magnitude of the mixing ratio is very similar between the two observations.

three trace gases, with faster downwind decreases in the concentrations. Both of these plots also show in-situ observations from within 1.5 hours of the plume overpass. The in-situ observations of HONO in the Williams Flats fire signify the difficulty of measuring HONO in-situ in BB plumes, as only one observation was made before HONO photolysis and plume dispersion led to negligible concentrations.

The results shown so far in this chapter all convey that a well-constrained RTM accurately accounts for the optical properties of BB smoke. The RTM reproduces the CI as measured by the mini-DOAS, and the model uncertainty is low for such a variable environment. The RTM also reproduced similar VCDs from three different overpasses with varying sensitivity of the plume, displaying how well the RTM represents the mini-DOAS measurements. When coupled with an accurate representation of the plume shape, this results in a detailed view of the vertical distribution of trace gases in a smoke plume. These results, combined with in-situ observations, show the variability of BB plumes

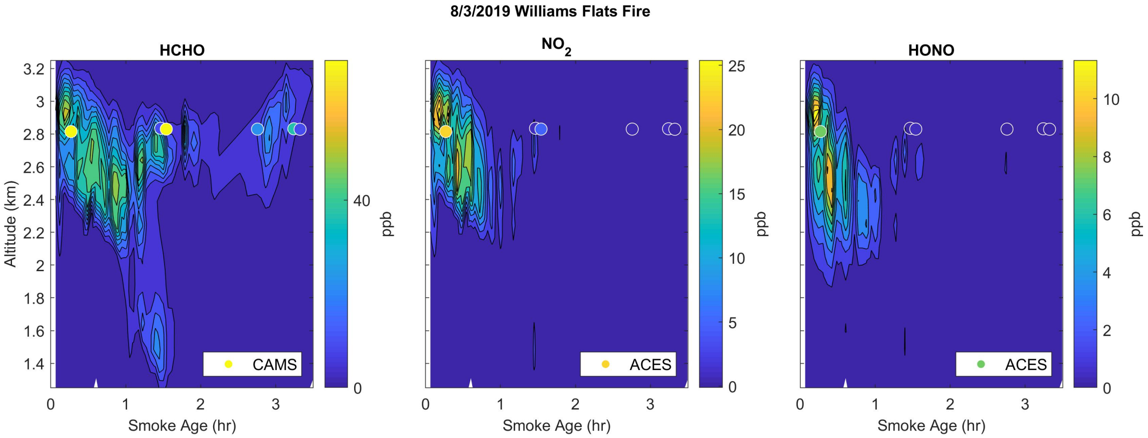

Figure 5.7: The mixing ratio profile of the Williams Flats fire displays the difficulty of measuring HONO in-situ.

which makes comparison with in-situ observations difficult. However, the magnitude of observations from these two techniques is similar, even if they are not well matched in space or time, and this offers an opportunity to compare the RS and in-situ observations.

5.4 Mixing Ratio Validation

To validate the RS retrieval method, HCHO mixing ratios from the mini-DOAS were compared to in-situ data from the CAMS instrument (Section 2.2.4) measured during the in-plume transects before and after the respective overpass. Direct comparison of in-situ to remotely sensed data is always challenging due to the different observational approaches and the fact that the two methods typically probe different air mass volumes. This problem is further exacerbated in BB plumes that are inherently variable and inhomogeneous, particularly in this case when the measurements were made at different times.

This can be seen in Figures 5.6 and 5.7, where the in-situ mixing ratios from in-plume transect data within an hour and a half of mini-DOAS observations are plotted over the mini-DOAS retrieved mixing ratio profile. Some in-situ observations appear to have been made outside of the plume. Clearly, the dynamic nature of this plume makes matching observations in space or time difficult. However, the magnitude of the observations is similar, giving confidence that this mixing ratio retrieval works.

Consequently, the measurements need to be matched based on location or plume age, neither of which will yield a perfect comparison in space and time. Considering these caveats, it is important to first define the remote sensing parameters that will most likely inform a meaningful comparison. The mini-DOAS analysis retrieved a mixing ratio profile, from which the mean mixing ratio, the maximum mixing ratio, or the mixing ratio at a specific altitudes can be determined.

The highly dynamic nature of the plume, seen in the mixing ratio profile in Figure 5.6, affects the plume shape and make values at specific altitudes difficult to rely on. Similarly, plume averages (vertical for the remote sensing data vs. horizontal for the transects) are difficult to use as horizontal and vertical dispersion are different in BB plumes

Therefore, the maximum mixing ratio retrieved by the mini-DOAS was compared with the maximum in-situ HCHO mixing ratio from each in plume transect, using the assumption that the maximum mixing ratio from a horizontal transect should be similar to the maximum of a vertical transect. The two datasets were then matched as a function of plume age, assuming that emissions and dilution did not change in the time between the two observations. The in-situ mixing ratios plotted in Figure 5.6 represent the maximum mixing ratio observed by CAMS for each transect flown within 1.5 hours of the plume overpass over the mixing ratio profile retrieved by the mini-DOAS (Figure 5.6).

To provide a more statistical view, this comparison was applied to all FIREX-AQ wildfires, with some additional restrictions to further address the temporal and spatial differences between the observations. As the smoke age is not fully known, mini-DOAS mixing ratios within a 15-minute smoke age of the in-situ observations were averaged to reduce this uncertainty. To further account for plume dynamics, the comparison was restricted to data where the peak AOP aerosol extinction was at least 0.5 km^{-1} and the difference between the peak LIDAR and AOP extinction was less than 1 km^{-1}. This was done to ensure that thick smoke was measured during the in-plume transect and that similar plume magnitudes were measured by both instruments.

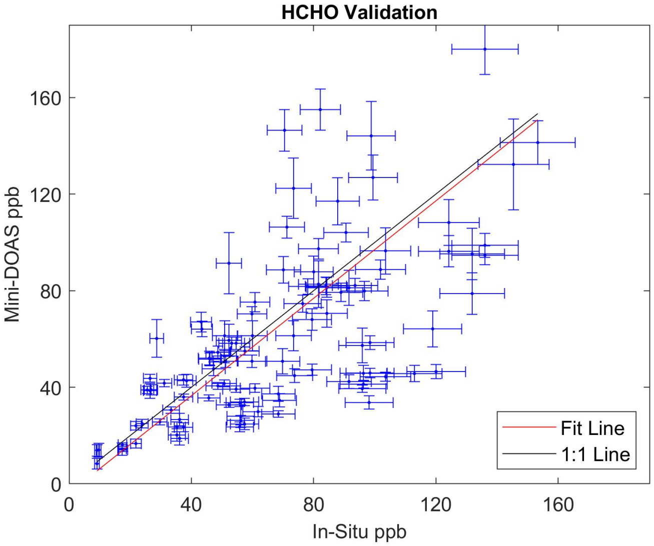

Figure 5.8: Correlation plot of in-situ mixing ratios from CAMS (x-axis) and the mini–DOAS retrieved HCHO mixing ratios (y-axis). The fit line is from an error-weighted orthogonal distance regression where with a slope of 1.01 and intercept of -3.85 ppb. The mini-DOAS has a bias of -6 ppb and the two datasets have a mean deviation of 21 ppb (30%).

The resulting comparison (Figure 5.8) shows excellent overall agreement of the data, with only a small bias between the two instruments and a near 1:1 fit line. Using a BEWR on 108 data points resulted in a slope of 1.01 ± 0.02 and an intercept of -3.85 ± 0.95 ppb with an R^2 of 0.45. Much of the variability around the fit line (standard deviation of 27.5 ppb) is due the challenge of matching the data in space and time in the highly inhomogeneous plumes.

5.5 Vertical Sensitivity

The relationship between the DSCD and VCD seen in Figures 5.2 and 5.3 is partially due to the changing sensitivity with altitude of the mini-DOAS with thinning smoke. This can be explained with Figure 5.9, by studying the BAMFs calculated at three different plume locations. For young, thick smoke (right), the BAMF quickly decreases from above the plume, reaching zero as light no longer penetrates the plume. As smoke disperses downwind, the BAMF increases as more light can penetrate the smoke. As the BAMF explains the instrument sensitivity to different levels of the atmosphere and the LIDAR extinction profile explains the magnitude of the smoke, the product of these two acts as a proxy for instrument sensitivity to the plume. The thinning of the plume and increasing BAMF counteract each other, resulting in a similar plume sensitivity at all three locations. As a result, the DSCD changes slowly as a function of plume age (Figures 5.2 and 5.3).

For early observations of the plume, there were portions of the plume that the mini-DOAS was not sensitive to that are used for the VCD calculation. This may seem like an extrapolation. However, these areas of the plume are not considered in the mixing ratio retrieval described in Section 3.4. Further, particularly in young smoke before significant photochemistry occurs, the aerosol profile is a very good representation of the HCHO profile in the smoke. It is therefore appropriate to include these portions of smoke in the VCD calculations. Cases where this profile shape is not known will be considered later.

The changing sensitivity with altitude is important to note, as it has implications for RS interpretation. The HCHO DSCDs show a slow decrease with plume age. If the RT impacts between individual observations are not considered, then this would indicate little change in HCHO throughout these observations. However, this clearly is not the

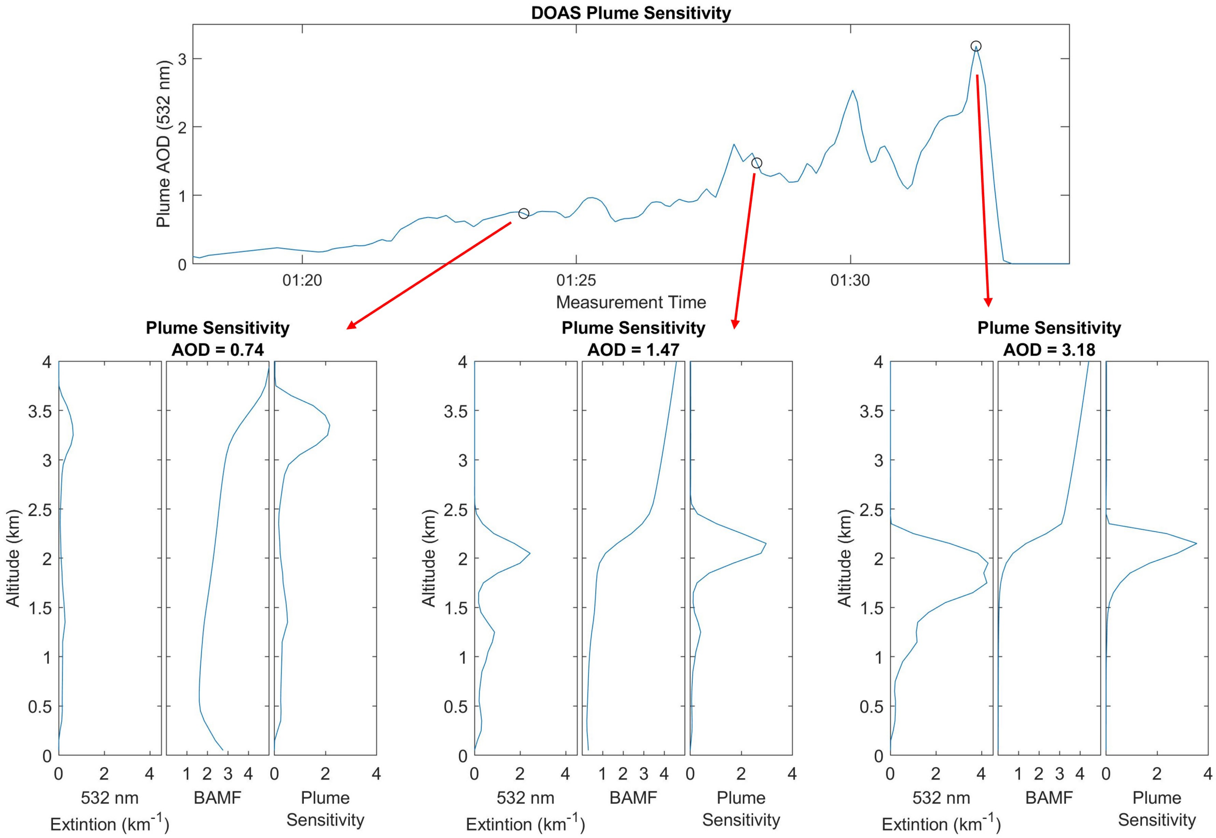

Figure 5.9: The 532 nm plume AOD from LIDAR data during the third plume overpass of the Shady fire on July 25th shows the relative concentration of the plume (top). Shown below is the input aerosol profile, modelled BAMF, and plume sensitivity for three different plume optical depths.

case due to plume dispersion (indicated by the AOD in Figure 5.9). Any quantification of downwind chemistry or emissions as a function of time without considering this changing sensitivity would thus be flawed.

5.6 Photochemical Profiles

Up to this point, the results have been focused on HCHO, which undergoes slow photolysis and formation. As observations of HONO in BB plumes are a large benefit of passive remote sensing, it is important to consider the effect of HONO photolysis. When considering the plume shape in the VCD calculation (Section 3.4), the LIDAR aerosol profile accounts for plume dispersion, but not chemistry.

HONO photolysis rates vary vertically in a plume due to changing light intensity at different altitudes. This causes HONO concentrations to decrease at the top of the plume where smoke is illuminated, and remain relatively unchanged in the middle of the plume where photolysis rates are considerably smaller in thick smoke. This results in a plume shape that differs from that of the aerosol extinction.

To study the impact of HONO photochemistry on mini-DOAS observations and retrievals, the PACT-1D chemical model was used (Section 3.2). The specifics of this model are beyond the scope of this thesis, and the results from the model will not be directly analyzed. The HONO profiles from the model were used to account for photolysis in the VCD retrieval. Photolysis profiles were parameterized based on VLIDORT-QS observations (Section 3.3) and in-plume photolysis rates. So far, results are only available for two overpasses.

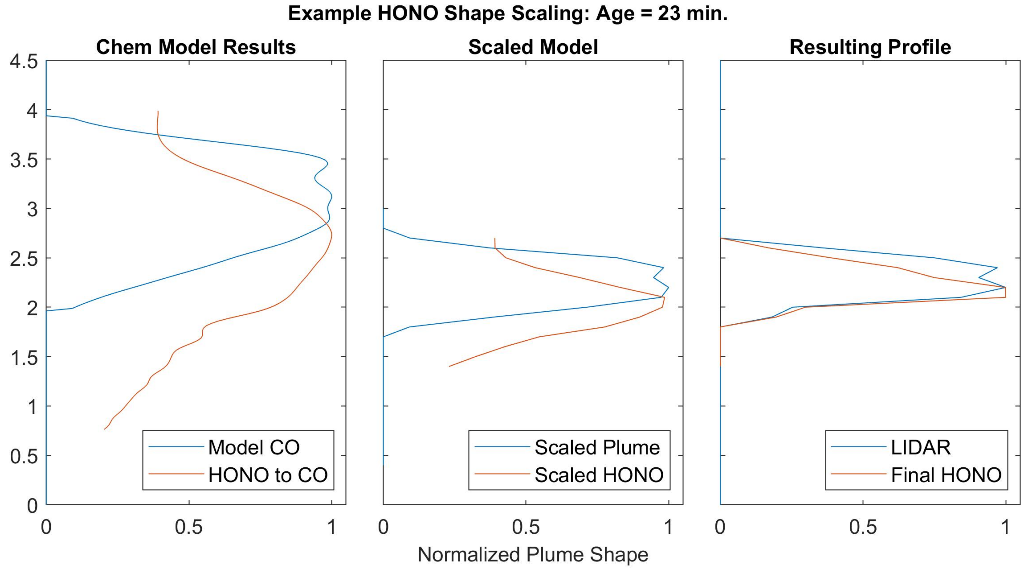

Figure 5.10: Example PACT-1D HONO profile scaling.

The use of PACT-1D results is summarized in Figure 5.10, which shows the model profiles (left) for a smoke age of 23 minutes. The modelled plume shape (using CO as the plume shape proxy) was scaled to the observed LIDAR profile based on plume height and width as a function of plume age (middle). This scaling was then applied to a normalized profile of the plume HONO to CO ratio, which quantifies how the profile of HONO differs from the CO/aerosol profile. This normalized ratio is then multiplied by the observed LIDAR plume shape resulting in the HONO plume shape (right).

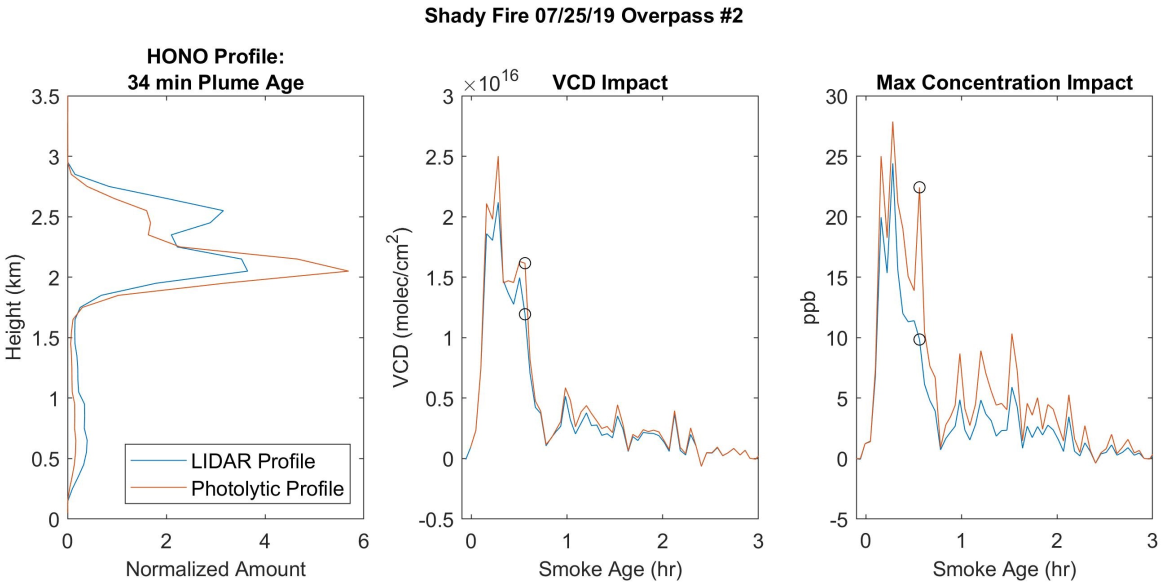

Figure 5.11: The effect of HONO photolysis on VCD retrievals during the second overpass of the Shady fire. The circled points denote the observation shown in the left panel.

The impact that plume photolysis has on VCD calculations can be seen in Figure 5.11, where the VCD and mixing ratio were calculated with this updated plume shape and observed HONO DSCDs (Section 3.4). On the left is an example of the effect of HONO photolysis on the input plume shape 34 minutes after emission. Utilizing the updated, photochemical profile (orange) has a 15% impact on the retrieved VCD over the first 2 hours after emission. The impact on the retrieved HONO mixing ratio in the plume (right) is even larger ($\sim$60%).

Clearly, photolysis has a large impact on the illuminated portions of the plume, *i.e.* the top and bottom of the plume where there is downwelling and upwelling radiation, respectively. This ostensibly narrows the HONO profile, skewing HONO to the middle of the plume where the mini-DOAS has lower sensitivity. Again, these two profiles are normalized to have a mean of one, and the VCD calculation depends on the profile shape, not the magnitude of the profile.

The middle panel of Figure 5.11 shows the VCD calculated with the LIDAR profile and with the chemical model profile, and the right panel shows the maximum mixing ratio retrieved from these two profiles. HONO photolysis affects the VCD and mixing ratio starting at just 10 minutes of plume age until nearly 2.5 hours after emission. This is partly due to the altitude dependent sensitivity of mini-DOAS observations. For observations of thick, young smoke, the mini-DOAS has much higher sensitivity to the upper portion of the plume with decreasing sensitivity further into the plume. By skewing the HONO profile lower in the plume where there is lower instrument sensitivity, more HONO is needed to produce the same DSCD. As such, accounting for HONO photolysis leads to an increased VCD for the first several hours after emission. This impact is slightly counteracted by the decreased HONO on the bottom of the plume. As a result, there is a larger impact on the peak HONO mixing ratio than on the HONO VCD. Eventually, in this case at 2.5 hour plume age, the plume has thinned enough that HONO photolysis affects every level of the plume and the sensitivity of the mini-DOAS has much less altitude dependence.

Figure 5.12 shows the impact of HONO photolysis on retrieved VCDs for the Williams Flats fire, the second fire that has been modelled with PACT-1D. Similar to the Shady

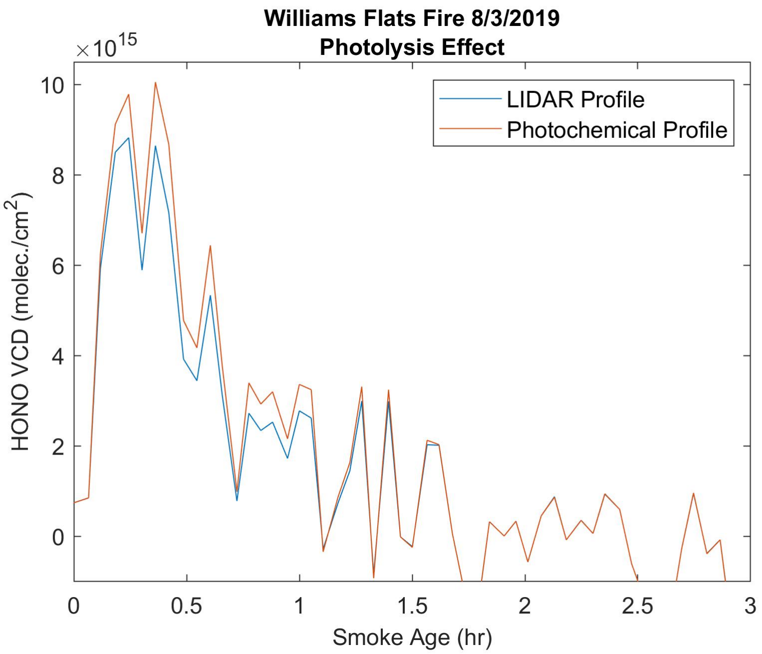

Figure 5.12: The impact of HONO photolysis on the Williams Flats fire from 8/3/2019.

fire, the average impact from HONO photolysis over the first 2 hours was 13%, with the largest impact occurring at roughly 45 minutes downwind. These two fires had similar dynamics, with a majority of the fuel being timber, smoke lofting above the boundary layer, maximum plume AODs between 3 and 4, and similar plume widths. Therefore, the fact that the impact of photolysis is similar for both cases is not surprising. Yet these conditions match several other fires observed during FIREX-AQ and suggest that these findings are a good representation of Western wildfires. A 13-15% difference of HONO in BB plumes would greatly impact the subsequent photochemistry. Therefore, future RS observations and modelling of BB plumes must consider the impacts of HONO photolysis on the profile shape. This also motivates advancement in the modelling of photolysis rates in BB plumes to better understand these observations and the impacts on BB chemistry.

5.7 Application to Satellites

This thesis has focused on how well remote sensing can measure trace gases in BB smoke plumes if good measurements are available to constrain a RTM. However, it is important to consider cases where this data is not available. For instance, satellite observations of smoke plumes will have much less data on the optical properties and vertical distribution of BB smoke available.

To determine the capability of satellites to measure trace gases in smoke plumes, apriori parameters were calculated based on FIREX-AQ averages. The average parameters were: smoke plume width, smoke PSD, background aerosol PSD, κAE, BC content, and background profiles of pressure, temperature, trace gas concentrations, and aerosol extinction. All of the values were calculated from campaign averages, listed in Table 5.2.

PARAMETER	VALUE
Plume Width	σ = 0.44, FWHM $\sim$ 1 km
κAE	7
BC Content	13%
Smoke PSD - Mode #1	r_0 = 0.115 μm, σ = 0.7, amount = 84%
Smoke PSD - Mode #2	r_0 = 0.06 μm, σ = 0.78, amount = 16%
Boundary Layer PSD	r_0 = 0.08 μm, σ = 0.59
Free Troposphere PSD	r_0 = 0.07 μm, σ = 0.54

Table 5.2: Apriori data calculated from FIREX-AQ observations for a VLIDORT-QS sensitivity test. PSD variables are those from Equation 2.2

Background profiles of pressure, temperature, trace gas concentration, and aerosol extinction were averaged over the campaign. The plume width was the median standard deviation from Gaussian fits of overpass LIDAR data. The κAE and BC content are the mean derived from RT modelling. The smoke PSD was fit from all Western wildfire observations of smoke less than 4 hours old (using Equation 2.2) and weighted by number concentration. The background PSDs were averaged from each flight.

For each observation, the solar geometry, surface elevation, and surface albedo were updated, as they are easy to account for in satellite data. The altitude of the top of the plume was also updated using LIDAR data, as this was an important parameter and can be approximated with O_4 observations or the TROPOMI aerosol layer height (Griffin et al., 2020). Lastly, the CI was used to iteratively determine the plume AOD for each observation.

AOD algorithms currently exist for many satellites, *e.g.* TropOMAER for TROPOMI (Torres et al., 2020), and the TROPOMI algorithm utilizes 354 and 388 nm observations, similar to the use of the CI. Figure 5.13 shows the impact of using the CI-based AOD calculation along with the original method (Section 3.4), as well as the effect of using a constant AOD of 1.5 based on the campaign average. The impact that the plume AOD has on the overall RT of a smoke plume indicates that the AOD must be updated for each observation and not held at a constant, average value from the campaign, to ensure that the changing instrument sensitivity is captured (Figure 5.9).

This analysis further demonstrates the importance of accounting for the amount and optical properties of aerosols in RS observations of BB plumes. When constant RT is assumed, the resulting VCD retrieval leads to an underestimation for young smoke (by 37% in the first 30 minutes) and overestimation downwind. Utilizing the CI to update the amount of aerosols in an observation greatly improves this, seen by an increased VCD in young smoke (toward the right) and decreased VCD in aged smoke. The CI-based analysis still underestimates the VCD for young smoke, by 13.5% in the first 30 minutes. This is because the smoke was so thick, that changes in the AOD had little impact on the CI. However, the CI used in this thesis utilizes observations at 340 and 360 nm. Extending

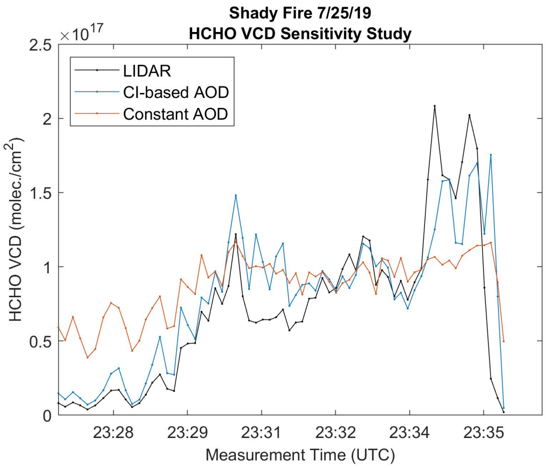

Figure 5.13: Results of a sensitivity study to determine the impact of averaged model input parameters. In black is the "true" HCHO VCD (from Figure 5.2). In blue is the retrieved VCD when the modelled CI is used to constrain the plume AOD. In orange is the retrieved VCD using a constant plume AOD of 1.5 (at 532 nm)

the CI calculation to more, and higher, wavelengths could provide more information on the AOD of smoke plumes and potentially more information on the optical properties of the smoke aerosols. Further use of the CI to constrain satellite-based RTM calculations should be explored.

CHAPTER 6

Discussion of Findings and Outlook

6.1 Plume Emissions and Chemistry

One goal of this research was to study and quantify HONO emissions from Western wildfires via remote sensing. The emissions observed by the mini-DOAS agreed very well with observations from Akagi et al. (2011) for temperate forest. Unfortunately, there were too few observations of grassland/shrubland fires during the FIREX-AQ campaign to make any meaningful determinations about emissions from this fuel type.

Due to the large variability of HONO emission, the findings from Andreae (2019) also fall within the margin of uncertainty of the temperate forest emissions seen by the mini-DOAS. The fact that both emission inventories agree within a standard deviation of the emissions calculated here is further evidence of the large variability of HONO emissions. For this reason, either emission inventory could theoretically be used to model BB plume smoke chemistry. However, if attempting to recreate the chemistry of specific observations, a more accurate representation of HONO emission is likely needed.

Since the work of Trentmann et al. (2005), heterogeneous production of HONO has been a key area of interest. For instance, Alvarado and Prinn (2009) relied on the secondary HONO production scheme proposed in Trentmann et al. (2005) to recreate downwind ozone production in chemical modelling of the same fire plume. However, the modelling of the Timbavati fire smoke plume in both Trentmann et al. (2005) and Alvarado and Prinn (2009) utilized a HONO emission of 0.122% HONO to CO.

This was lower than all emissions calculated from mini-DOAS data and all but two emissions calculated with in-situ data. Further, these two lower emissions calculated from in-situ data were from timber burning, which generally has a lower MCE and therefore has a lower HONO to CO emission ratio than the savanna biome of the Timbavati fire. Although this emission ratio is derived from in-situ data, the AFTIR instrument used had high HONO measurement uncertainty. Further, Alvarado et al. (2015) found no evidence of secondary chemistry in chemical modelling of a different plume.

This is not to say that there is no heterogeneous production of HONO in BB plumes or that it is insignificant. The emissions of HONO seen in this work and how they compare to literature simply indicate that the variability of HONO emissions likely has a larger effect on the concentration of HONO in young BB plumes than secondary chemistry.

Another conclusion from the comparison of mini-DOAS emissions to those from literature may be that photolysis has little impact on in-situ emission measurements, considering the excellent agreement between mini-DOAS and Akagi et al. (2011). However, in-situ observations from the FIREX-AQ campaign suggest otherwise. Emissions measured by the mini-DOAS were generally higher than those seen in-situ, even in photochemically young smoke, suggesting that photolysis needs to be considered for in-situ HONO emission calculations. Remote sensing observations help in reducing the effect of photolysis and observations closer to the fire should be further explored. One alternative may be to calculate HONO emissions as a HONO to NO_2 ratio, which is the method utilized in Akagi et al. (2011). For FIREX-AQ, similar HONO to NO_2 emission ratios were observed via RS and in-situ, suggesting that this parameter has less impact from photolysis over the first 30 minutes after emission.

Fuel Type	Theys et al. (2020)	Mini-DOAS
Grassland, etc.	0.34 ± 0.08	0.31
Extratropical Forest	0.54 ± 0.12	0.56 ± 0.19

Table 6.1: ER_{HONO/NO_2} comparison from TROPOMI and mini-DOAS data.

Theys et al. (2020) utilized TROPOMI observations of biomass burning to quantify HONO to NO_2 emission ratios and found higher HONO to NO_2 ratios than laboratory and field studies for all three fuel types considered. Interestingly, and as previously noted, this relationship was not seen here. However, the emissions seen for both extratropical forest and savanna/grassland/shrubland both agree very well with the emissions observed by the mini-DOAS (Table 6.1). This is very encouraging, as it suggests that the pixel size of TROPOMI (3.5 x 7 km^2) does not impact the observed HONO to NO_2 emission ratio and that satellite data will be invaluable to calculate and study HONO emissions. Further, it signifies that a simple correction accurately accounts for the stratospheric component of the NO_2 SCD.

As geostationary satellites become more prevalent (*e.g.* TEMPO), RS observations of smoke plumes could also provide observations of changing fire dynamics which may be helpful to understanding the variability of HONO emissions. Figure 6.1 shows seven different mini-DOAS emission calculations from three different days of the Williams Flats fire. This was the only fire with more than three emission calculations from the mini-DOAS. For this fire, there was a high relationship between the HONO to NO_2 emission ratio and the MCE, as calculated in-situ for the in-plume observations temporally closest to the overpass.

Although the fuel burned changed over the course of these three observation days,

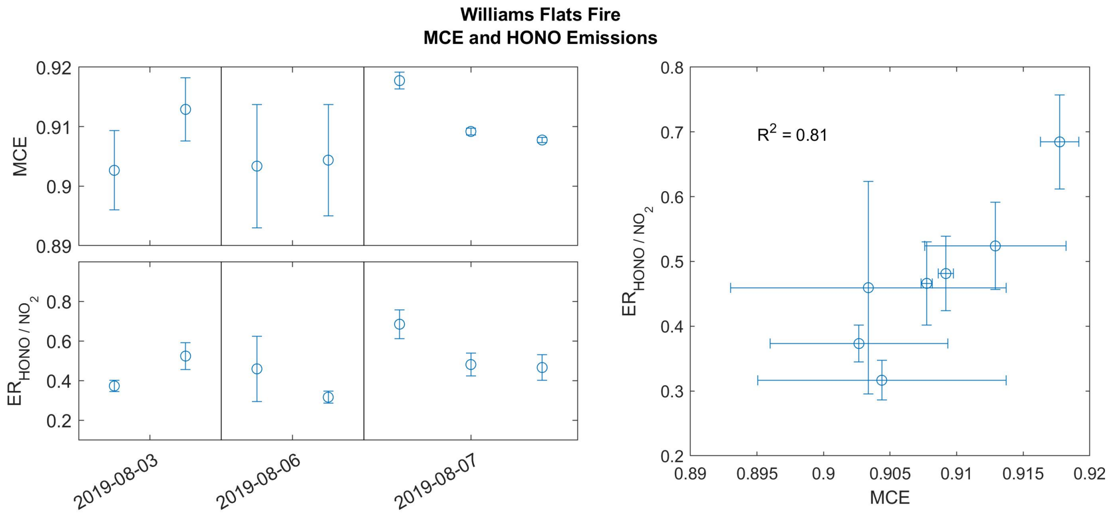

Figure 6.1: ER_{HONO/NO_2} calculated over three days of observations of the Williams Flats fire and the MCE determined from in-situ data (left).

many other fire parameters were similar. For instance, soil moisture, fuel moisture content, relative humidity, etc. were more similar than if considering multiple other fires. It is difficult to make a significant claim from this finding based on seven observations, but it offers one explanation to the variability of HONO emissions. Future satellite observations will be helpful to study these dynamics and determine if this relationship is robust or merely coincidence.

Although the ability of satellites to observe HONO to NO_2 emission ratios is exciting, it is important to consider the utility of this parameter. HONO to NO_2 ratios are dependent upon NO_2 emissions and chemistry, which can be complicated in BB plumes. NO is quickly converted to NO_2 after emission, but this process can be limited by the amount of ozone in the background atmosphere. As a result, early NO_2 amounts, and therefore HONO to NO_2 ratios, are impacted by NOx emissions and ozone availability. It is important to consider this chemistry when utilizing HONO to NO_2 ratios.

Due to the impacts of chemistry on HONO to NO_2 ratios, it is worthwhile to study the ability of satellites to measure emission factors. In this thesis, I utilized in-situ observations of HCHO to quantify emissions, which is not feasible for satellite data. One alternative to this approach is to utilize emission inventories for HCHO to scale the HONO to HCHO ratio in the same method that this thesis utilized.

For instance, using HCHO emissions for temperate forests of 2.04 g/kg dry fuel (Andreae, 2019) results in mini-DOAS HONO emissions of 0.53 ± 0.2 g/kg which is very close to the temperate forest emissions derived with in-situ data with a standard deviation between the two methods of 0.11 g/kg. This suggests much more consistent HCHO emissions from temperate forest BB, and that this method can certainly be used for an approximation of HONO emissions.

The last consideration to make for future satellite observations is the impact of plume photochemistry. In this work, it was clear that the HONO to NO_2 ratio was not always indicative of the chemistry of the entire plume. In many observations of thick plumes with high sun (low SZA), the mini-DOAS observations suggested lower HONO to NO_2 ratios than were seen inside the plume. However, this was not always the case (Figure 4.13 - left). Unfortunately, no consistent conclusions can be made from these comparisons. For each observation of HONO to NO_2 ratios in BB plumes, it is important to consider the plume AOD, solar geometry, age of smoke, and sensitivity of the RS instrument.

6.2 Remote Sensing and Radiative Transfer

Measurements of HONO and NOx in BB plumes from satellites are beginning to be reported (Theys et al., 2020; Jin et al., 2021; Griffin et al., 2021). However, of these early works, radiative transfer is either not considered or is greatly approximated. Theys et al.

(2020) reported tropospheric SCD ratios of HONO to NO_2 and argued that RT did not need to be considered due to trace gas colocation. However, this work showed that the profiles of HONO and NO_2 change with respect to each other. Due to plume photochemistry and the RT environment, downwind SCD ratios of HONO to NO_2 are not indicative of the entire plume. Although, this approximation appears to be accurate shortly after emission.

Both Jin et al. (2021) and Griffin et al. (2021) have attempted to quantify NOx and NO_2 emissions from BB, respectively. Jin et al. (2021) utilized an apriori NO_2 profile with the standard TROPOMI AMF which assumed that BB plumes are clouds and used a cloud fraction to scale AMFs. Griffin et al. (2021) applied an explicit aerosol correction, although utilized a similar apriori aerosol and NO_2 profile. Further, the BB pollutants were held constant between 0 and 2.5 km and linearly decreased to 0 at 3.5 km altitude. Griffin et al. (2021) considers a changing AOD based on a parameterization of initial TROPOMI NO_2 VCDs, before aerosol correction. In this case, the AODs considered varied from 0 to 1 at 550 nm. This is lower than the maximum 532 nm AOD observed in all but one plume overpass studied during FIREX-AQ.

In both works, these flawed RT considerations add uncertainty and bias to the VCD retrievals. Results from this thesis show that the methods of Griffin et al. (2021) would underestimate VCDs due to underestimating the plume AOD. By utilizing a low AOD, the RT would assume higher measurement sensitivity to the plume and therefore underestimate the plume VCD. Further, the natural variability of the smoke extinction and PSD, coupled with refractive index uncertainty, resulted in a model uncertainty of 16.5%. This uncertainty would be considerably higher if the smoke plume were approximated as a cloud fraction. Future studies must consider both the amount and optical properties of

BB smoke plumes.

In this thesis, I show the utility of unique RT calculations for each BB plume observation. With the individual RT effects accounted for, good agreement was found between mini-DOAS retrievals and in-situ observations in the plume (Figure 5.8). Although the spread was high due to the challenges of matching observations in space and time, the near 1:1 fit with low uncertainty provides confidence in the methods described here.

For this thesis, the color index was used to constrain the κAE of BB aerosols for RTM initialization. The CI was largely a function of the plume AOD, the κAE, and the PSD of the aerosols, and by modelling the CI, I ensured that the RTM calculations accurately accounted for the amount and optical properties of particles in smoke plumes. The utility of the CI can be extended to satellite data, as it provides an easy way to account for the changing RT environment in BB plumes. Without in-situ data, these impacts of aerosol optical properties are very difficult, if not impossible, to accurately account for and the CI may be the best option to minimize these uncertainties. Even with these CI-based, individual calculations, the different RT assumptions can have a 50% impact on the retrieved VCD. This impact is likely higher for lookup table BAMFs/AMFs.

Much of this remaining uncertainty stems from constant aerosol optical properties in RTM calculations and the effect of light penetration on the CI. In this work, only two wavelengths were used for CI calculations. It is certainly possible that extending the CI to different wavelengths could help constrain both of these issues. For instance, light penetrates further into the plume at higher wavelengths and may be less impacted by the effects of BrC. Therefore, larger wavelengths may be more useful for approximating plume AODs in RTM calculations. Similarly, using multiple wavelength ranges could allow more constraints on the aerosol optical properties. This should be an area of focus over the coming years as it is a simple way to account for plume dynamics.

Another consideration for RS of BB plumes is the impact of photochemistry. Photolysis appears to have a smaller impact on NO_2 in BB plumes than HONO. Evidence to support this is the rate of change of NO_2 DSCDs compared to HONO DSCDs. Although NO_2 photolysis rates are higher than those of HONO, there are many more sources of NO_2 and it quickly reaches equilibrium. As a result, the plume shape of NO_2 is likely similar to that of HCHO, but perhaps with higher variability.

Photolysis impacted HONO observations in BB plumes throughout this campaign, where mini-DOAS data often suggested decreasing HONO in the upper part of illuminated plumes. This scenario was also recreated with chemical modelling of two separate plumes. Accounting for this change in the shape of the HONO profile led to a roughly 15% average increase in the retrieved VCD from mini-DOAS data due to decreasing sensitivity with depth through a plume. This was found for two similar Western wildfires, both with peak AODs between 3 and 4 and plumes that lofted above the boundary layer. Further work is needed to study HONO chemistry in BB plumes under different circumstances, such as varying plume optical thickness, emissions, vertical spread, etc. This work will be very important to understanding satellite observations of HONO and NO_2 in BB plumes.

Also needed for future chemical modelling is a better representation of photolysis rates. This study showed that a proxy for photolysis rates can be calculated with RT modelling and used to parameterize the vertical distribution of photolysis rates. However, this is still based on a few assumptions, is only accurate in the plume, is scaled by observations at just a single altitude. Lastly, the model was also only run at a single wavelength. A RTM optimized to calculate actinic fluxes would be very beneficial for directly modelling the vertical distribution of photolysis rates. This could also be useful for future satellite observations of HONO emissions, which likely have a similar impact from photolysis as mini-DOAS emission calculations. Advances in this area would therefore be very beneficial.

BIBLIOGRAPHY

S. K. Akagi, R. J. Yokelson, C. Wiedinmyer, M. J. Alvarado, J. S. Reid, T. Karl, J. D. Crounse, and P. O. Wennberg. Emission factors for open and domestic biomass burning for use in atmospheric models. *Atmos. Chem. Phys.*, 11(9):4039–4072, 2011. ISSN 1680-7316. doi:10.5194/acp-11-4039-2011.

S. K. Akagi, J. S. Craven, J. W. Taylor, G. R. McMeeking, R. J. Yokelson, I. R. Burling, S. P. Urbanski, C. E. Wold, J. H. Seinfeld, H. Coe, M. J. Alvarado, and D. R. Weise. Evolution of trace gases and particles emitted by a chaparral fire in California. *Atmos. Chem. Phys.*, 12(3):1397–1421, 2012. doi:10.5194/acp-12-1397-2012.

Ali Akherati, Yicong He, Matthew M. Coggon, Abigail R. Koss, Anna L. Hodshire, Kanako Sekimoto, Carsten Warneke, Joost de Gouw, Lindsay Yee, John H. Seinfeld, Timothy B. Onasch, Scott C. Herndon, Walter B. Knighton, Christopher D. Cappa, Michael J. Kleeman, Christopher Y. Lim, Jesse H. Kroll, Jeffrey R. Pierce, and Shantanu H. Jathar. Oxygenated Aromatic Compounds are Important Precursors of Secondary Organic Aerosol in Biomass-Burning Emissions. *Environ. Sci. Technol.*, 54(14): 8568–8579, 2020. doi:10.1021/acs.est.0c01345.

Duncan T. L. Alexander, Peter A. Crozier, and James R. Anderson. Brown Carbon Spheres in East Asian Outflow and Their Optical Properties. *Science*, 321(5890):833–836, 2008. doi:10.1126/science.1155296.

M. J. Alvarado, C. R. Lonsdale, R. J. Yokelson, S. K. Akagi, H. Coe, J. S. Craven, E. V. Fischer, G. R. McMeeking, J. H. Seinfeld, T. Soni, J. W. Taylor, D. R. Weise, and C. E. Wold. Investigating the links between ozone and organic aerosol chemistry in a biomass burning plume from a prescribed fire in California chaparral. *Atmos. Chem. Phys.*, 2015. ISSN 1680-7324. doi:10.5194/acp-15-6667-2015.

Matthew James Alvarado and Ronald G. Prinn. Formation of ozone and growth of aerosols in young smoke plumes from biomass burning: 1. Lagrangian parcel studies. *J. Geophys. Res.*, 2009. doi:10.1029/2008JD011144.

Meinrat O. Andreae. Emission of trace gases and aerosols from biomass burning - An updated assessment. *Atmos. Chem. Phys.*, 2019. ISSN 1680-7324. doi:10.5194/acp-19-8523-2019.

Moetasim Ashfaq, Subimal Ghosh, Shih-Chieh Kao, Laura C. Bowling, Philip Mote, Danielle Touma, Sara A. Rauscher, and Noah S. Diffenbaugh. Near-term acceleration of hydroclimatic change in the western U.S. *J. Geophys. Res. Atmos.*, 118(19):10,676–10,693, 2013. doi:https://doi.org/10.1002/jgrd.50816.

S. Baidar, H. Oetjen, S. Coburn, B. Dix, I. Ortega, R. Sinreich, and R. Volkamer. The CU Airborne MAX-DOAS instrument: vertical profiling of aerosol extinction and trace gases. *Atmos. Meas. Tech.*, 6(3):719–739, 2013. doi:10.5194/amt-6-719-2013.

P. Baylon, D. A. Jaffe, S. R. Hall, K. Ullmann, M. J. Alvarado, and B. L. Lefer. Impact of Biomass Burning Plumes on Photolysis Rates and Ozone Formation at the Mount Bachelor Observatory. *J. Geophys. Res. Atmos.*, 123(4):2272–2284, 2018. doi:https://doi.org/10.1002/2017JD027341.

I. R. Burling, R. J. Yokelson, D. W. T. Griffith, T. J. Johnson, P. Veres, J. M. Roberts, C. Warneke, S. P. Urbanski, J. Reardon, D. R. Weise, W. M. Hao, and J. de Gouw. Laboratory measurements of trace gas emissions from biomass burning of fuel types from the southeastern and southwestern United States. *Atmos. Chem. Phys.*, 10(22):11115–11130, nov 2010. ISSN 1680-7324. doi:10.5194/acp-10-11115-2010.

J. G. Calvert, R. Atkinson, J. a. Kerr, Sasha Madronich, G. K. Moortgat, Timothy J. Wallington, and G. Yarwood. *The Mechanisms of Atmospheric Oxidation of the Alkenes*. Oxford Univ. Press, 2000.

R. K. Chakrabarty, H. Moosmüller, L.-W. A. Chen, K. Lewis, W. P. Arnott, C. Mazzoleni, M. K. Dubey, C. E. Wold, W. M. Hao, and S. M. Kreidenweis. Brown carbon in tar balls from smoldering biomass combustion. *Atmos. Chem. Phys.*, 10(13):6363–6370, 2010. doi:10.5194/acp-10-6363-2010.

K. R. Chan, J. Dean-Day, S. W. Bowen, and T. P. Bui. Turbulence measurements by the DC-8 Meteorological Measurement System. *Geophys. Res. Lett.*, 25(9):1355–1358, 1998. doi:https://doi.org/10.1029/97GL03590.

Hsueh-chia Chang and T. T. Charalampopoulos. Determination of the wavelength dependence of refractive indices of flame soot. *Proc. R. Soc. Lond. A*, 430(1880):577–591, 1990. doi:10.1098/rspa.1990.0107.

Y. Chen and T. C. Bond. Light absorption by organic carbon from wood combustion. *Atmos. Chem. Phys.*, 10(4):1773–1787, 2010. doi:10.5194/acp-10-1773-2010.

Sonya Collier, Shan Zhou, Timothy B. Onasch, Daniel A. Jaffe, Lawrence Kleinman, Arthur J. Sedlacek, Nicole L. Briggs, Jonathan Hee, Edward Fortner, John E. Shilling, Douglas Worsnop, Robert J. Yokelson, Caroline Parworth, Xinlei Ge, Jianzhong Xu, Zachary Butterfield, Duli Chand, Manvendra K. Dubey, Mikhail S. Pekour, Stephen Springston, and Qi Zhang. Regional Influence of Aerosol Emissions from Wildfires

Driven by Combustion Efficiency: Insights from the BBOP Campaign. *Environ. Sci. Tech.*, 50:8613–8622, 2016. doi:10.1021/acs.est.6b01617.

Paul J. Crutzen, Leroy E. Heidt, Joseph P. Krasnec, and Wolfgang Pollock, Walter H.and Seiler. Biomass burning as a source of atmospheric gases CO, H_2, N_2O, NO, CH_3Cl and COS. *Nature*, 282:253–256, 1979. ISSN 1476-4687. doi:https://doi.org/10.1038/282253a0.

Tim Deutschmann, Steffen Beirle, Udo Frieß, Michael Grzegorski, Christoph Kern, Lena Kritten, Ulrich Platt, Cristina Prados-Román, Jānis Puķı¯te, Thomas Wagner, Bodo Werner, and Klaus Pfeilsticker. The Monte Carlo atmospheric radiative transfer model McArtim: Introduction and validation of Jacobians and 3D features. *J. Quant. Spectrosc. Ra.*, 112(6):1119–1137, 2011. ISSN 0022-4073. doi:https://doi.org/10.1016/j.jqsrt.2010.12.009.

Mike Flannigan, Alan S. Cantin, William J. de Groot, Mike Wotton, Alison Newbery, and Lynn M. Gowman. Global wildland fire season severity in the 21st century. *Forest Ecol. Manag.*, 294:54–61, 2013. ISSN 0378-1127. doi:https://doi.org/10.1016/j.foreco.2012.10.022.

Haviland Forrister, Jiumeng Liu, Eric Scheuer, Jack Dibb, Luke Ziemba, Kenneth L. Thornhill, Bruce Anderson, Glenn Diskin, Anne E. Perring, Joshua P. Schwarz, Pedro Campuzano-Jost, Douglas A. Day, Brett B. Palm, Jose L. Jimenez, Athanasios Nenes, and Rodney J. Weber. Evolution of brown carbon in wildfire plumes. *Geophys. Res. Lett.*, 42(11):4623–4630, 2015. doi:https://doi.org/10.1002/2015GL063897.

U. Frieß, S. Beirle, L. Alvarado Bonilla, T. Bösch, M. M. Friedrich, F. Hendrick, A. Piters, A. Richter, M. van Roozendael, V. V. Rozanov, E. Spinei, J.-L. Tirpitz, T. Vlemmix,

T. Wagner, and Y. Wang. Intercomparison of MAX-DOAS vertical profile retrieval algorithms: studies using synthetic data. *Atmos. Meas. Tech.*, 12(4):2155–2181, 2019. doi:10.5194/amt-12-2155-2019.

Daniel L. Goldberg, Susan C. Anenberg, Gaige Hunter Kerr, Arash Mohegh, Zifeng Lu, and David G. Streets. TROPOMI NO_2 in the United States: A Detailed Look at the Annual Averages, Weekly Cycles, Effects of Temperature, and Correlation With Surface NO_2 Concentrations. *Earth's Fut.*, 9(4), 2021. doi:https://doi.org/10.1029/2020EF001665.

V. Gorshelev, A. Serdyuchenko, M. Weber, W. Chehade, and J. P. Burrows. High spectral resolution ozone absorption cross-sections – Part 1: Measurements, data analysis and comparison with previous measurements around 293 K. *Atmos. Meas. Tech.*, 7(2), 2014. ISSN 18671381. doi:10.5194/amt-7-609-2014.

D. Griffin, C. Sioris, J. Chen, N. Dickson, A. Kovachik, M. de Graaf, S. Nanda, P. Veefkind, E. Dammers, C. A. McLinden, P. Makar, and A. Akingunola. The 2018 fire season in North America as seen by TROPOMI: aerosol layer height intercomparisons and evaluation of model-derived plume heights. *Atmos. Meas. Tech.*, 13(3):1427–1445, 2020. doi:10.5194/amt-13-1427-2020.

D. Griffin, C. A. McLinden, E. Dammers, C. Adams, C. Stockwell, C. Warneke, I. Bourgeois, J. Peischl, T. B. Ryerson, K. J. Zarzana, J. P. Rowe, R. Volkamer, C. Knote, N. Kille, T. K. Koenig, C. F. Lee, D. Rollins, P. S. Rickly, J. Chen, L. Fehr, A. Bourassa, D. Degenstein, K. Hayden, C. Mihele, S. N. Wren, J. Liggio, A. Akingunola, and P. Makar. Biomass burning nitrogen dioxide emissions derived from space with TROPOMI:

methodology and validation. *Atmos. Meas. Tech. Discuss.*, 2021. doi:10.5194/amt-2021-223.

Johnathan W. Hair, Chris A. Hostetler, Anthony L. Cook, David B. Harper, Richard A. Ferrare, Terry L. Mack, Wayne Welch, Luis Ramos Izquierdo, and Floyd E. Hovis. Airborne High Spectral Resolution Lidar for profiling aerosol optical properties. *Appl. Opt.*, 47 (36):6734–6752, Dec 2008. doi:10.1364/AO.47.006734.

Rachel F. Hems, Elijah G. Schnitzler, Carolyn Liu-Kang, Christopher D. Cappa, and Jonathan P.D. Abbatt. Aging of Atmospheric Brown Carbon Aerosol. *ACS Earth Space Chem.*, 5:722–748, 2021. doi:10.1021/acsearthspacechem.0c00346.

F. Hendrick, M. Van Roozendael, A. Kylling, A. Petritoli, A. Rozanov, S. Sanghavi, R. Schofield, C. von Friedeburg, T. Wagner, F. Wittrock, D. Fonteyn, and M. De Mazière. Intercomparison exercise between different radiative transfer models used for the interpretation of ground-based zenith-sky and multi-axis DOAS observations. *Atmos. Chem. Phys.*, 6(1):93–108, 2006. doi:10.5194/acp-6-93-2006.

C. J. Hennigan, M. A. Miracolo, G. J. Engelhart, A. A. May, A. A. Presto, T. Lee, A. P. Sullivan, G. R. McMeeking, H. Coe, C. E. Wold, W. M. Hao, J. B. Gilman, W. C. Kuster, J. De Gouw, B. A. Schichtel, J. L. Collett, S. M. Kreidenweis, and A. L. Robinson. Chemical and physical transformations of organic aerosol from the photo-oxidation of open biomass burning emissions in an environmental chamber. *Atmos. Chem. Phys.*, 2011. ISSN 1680-7324. doi:10.5194/acp-11-7669-2011.

Simon J Hook, Jeffrey J Myers, Kurtis J Thome, Michael Fitzgerald, and Anne B Kahle. The MODIS/ASTER airborne simulator (MASTER) — a new instrument for earth science studies. *Rem. Sens. Env.*, 76(1):93–102, 2001. ISSN 0034-4257. doi:https://doi.org/10.1016/S0034-4257(00)00195-4.

Matthew D. Hurteau, Shuang Liang, A. LeRoy Westerling, and Christine Wiedinmyer. Vegetation-fire feedback reduces projected area burned under climate change. *Sci. Rep.*, 9, 02 2019. doi:10.1038/s41598-019-39284-1.

Daniel J. Jacob. Heterogeneous chemistry and tropospheric ozone. *Atmos. Environ.*, 34(12): 2131–2159, 2000. ISSN 1352-2310. doi:https://doi.org/10.1016/S1352-2310(99)00462-8.

Daniel A. Jaffe and Nicole L. Wigder. Ozone production from wildfires: A critical review. *Atmos. Environ.*, 51:1–10, 2012. ISSN 1352-2310. doi:https://doi.org/10.1016/j.atmosenv.2011.11.063.

C. N. Jen, L. E. Hatch, V. Selimovic, R. J. Yokelson, R. Weber, A. E. Fernandez, N. M. Kreisberg, K. C. Barsanti, and A. H. Goldstein. Speciated and total emission factors of particulate organics from burning western US wildland fuels and their dependence on combustion efficiency. *Atmos. Chem. Phys.*, 19(2):1013–1026, 2019. doi:10.5194/acp-19-1013-2019.

X. Jin, Q. Zhu, and R. Cohen. Direct estimates of biomass burning NOx emissions and lifetime using daily observations from TROPOMI. *Atmos. Chem. Phys. Discussions*, 2021: 1–27, 2021. doi:10.5194/acp-2021-381.

Angeliki Karanasiou, Andrés Alastuey, Fulvio Amato, Matteo Renzi, Massimo Stafoggia, Aurelio Tobias, Cristina Reche, Francesco Forastiere, Sophie Gumy, Pierpaolo Mudu, and Xavier Querol. Short-term health effects from outdoor exposure to biomass burning emissions: A review. *Sci. Total Environ.*, 781:146739, 2021. ISSN 0048-9697. doi:https://doi.org/10.1016/j.scitotenv.2021.146739.

Aaron S. Kaulfus, Udaysankar Nair, Daniel Jaffe, Sundar A. Christopher, and Scott Goodrick. Biomass Burning Smoke Climatology of the United States: Implications for Particulate Matter Air Quality. *Environ. Sci. Technol.*, 51(20):11731–11741, 2017. doi:10.1021/acs.est.7b03292.

Q. L. Kleipool, M. R. Dobber, J. F. de Haan, and P. F. Levelt. Earth surface reflectance climatology from 3 years of OMI data. *J. Geophys. Res. Atmos.*, 113(D18), 2008. doi:https://doi.org/10.1029/2008JD010290.

Daniel A. Lack, Mathews S. Richardson, Daniel Law, Justin M. Langridge, Christopher D. Cappa, Richard J. McLaughlin, and Daniel M. Murphy. Aircraft Instrument for Comprehensive Characterization of Aerosol Optical Properties, Part 2: Black and Brown Carbon Absorption and Absorption Enhancement Measured with Photo Acoustic Spectroscopy. *Aerosol Sci. Tech.*, 46(5):555–568, 2012. doi:10.1080/02786826.2011.645955.

Justin M. Langridge, Mathews S. Richardson, Daniel Lack, Daniel Law, and Daniel M. Murphy. Aircraft Instrument for Comprehensive Characterization of Aerosol Optical Properties, Part I: Wavelength-Dependent Optical Extinction and Its Relative Humidity Dependence Measured Using Cavity Ringdown Spectroscopy. *Aerosol Sci. Tech.*, 45(11): 1305–1318, 2011. doi:10.1080/02786826.2011.592745.

Chiara Levoni, Marco Cervino, Rodolfo Guzzi, and Francesca Torricella. Atmospheric aerosol optical properties: a database of radiative characteristics for different components and classes. *Appl. Opt.*, 36(30):8031–8041, Oct 1997. doi:10.1364/AO.36.008031.

A. Lorente, K. Folkert Boersma, H. Yu, S. Dörner, A. Hilboll, A. Richter, M. Liu, L. N. Lamsal, M. Barkley, I. De Smedt, M. Van Roozendael, Y. Wang, T. Wagner, S. Beirle, J.-T. Lin, N. Krotkov, P. Stammes, P. Wang, H. J. Eskes, and M. Krol. Structural uncertainty in air mass factor calculation for NO_2 and HCHO satellite retrievals. *Atmos. Meas. Tech.*, 10(3):759–782, 2017. doi:10.5194/amt-10-759-2017.

Brian I. Magi, Qiang Fu, and Jens Redemann. A methodology to retrieve self-consistent aerosol optical properties using common aircraft measurements. *J. Geophys. Res. Atmos.*, 112(D24), 2007. doi:https://doi.org/10.1029/2006JD008312.

M. Majdi, K. Sartelet, G. M. Lanzafame, F. Couvidat, Y. Kim, M. Chrit, and S. Turquety. Precursors and formation of secondary organic aerosols from wildfires in the Euro-Mediterranean region. *Atmos. Chem. Phys.*, 19(8):5543–5569, 2019. doi:10.5194/acp-19-5543-2019.

Jennifer R. Marlon, Patrick J. Bartlein, Daniel G. Gavin, Colin J. Long, R. Scott Anderson, Christy E. Briles, Kendrick J. Brown, Daniele Colombaroli, Douglas J. Hallett, Mitchell J. Power, Elizabeth A. Scharf, and Megan K. Walsh. Long-term perspective on wildfires in the western USA. *P. Natl. Acad. Sci. USA*, 109(9):E535–E543, 2012. ISSN 0027-8424. doi:10.1073/pnas.1112839109.

A. A. May, T. Lee, G. R. McMeeking, S. Akagi, A. P. Sullivan, S. Urbanski, R. J. Yokelson, and S. M. Kreidenweis. Observations and analysis of organic aerosol evolution in some prescribed fire smoke plumes. *Atmos. Chem. Phys.*, 15(11):6323–6335, 2015. doi:10.5194/acp-15-6323-2015.

Crystal D. McClure and Daniel A. Jaffe. US particulate matter air quality improves except in wildfire-prone areas. *P. Natl. Acad. Sci. USA*, 115, 2018. ISSN 10916490. doi:10.1073/pnas.1804353115.

Don McKenzie, David Peterson, and J. Littell. Global warming and stress complexes in forests of western North America. *Wildland Fires and Air Pollution*, 8, 01 2009.

A. C. Meier, A. Schönhardt, T. Bösch, A. Richter, A. Seyler, T. Ruhtz, D.-E. Constantin, R. Shaiganfar, T. Wagner, A. Merlaud, M. Van Roozendael, L. Belegante, D. Nicolae, L. Georgescu, and J. P. Burrows. High-resolution airborne imaging DOAS measurements of NO_2 above Bucharest during AROMAT. *Atmos. Meas. Tech.*, 10(5):1831–1857, 2017. doi:10.5194/amt-10-1831-2017.

K.-E. Min, R. A. Washenfelder, W. P. Dubé, A. O. Langford, P. M. Edwards, K. J. Zarzana, J. Stutz, K. Lu, F. Rohrer, Y. Zhang, and S. S. Brown. A broadband cavity enhanced absorption spectrometer for aircraft measurements of glyoxal, methylglyoxal, nitrous acid, nitrogen dioxide, and water vapor. *Atmos. Meas. Tech.*, 9(2):423–440, 2016. doi:10.5194/amt-9-423-2016.

Jungbin Mok, Nickolay A. Krotkov, Antti Arola, Omar Torres, Hiren Jethva, Marcos Andrade, Gordon Labow, Thomas F. Eck, Zhanqing Li, Russell R. Dickerson, Georgiy L. Stenchikov, Sergey Osipov, and Xinrong Ren. Impacts of brown carbon from biomass burning on surface UV and ozone photochemistry in the Amazon Basin. *Sci. Rep.*, 2016. doi:10.1038/srep36940.

H. Moosmüller, R. K. Chakrabarty, K. M. Ehlers, and W. P. Arnott. Absorption Ångström coefficient, brown carbon, and aerosols: basic concepts, bulk matter, and spherical particles. *Atmos. Chem. Phys.*, 11(3):1217–1225, 2011. doi:10.5194/acp-11-1217-2011.

NASA/LARC/SD/ASDC. Stratospheric Aerosol and Gas Experiment (SAGE) II Version 7.0 Data. *NASA Langley Atmospheric Science Data Center DAAC*, 2012. doi:https://doi.org/10.5067/ERBS/SAGEII/SOLAR_BINARY_L2-V7.0.

Amanda M. Nienow and Jeffrey T. Roberts. Heterogeneous Chemistry of Carbon Aerosols. *Annu. Rev. Phys. Chem.*, 57(1):105–128, 2006. doi:10.1146/annurev.physchem.57.032905.104525.

Sean Parks, Carol Miller, Marc-André Parisien, Lisa Holsinger, Solomon Dobrowski, and John Abatzoglou. Wildland fire deficit and surplus in the western United States, 1984–2012. *Ecosphere*, 6, 12 2015. doi:10.1890/ES15-00294.1.

Qiaoyun Peng, Brett B. Palm, Kira E. Melander, Ben H. Lee, Samuel R. Hall, Kirk Ullmann, Teresa Campos, Andrew J. Weinheimer, Eric C. Apel, Rebecca S. Hornbrook, Alan J. Hills, Denise D. Montzka, Frank Flocke, Lu Hu, Wade Permar, Catherine Wielgasz, Jakob Lindaas, Ilana B. Pollack, Emily V. Fischer, Timothy H. Bertram, and Joel A. Thornton. HONO Emissions from Western U.S. Wildfires Provide Dominant Radical Source in Fresh Wildfire Smoke. *Environ. Sci. Technol.*, 54(10):5954–5963, 2020. doi:10.1021/acs.est.0c00126.

Ulrich Platt and Jochen Stutz. *Differential Optical Absorption Spectroscopy (DOAS), Principles and Applications*. Springer, 2008. ISBN 978-3-540- 21193-8.

R. P. Pokhrel, N. L. Wagner, J. M. Langridge, D. A. Lack, T. Jayarathne, E. A. Stone, C. E. Stockwell, R. J. Yokelson, and S. M. Murphy. Parameterization of single-scattering albedo (SSA) and absorption Ångström exponent (AAE) with EC / OC for aerosol emissions from biomass burning. *Atmos. Chem. Phys.*, 16(15):9549–9561, 2016. doi:10.5194/acp-16-9549-2016.

Susan J. Prichard, Anne G. Andreu, Roger D. Ottmar, and Ellen Eberhardt. Fuel characteristic classification system (FCCS) field sampling and fuelbed development guide. *USDA For. Serv. T. R. PNW*, 2019. ISSN 08874840. doi:10.2737/PNW-GTR-972.

Dirk Richter, Petter Weibring, J.G. Walega, A. Fried, Scott Spuler, and Matthew Taubman. Compact highly sensitive multi-species airborne mid-IR spectrometer. *Appl. Phys. B*, 119, 02 2015. doi:10.1007/s00340-015-6038-8.

L. S. Rothman, I. E. Gordon, R. J. Barber, H. Dothe, R. R. Gamache, A. Goldman, V. I. Perevalov, S. A. Tashkun, and J. Tennyson. HITEMP, the high-temperature molecular spectroscopic database. *J. Quant. Spectrosc. Radiat. Transf.*, 111(15), 2010. ISSN 00224073. doi:10.1016/j.jqsrt.2010.05.001.

R. Saleh, C. J. Hennigan, G. R. McMeeking, W. K. Chuang, E. S. Robinson, H. Coe, N. M. Donahue, and A. L. Robinson. Absorptivity of brown carbon in fresh and photochemically aged biomass-burning emissions. *Atmos. Chem. and Phys.*, 13(15):7683–7693, 2013. doi:10.5194/acp-13-7683-2013.

Rawad Saleh, Ellis S. Robinson, Daniel S. Tkacik, Adam T. Ahern, Shang Liu, Allison C. Aiken, Ryan C. Sullivan, Albert A. Presto, Manvendra K. Dubey, Robert J. Yokelson, Neil M. Donahue, and Allen L. Robinson. Brownness of organics in aerosols from biomass burning linked to their black carbon content. *Nat. Geosci.*, 7:647–650, 2014. ISSN 1752-0908. doi:10.1038/ngeo2220.

Rawad Saleh, Zezhen Cheng, and Khairallah Atwi. The Brown–Black Continuum of Light-Absorbing Combustion Aerosols. *Environ. Sci. Technol. Lett.*, 5(8):508–513, 2018. doi:10.1021/acs.estlett.8b00305.

Jonathan M. Samet, Francesca Dominici, Frank C. Curriero, Ivan Coursac, and Scott L. Zeger. Fine Particulate Air Pollution and Mortality in 20 U.S. Cities, 1987–1994. *New Engl. J. Med.*, 343(24):1742–1749, 2000. doi:10.1056/NEJM200012143432401.

K. Sekimoto, A. R. Koss, J. B. Gilman, V. Selimovic, M. M. Coggon, K. J. Zarzana, B. Yuan, B. M. Lerner, S. S. Brown, C. Warneke, R. J. Yokelson, J. M. Roberts, and J. de Gouw. High- and low-temperature pyrolysis profiles describe volatile organic compound emissions from western US wildfire fuels. *Atmos. Chem. Phys.*, 18(13):9263–9281, 2018. doi:10.5194/acp-18-9263-2018.

Richard E. Shetter and Martin Müller. Photolysis frequency measurements using actinic flux spectroradiometry during the PEM-Tropics mission: Instrumentation description and some results. *J. Geophys. Res.-Atmos.*, 104(D5):5647–5661, 1999. doi:10.1029/98JD01381.

Amber Soja, Emily Gargulinski, Elizabeth Wiggins, Jessica McCarty, Andy Hudak, Eileen Rintsch, Kevin Hiers, Chris Schmidt, , and Justin Fain. Fueled from below: Linking Fire, Fuels, and Weather to Atmospheric Chemistry. Session: Fire Influence on Regional to Global Environments and Air Quality (FIREX-AQ), Virtual, 2021. 3rd International Smoke Symposium.

Robert Spurr and Matt Christi. *The LIDORT and VLIDORT Linearized Scalar and Vector Discrete Ordinate Radiative Transfer Models: Updates in the Last 10 Years*, pages 1–62. Springer International Publishing, 2019. ISBN 978-3-030-03445-0. doi:10.1007/978-3-030-03445-0_1.

Robert J.D. Spurr. VLIDORT: A linearized pseudo-spherical vector discrete ordinate radiative transfer code for forward model and retrieval studies in multilayer multiple scattering media. *J. Quant. Spectrosc. Radiat. Transfer*, 102, 2006. ISSN 00224073. doi:10.1016/j.jqsrt.2006.05.005.

K. Stemmler, M. Ndour, Y. Elshorbany, J. Kleffmann, B. D'Anna, C. George, B. Bohn, and

M. Ammann. Light induced conversion of nitrogen dioxide into nitrous acid on submicron humic acid aerosol. *Atmos. Chem. Phys.*, 7(16):4237–4248, 2007. doi:10.5194/acp-7-4237-2007.

Konrad Stemmler, Markus Ammann, Chantal Donders, Jörg Kleffmann, and Christian George. Photosensitized reduction of nitrogen dioxide on humic acid as a source of nitrous acid. *Nature*, 2006. doi:10.1038/nature04603.

J. Stutz, E. S. Kim, U. Platt, P. Bruno, C. Perrino, and A. Febo. UV-visible absorption cross sections of nitrous acid. *J. Geophys. Res. Atmos.*, 105(D11), 2000. ISSN 01480227. doi:10.1029/2000JD900003.

Jochen Stutz, Bodo Werner, Max Spolaor, Lisa Scalone, James Festa, Catalina Tsai, Ross Cheung, Santo F. Colosimo, Ugo Tricoli, Rasmus Raecke, Ryan Hossaini, Martyn P. Chipperfield, Wuhu Feng, Ru Shan Gao, Eric J. Hintsa, James W. Elkins, Fred L. Moore, Bruce Daube, Jasna Pittman, Steven Wofsy, and Klaus Pfeilsticker. A new Differential Optical Absorption Spectroscopy instrument to study atmospheric chemistry from a high-altitude unmanned aircraft. *Atmos. Meas. Tech.*, 10, 2017. ISSN 18678548. doi:10.5194/amt-10-1017-2017.

Benjamin J. Sumlin, Yuli W. Heinson, Nishit Shetty, Apoorva Pandey, Robert S. Pattison, Stephen Baker, Wei Min Hao, and Rajan K. Chakrabarty. UV–Vis–IR spectral complex refractive indices and optical properties of brown carbon aerosol from biomass burning. *J. Quant. Spectrosc. Ra.*, 206:392–398, 2018. ISSN 0022-4073. doi:https://doi.org/10.1016/j.jqsrt.2017.12.009.

Ryan Thalman and Rainer Volkamer. Temperature dependent absorption cross-sections of O2-O 2 collision pairs between 340 and 630 nm and at atmospherically relevant pressure. *Phys. Chem. Chem. Phys.*, 15(37), 2013. ISSN 14639076. doi:10.1039/c3cp50968k.

Nicolas Theys, Rainer Volkamer, J.-F Müller, K. Zarzana, N. Kille, Lieven Clarisse, Isabelle De Smedt, C. Lerot, H. Finkenzeller, Francois Hendrick, T. Koenig, C. Lee, Christoph Knote, Huan Yu, and Michel Van Roozendael. Global nitrous acid emissions and levels of regional oxidants enhanced by wildfires. *Nat. Geosci.*, 13:1–6, 10 2020. doi:10.1038/s41561-020-0637-7.

O. Torres, H. Jethva, C. Ahn, G. Jaross, and D. G. Loyola. TROPOMI aerosol products: evaluation and observations of synoptic-scale carbonaceous aerosol plumes during 2018–2020. *Atmos. Meas. Tech.*, 13(12):6789–6806, 2020. doi:10.5194/amt-13-6789-2020.

Jörg Trentmann, Robert J. Yokelson, Peter V. Hobbs, Tanja Winterrath, Theodore J. Christian, Meinrat O. Andreae, and Sherri a. Mason. An analysis of the chemical processes in the smoke plume from a savanna fire. *J. Geophys. Res. D: Atmos.*, 110(12):1–20, 2005. ISSN 0148-0227. doi:10.1029/2004JD005628.

Katie Tuite, Jennie L. Thomas, Patrick R. Veres, James M. Roberts, Philip S. Stevens, Stephen M. Griffith, Sebastien Dusanter, James H. Flynn, Shaddy Ahmed, Louisa Emmons, Si-Wan Kim, Rebecca Washenfelder, Cora Young, Catalina Tsai, Olga Pikelnaya, and Jochen Stutz. Quantifying Nitrous Acid Formation Mechanisms Using Measured Vertical Profiles During the CalNex 2010 Campaign and 1D Column Modeling. *J. Geophys. Res. Atmos.*, 126(13), 2021. doi:https://doi.org/10.1029/2021JD034689.

S. Voigt, J. Orphal, and J. P. Burrows. The temperature and pressure dependence of the absorption cross-sections of NO_2 in the 250-800 nm region measured by Fouriertransform spectroscopy. *J. Photochem. Photobiol. A Chem.*, 149(1-3), 2002. ISSN 10106030. doi:10.1016/S1010-6030(01)00650-5.

T. Wagner, J. P. Burrows, T. Deutschmann, B. Dix, C. von Friedeburg, U. Frieß, F. Hendrick, K.-P. Heue, H. Irie, H. Iwabuchi, Y. Kanaya, J. Keller, C. A. McLinden, H. Oetjen, E. Palazzi, A. Petritoli, U. Platt, O. Postylyakov, J. Pukite, A. Richter, M. van Roozendael, A. Rozanov, V. Rozanov, R. Sinreich, S. Sanghavi, and F. Wittrock. Comparison of box-air-mass-factors and radiances for Multiple-Axis Differential Optical Absorption Spectroscopy (MAX-DOAS) geometries calculated from different UV/visible radiative transfer models. *Atmos. Chem. Phys.*, 7(7):1809–1833, 2007. doi:10.5194/acp-7-1809-2007.

T Wagner, S Beirle, T Deutschmann, E Eigemeier, C Frankenberg, M Grzegorski, C Liu, T Marbach, U Platt, and M Penning de Vries. Monitoring of atmospheric trace gases, clouds, aerosols and surface properties from UV/vis/NIR satellite instruments. *J. Opt. A-Pure Appl. Op.*, 10(10):104019, aug 2008. doi:10.1088/1464-4258/10/10/104019.

J. X. Warner, Z. Wei, L. L. Strow, C. D. Barnet, L. C. Sparling, G. Diskin, and G. Sachse. Improved agreement of AIRS tropospheric carbon monoxide products with other EOS sensors using optimal estimation retrievals. *Atmos. Chem. Phys.*, 10(19):9521–9533, 2010. doi:10.5194/acp-10-9521-2010.

Anthony LeRoy Westerling. Increasing western US forest wildfire activity: sensitivity to changes in the timing of spring. *Philos. T. R. Soc. B*, 371(1696):20150178, 2016. doi:10.1098/rstb.2015.0178.

A. Park Williams, John T. Abatzoglou, Alexander Gershunov, Janin Guzman-Morales, Daniel A. Bishop, Jennifer K. Balch, and Dennis P. Lettenmaier. Observed Impacts of

Anthropogenic Climate Change on Wildfire in California. *Earth's Fut.*, 7(8):892–910, 2019. doi:https://doi.org/10.1029/2019EF001210.

Jenny P.S. Wong, Maria Tsagkaraki, Irini Tsiodra, Nikolaos Mihalopoulos, Kalliopi Violaki, Maria Kanakidou, Jean Sciare, Athanasios Nenes, and Rodney J. Weber. Effects of Atmospheric Processing on the Oxidative Potential of Biomass Burning Organic Aerosols. *Environ. Sci. Technol.*, 53(12):6747–6756, 2019. doi:10.1021/acs.est.9b01034.

R. J. Yokelson, J. D. Crounse, P. F. DeCarlo, T. Karl, S. Urbanski, E. Atlas, T. Campos, Y. Shinozuka, V. Kapustin, A. D. Clarke, A. Weinheimer, D. J. Knapp, D. D. Montzka, J. Holloway, P. Weibring, F. Flocke, W. Zheng, D. Toohey, P. O. Wennberg, C. Wiedinmyer, L. Mauldin, A. Fried, D. Richter, J. Walega, J. L. Jimenez, K. Adachi, P. R. Buseck, S. R. Hall, and R. Shetter. Emissions from biomass burning in the Yucatan. *Atmos. Chem. Phys.*, 9, 2009. ISSN 16807324. doi:10.5194/acp-9-5785-2009.

Chengxin Zhang, Cheng Liu, Ka Lok Chan, Qihou Hu, Haoran Liu, Bo Li, Chengzhi Xing, Wei Tan, Haijin Zhou, Fuqi Si, and Jianguo Liu. First observation of tropospheric nitrogen dioxide from the Environmental Trace Gases Monitoring Instrument onboard the GaoFen-5 satellite. *Light-Sci. Appl.*, 9, 12 2020. doi:10.1038/s41377-020-0306-z.

Lei Zhu, Daniel J. Jacob, Frank N. Keutsch, Loretta J. Mickley, Richard Scheffe, Madeleine Strum, Gonzalo González Abad, Kelly Chance, Kai Yang, Bernhard Rappenglück, Dylan B. Millet, Munkhbayar Baasandorj, Lyatt Jaeglé, and Viral Shah. Formaldehyde (HCHO) As a Hazardous Air Pollutant: Mapping Surface Air Concentrations from Satellite and Inferring Cancer Risks in the United States. *Environ. Sci. Technol.*, 51(10): 5650–5657, 2017. doi:10.1021/acs.est.7b01356.